Measurement of the Inclusive Deep Inelastic Scattering Cross Section at low Q^2

DISSERTATION

zur Erlangung des akademischen Grades

doctor rerum naturalium
(Dr. rer. nat.)

im Fach Physik

eingereicht an der

Mathematisch-Naturwissenschaftlichen Fakultät I
der Humboldt-Universität zu Berlin

von

Mgr. Tomáš Laštovička

geboren am 13. Oktober 1974 in Náchod, Tschechische Republik

Präsident der Humbdolt-Universität zu Berlin
Prof. Dr. J. Mlynek

Dekan der Mathematisch-Naturwissenschaftlichen Fakultät I
Prof. Dr. M. Linscheid

Gutachter/innen: Prof. Dr. H. Kolanoski
Prof. Dr. J. B. Dainton
Prof. Dr. N. Pavel

Tag der mündlichen Prüfung: 7. Mai 2004

Abstract

A measurement of the inclusive cross section for the deep inelastic scattering of positrons on protons is presented in the transition region from the non-perturbative to the deep inelastic domain at low four momentum transfer squared Q^2. The analysis is based on data collected by the H1 experiment during special runs in the years 1999 and 2000. Thus this thesis presents the first accurate HERA data at low x for $Q^2 \sim 1\,\mathrm{GeV}^2$ accessed with new instrumentation and novel analysis methods to extract the proton structure functions. The longitudinal structure function F_L is extracted for the first time at low values of Q^2, x.

A completely new approach to study low x proton structure is proposed, by looking at fractal patterns in the parton densities. The proton is seen as a multi-fractal and the corresponding fractal dimensions are determined by constructing a phenomenological model which is fitted to the H1 data on the F_2 proton structure function. This approach is found to describe the data excellently, from the non-perturbative to the perturbative region, and can be used to obtain deeper and complementary understanding of the proton substructure.

Zusammenfassung

Diese Arbeit praesentiert die Messung des inklusiven, tiefinelastischen Streuquerschnitts von Positronen and Protonen, in der Uebergangsregion vom nichtperturbativen zum tiefinelastischen Verhalten, bei kleinen Impulsuebertraegen Q^2. Die Analyse beruht auf Daten, die vom H1 Experiment in speziellen Datennahmeperioden in den Jahren 1999 und 2000 aufgezeichnet wurden. Die Doktorarbeit enthaelt daher die ersten genauen Messdaten, bei kleinen x fuer $Q^2 \sim 1\,\mathrm{GeV}^2$, die mit neuer Messtechnik und Analysemethoden zugaenglich gemacht wurden, um die Protonstrukturfunktionen zu messen. Zum ersten Mal werden dabei auch Daten fuer die longitudinale Strukturfunktion F_L bei kleinen Werten Q^2, x erhalten.

Ein ganz neuer Zugang zur Untersuchung der Protonstruktur bei kleinen x wird vorgestellt, der auf den fraktalen Strukturen der Partondichten beruht. Das Proton wird als ein Multifraktal angesehen und die entsprechenden fraktalen Dimensionen werden bestimmt, indem ein phaenomenologischer Ansatz entwickelt wird, der an die H1-Daten der F_2 Strukturfunktion angepasst wurde. Es zeigt sich, dass dieses Modell die Daten exzellent beschreibt, vom nichtperturbativen zum stoerungstheoretisch behandelten Bereich, und also verfuegbar ist, um ein tieferes, komplementaeres Verstaendnis der Protonsubstruktur zu ermoeglichen.

Contents

Introduction

The beginning of attempts to understand the origin and structure of the matter dates back to the times of ancient Greek and Indian philosophers. The matter was seen to be composed of a number of elements, as e.g. four (Empedocle) or twenty-four[1] (Bhagavad Gita). Later a concept of indivisible *atoms* was introduced by Leucippe and Democrite and approximately at the same epoch a similar philosophy was taught by the Indian philosophy system Vaiseshika. Although there were no experimental opportunities to proof or disproof those theories, they formed a ground for theories developed many centuries later. Important concepts introduced at that times are: symmetry, a concept of elementary particles and a concept of classification.

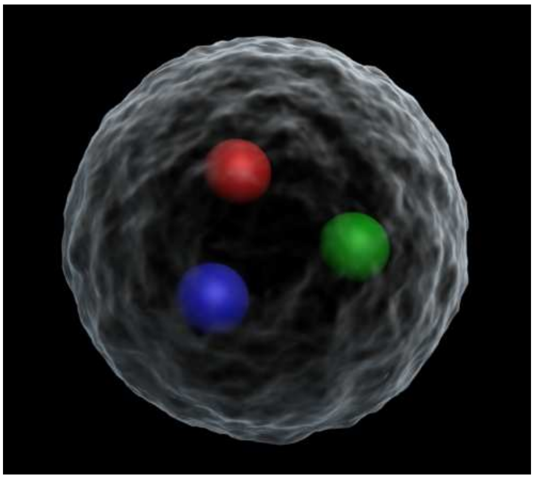

The interest in matter has developed via alchemy of middle ages, philosophy in the 17th and 18th century and due to developments in experimental techniques to the birth of the modern science epoch in the 19th century. It has started with the construction of a periodic table of elements by the Russian chemist Mendeleev and with the discovery of the electron by Thompson, who also proposed a naive 'pudding' model of an atom. Thomspon's disciple and Nobel price winner for chemistry, Rutherford, performed the first scattering experiments in order to understand the inner structure of atoms. In his experiment, together with Geiger and Marsden, he observed that a measurable fraction of alpha particles scattered off a thin golden foil scatters through large angles. According to Rutherford: "It was almost as incredible as if you fired a 15-inch shell at a piece of tissue paper and it came back and hit you." As a consequence of this experiment the pudding model of Thompson was disproved and evidence raised for a very small positively charged nuclei within the atom. Further experiments of this kind observed effects which were not explainable by the conventional electromagnetic theory and gave birth to the theory of the strong interactions.

Until the sixties it was widely believed that there are only three elementary massive particles: electron, proton and neutron. Although experiments performed on particle accelerators detected a large number of unstable particles, these were treated to be composed of elementary ones. In 1964, Gell-Mann and Zweig independently proposed a progressive model in which the elementary particles are so called *quarks* out of which protons and neutrons are composed. In the late sixties, high energy electron-proton scattering at the Stanford Linear Accelerator Centre (SLAC) provided the first evidence for substructure within the proton [1].

[1]Note that in the standard model there are indeed 24 elementary fermions, including anti-particles.

Particle physics nowadays is concerned with studying the matter constituents and the way they interact with each other. The Standard Model [2] of high energy physics describes the elementary matter constituents as quarks and leptons, which interact with each other through the exchange of gauge bosons. The electro-weak interaction of quarks and leptons, mediated by photons and $W^{\pm}$, Z^0 bosons, is precisely described. Thus these particles can be employed to probe the structure of composed particles such as protons.

The research topic of this thesis is to investigate in detail the proton structure at low four momentum transfer squared Q^2, in the transition region from the non-perturbative to the deep inelastic domain. This region remains poorly understood, although it is essential for a complete understanding of Quantum Chromodynamics (QCD) and the mechanism of quark *confinement*. In QCD, the mechanism of quark confinement is a long-distance phenomenon. While quarks in the proton behave as almost free particles when probed at small distances, at large distances the strong interaction keeps them confined together. Hence, a promising approach to understand confinement is to study the transition from the small-distance deep inelastic domain of ep scattering at large values of Q^2 to the low Q^2 region, where the infrared behavior of QCD sets in. Furthermore, the region of low Q^2 is very valuable in the search for novel and exotic QCD effects, such as saturation. This effect has not yet been conclusively observed. Its likely existence is motivated by the strong rise of the proton structure function F_2 towards low Bjorken x, the fraction of the proton momentum carried by the struck quark. The rise is generated by the gluonic content of the proton and at the lowest values of x reached at HERA, it approaches the unitarity limit where the interaction probability becomes unity. Hence, the rise is expected to slow down or 'saturate', for example due to gluon recombination effects.

The underlying mechanisms of strong interactions and of confinement can be studied in an alternative way, by looking at the fractal patterns in the parton densities. This approach was found to describe excellently experimental data [3] and can be used to obtain deeper and complementary understanding of low x, Q^2 physics.

This thesis presents new data which were taken in special runs by the H1 collaboration to access the region of low Q^2 and also a wide region of inelasticity y. The accurate measurement of the deep inelastic scattering cross section allows the proton structure function F_2 to be determined at low Q^2 and Bjorken x. At high $y > 0.5$ the cross section rise towards low x is weakened which is attributable to the second, the longitudinal structure function F_L. Access to the extreme regions of y is possible by using the new Backward Silicon Tracker which at high y suppresses neutral particle background and which at low y, where the hadronic final state escapes detection in proton beam direction, restores efficiently the vertex reconstruction efficiency. Based on the cross section data novel methods are introduced here to extract F_L, measure the rise of F_2 to low x and for the first time to access the region of large x at low Q^2 by using QED radiative events in a new way.

This thesis is organized as follows

- The theoretical background to the deep inelastic scattering is presented in the first chapter. It is followed by an introduction to the Quark Parton Model (QPM) and Quantum Chromodynamics (QCD) and to the evolution of the the proton structure functions. The rise of the F_2 proton structure function and in this context the dipole saturation model are also discussed.

- In the second chapter a novel approach to the proton structure description via the fractal geometry concept is introduced. The chapter starts with an introduction to the fractal geometry. An overview of mostly theoretical work on this subject in the context of quantum mechanics is given in order to summarize motivations to study fractal properties of the proton structure. The fractal model construction and a fit of the resulting structure function parametrization to the experimental data is presented. Finally the chapter is enclosed by a discussion of the photoproduction limit, the rise of F_2 and also of the pion structure function in the fractal model framework.

- The experimental part of this thesis is opened in the third chapter by an overview of the H1 detector at HERA and its relevant components. Special focus is paid on the backward silicon tracker (BST) and the backward spaghetti calorimeter (SpaCal), which are the main sub-detectors used in the presented low Q^2 analysis.

- The fourth chapter presents the double differential deep inelastic scattering cross section measurement at values of low four momentum transfer squared Q^2. The chapter incorporates all necessary analysis steps, including alignment and calibration of sub-detectors, efficiency studies and Monte Carlo simulation treatment. The chapter concludes with the results for the DIS cross section, a study of the rise of F_2 at low Q^2 and with an extraction of the longitudinal structure function F_L.

- Finally, in the last chapter all results of this thesis are summarized.

The thesis has three appendixes devoted to the introduction of structure functions, the evaluation of fractal path dimension via path integrals and to the tables of the experimental results.

Chapter 1

Deep inelastic scattering

The *deep inelastic scattering* (DIS) process at HERA is characterized by the exchange of space-like virtual gauge boson between the interacting lepton and proton. According to the type of exchanged boson the DIS processes can be classified into two groups:

- **neutral current** processes (NC DIS) $ep \to eX$ are mediated by the exchange of neutral gauge bosons, photon and Z^0 boson. At virtuality $Q^2 \ll M_Z^2$, where M_Z is the mass of the Z^0 boson, the Born cross section is dominated by single-photon exchange since the weak interaction is suppressed by a factor of M_Z^2 in the Z^0 boson propagator.

- **charged current** processes (CC DIS) $ep \to \nu_e X$ are mediated by the exchange of charged gauge bosons $W^{\pm}$. Again, this weak interaction is suppressed by a factor of W boson mass squared M_W^2 entering the gauge boson propagator.

The kinematic region studied in this thesis corresponds to four-momentum transfers squared $0.35 \leq Q^2 \leq 12$ GeV^2. The masses of Z^0 and $W^{\pm}$ bosons are about 90.2 GeV and 80.4 GeV, respectively, and thus in the considered Q^2 region the influence of the weak interactions is negligible.

In this Chapter, the kinematics and the cross section of DIS events are introduced in Sections 1.1 and 1.2, respectively. More details on the introduction of proton structure functions can be found in Appendix A. The Quark Parton Model is introduced in Section 1.3 and Quantum Chromodynamics in Section 1.4. Various models of the proton structure evolution are briefly discussed in Section 1.5. A phenomenological study of the rise of the proton structure function F_2 is presented in Section 1.7. Finally, Section 1.8 contains an introduction to the GBW saturation model.

1.1 Kinematics of DIS events

The kinematics of the process is described by two independent Lorentz invariant quantities. The four momentum transfer squared Q^2 is given as

$$Q^2 = -q^2 = -(k - k')^2, \tag{1.1}$$

where k (k') is the four-momentum of the incoming (outgoing) positron (see Figure 1.1). Another Lorentz invariant quantity is the inelasticity y

$$y = \frac{p(k - k')}{pk}, \tag{1.2}$$

where p is the momentum of incoming proton. The inelasticity y is dimensionless and corresponds to the fraction of momentum lost by the electron in the proton rest frame. Thus it is bounded to the range $\langle 0, 1\rangle$.

A further frequently used variable, called Bjorken x, is defined as the ratio of the four-momentum transfer squared and the energy transfer in the proton rest frame,

$$x = \frac{Q^2}{2p(k - k')}. \tag{1.3}$$

As in the case of the inelasticity y, the Bjorken x variable is dimensionless and limited to the range $\langle 0, 1\rangle$. In the naive QPM it corresponds to the fraction of the nucleon momentum carried by the struck quark.

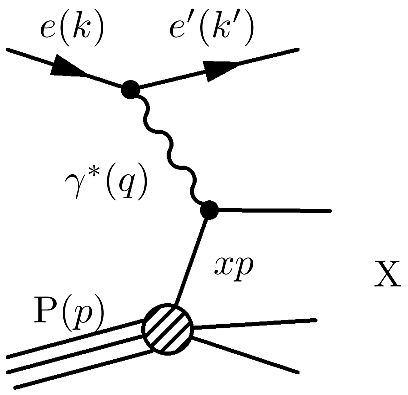

Figure 1.1: Schematic picture of the deep inelastic scattering process.

Two of the three mentioned Lorentz invariant variables are independent since the following approximate relation holds

$$Q^2 = xys, \tag{1.4}$$

where s is the square of the center of mass energy defined as $s = (k+p)^2$. Neglecting the masses of the interacting particles, the center of mass energy can be evaluated as $s = 4E_eE_p$, where E_e and E_p is the energy of the electron and the proton beam, respectively.

In addition, it is convenient to define the following Lorentz invariant variable

$$W^2 = (q + p)^2, \tag{1.5}$$

which is the total mass squared of the hadronic final state (or invariant mass of the virtual boson-proton system) squared and the following relation holds

$$W^2 = \frac{1 - x}{x}Q^2 + M_p^2. \tag{1.6}$$

1.2 DIS cross section

The inclusive NC DIS cross section, for $ep \to eX$, can be calculated from the tensor product

$$\sigma \sim L_{\mu\nu}W^{\mu\nu}, \tag{1.7}$$

where $L_{\mu\nu}$ is the leptonic tensor which is known from QED. Due to the finite structure of the proton the hadronic tensor $W^{\mu\nu}$ is not completely known and can be expressed in terms of proton structure functions $F_2(x, Q^2)$ and $F_L(x, Q^2)$ (for more details see Appendix A). The double differential NC DIS cross section then reads

$$\frac{d^2\sigma}{dxdQ^2} = \frac{2\pi\alpha^2}{Q^4 x} Y_+ \left[F_2(x, Q^2) - \frac{y^2}{Y_+} F_L(x, Q^2) \right], \qquad Y_+ = 1 + (1-y)^2. \tag{1.8}$$

The longitudinal structure function $F_L(x, Q^2)$ is proportional to the absorption cross section of longitudinally polarized virtual photons while the structure function $F_2(x, Q^2)$ contains contributions both from longitudinally and transversally polarized photons:

$$F_2(x, Q^2) = \frac{Q^2}{4\pi^2\alpha}(\sigma_T(x, Q^2) + \sigma_L(x, Q^2)) \tag{1.9}$$

$$F_L(x, Q^2) = \frac{Q^2}{4\pi^2\alpha}\sigma_L(x, Q^2). \tag{1.10}$$

A quantity representing the ratio of the longitudinal and the transverse cross sections is

$$R(x, Q^2) = \frac{\sigma_L(x, Q^2)}{\sigma_T(x, Q^2)} = \frac{F_L(x, Q^2)}{F_2(x, Q^2) - F_L(x, Q^2)}. \tag{1.11}$$

As can be seen from equations (1.9) and (1.10), the condition that longitudinal and transversal cross sections must be positive constrains the structure functions as

$$0 \leq F_L(x, Q^2) \leq F_2(x, Q^2). \tag{1.12}$$

By convention, the term in brackets in eq. (1.8) is denoted as the *reduced cross section*

$$\sigma_r = F_2(x, Q^2) - \frac{y^2}{Y_+} F_L(x, Q^2). \tag{1.13}$$

In most of the kinematic region accessible by HERA it is proportional to $F_2(x, Q^2)$. The contribution of the longitudinal structure function $F_L(x, Q^2)$ is sizeable only at very high values of inelasticity y, due to the kinematic term y^2/Y_+.

1.3 Quark parton model

In 1968, Feynman proposed a model of the proton in which the inelastic lepton-nucleon scattering is represented as quasi-free scattering from point-like constituents, called *partons*, within the proton, viewed from a frame in which the proton has infinite momentum. In such a frame the transverse momenta of partons can be neglected with respect to the longitudinal ones. The momentum of a parton is given as $p' = \eta p$. Neglecting particle masses the scaling variable η coincides with Bjorken x as introduced in the previous section. In deep inelastic scattering these transverse components can be also safely neglected in the calculation of the cross section, which can be then written as the *incoherent sum* of cross sections from scattering off individual charged partons.

Considering the deep inelastic scattering at large four momentum transfer squared $Q^2 \gg M_p^2$ and neglecting the F_L contribution, the double differential cross section can be written as

$$\frac{d^2\sigma}{dxdQ^2} = \frac{4\pi\alpha^2}{Q^4}\frac{F_2(x,Q^2)}{x}, \tag{1.14}$$

to be compared with elastic scattering on a point-like target with electric charge e_p

$$\frac{d^2\sigma}{dxdQ^2} = \frac{4\pi\alpha^2}{Q^4}e_p^2. \tag{1.15}$$

Feynman wrote down $F_2(x,Q^2)/x$ in terms of parton densities $d_i(x)$ describing the probability distribution to find within the proton a parton specie i with momentum fraction x of the proton momentum and with electric charge e_i

$$\frac{F_2(x)}{x} = \sum_i e_i^2 d_i(x) \Rightarrow F_2(x) = \sum_i e_i^2 x d_i(x) \tag{1.16}$$

Denoting $q_i(x)$ as parton densities for quarks and $\bar{q}_i(x)$ for corresponding anti-quarks, the basic formula, expressing F_2 in terms of quark densities, is written as

$$F_2(x) = \sum_i e_i^2 x[q_i(x) + \bar{q}_i(x)]. \tag{1.17}$$

In the QPM the proton structure function is independent of the scale Q^2 and determined as the sum of quark densities within the proton weighted by their momentum fraction and square of the corresponding electric charge.

Due to helicity and momentum conservation, and neglecting the intrinsic transverse momentum of partons, longitudinally polarized photons can not be absorbed by spin 1/2 partons. Thus $F_L(x,Q^2)$ is predicted to be zero in the QPM framework.

The model also predicts that the integral over all momenta, carried by charged partons within the proton, is equal to one

$$\sum_i \int_0^1 x(q_i(x) + \bar{q}_i(x)) = 1, \tag{1.18}$$

where the summation is over all quark species in the proton. It was shown about 30 years ago by experiment that quarks carry only about 50% of the proton momenta and thus another parton specie, electrically neutral, must exist within the proton, subsequently identified with gluons.

1.4 Quantum chromodynamics and DIS

In deep inelastic scattering experiments expectations of the naive quark parton model, namely the prediction of a vanishing longitudinal structure function F_L, the independence of the structure function F_2 of Q^2 and the momentum sum rule (1.18), were found to be violated. Instead, it was observed that F_2 has a weak logarithmic dependence on Q^2 and F_L is non-zero. Furthermore the sum over the quark momenta was measured to be only about 1/2. Hence, a more evolved theory was required to describe experimental facts and the naive QPM was successfully modified within the framework of *Quantum Chromodynamics* (QCD) while maintaining the meaning of its basic concepts.

Quantum Chromodynamics is a gauge field theory describing strong interactions of quarks via intermediate massless vector bosons called *gluons*. Due to the *non-Abelian*[1] nature of the theory the strong force involves a new quantum number, *color charge*. Quarks carry color, conventionally denoted as r (red), g (green) and b (blue) while anti-quarks carry corresponding anti-color. In this picture, gluons carry combinations of colors, for instance $g\bar{b}$. Unlike in QED, where photons are electrically neutral, the color charge of gluons enables gluons to couple to themselves, which is a result of the non-Abelian character of QCD. This fundamental difference, compared to QED, has large consequences.

In the Quark Parton Model, the lepton-nucleon interaction at short distances is represented as the scattering from quasi-free partons within the proton. This implies that the coupling strength of the interaction is weak in the short-distance, high momentum transfer regime. On the other hand, no free quarks have been observed, implying the coupling strength must be large in the long distance, low momentum transfer regime, leading to the confinement of quarks in hadrons. Thus in the theory, accounting for this effect, the coupling strength is varying with the momentum transfer. Conventionally this behaviour of the coupling strength is referred to as *running coupling constant*.

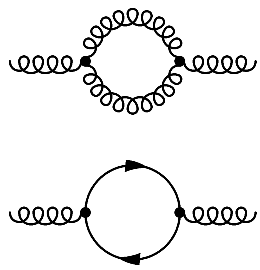

Figure 1.2: Subset of loop diagrams involved in the evaluation of the β function, see text below.

In quantum field theory the scale dependence of the coupling constant is due to the fact that infinities arise, for example due to loop diagrams in boson propagators, where the momentum is not fixed by energy conservation (see Figure 1.2). These infinities are called *ultraviolet divergencies* and can be removed from the theory by a renormalization procedure, where a renormalization scale μ_r^2 is introduced at which ultraviolet divergencies are subtracted off. Thus the strong coupling constant depends on the renormalization scale μ_r^2.

However, the physical observables should not depend on the renormalization scale μ_r^2 when calculated to all orders of perturbation theory. Thus every explicit dependence of an observable R on μ_r^2 must be cancelled by the dependence of α_s on μ_r^2. This requirement can be mathematically expressed as

$$\mu_r^2 \frac{dR}{d\mu_r^2} = \mu_r^2 \frac{\partial R}{\partial \mu_r^2} + \mu_r^2 \frac{\partial \alpha_s}{\partial \mu_r^2} \frac{\partial R}{\partial \alpha_s} = 0. \tag{1.19}$$

This equation is called the *renormalization group equation*. In perturbative QCD, the physical quantities are computed to a given order. Due to missing higher order diagrams the observables

[1]Non-Abelian means that the elements of the corresponding algebra do not commute with each other.

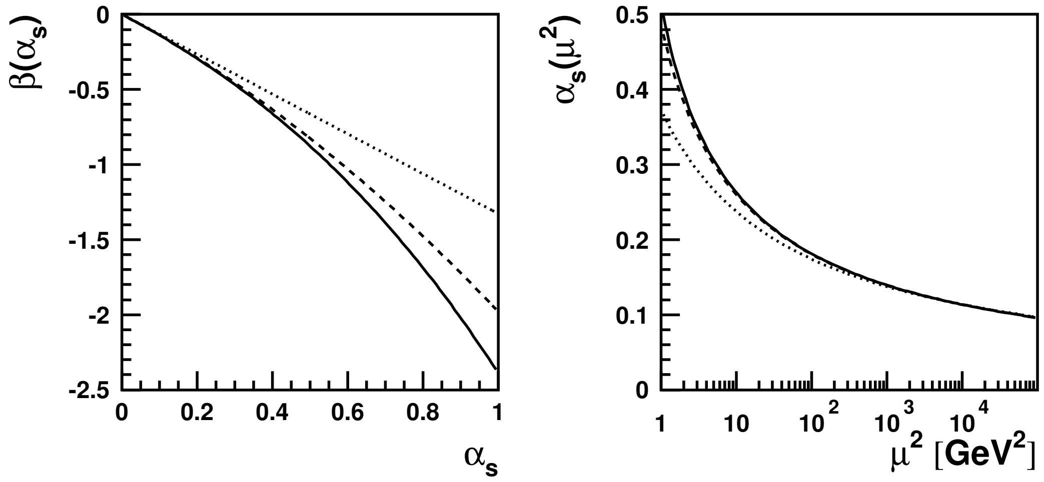

Figure 1.3: Beta function as defined in eq. (1.20) for different orders in α_s (left) and numerical solution for $\alpha_s(\mu^2)$ at fixed $\alpha_s(M_Z^2)$ (right). Full lines correspond to the β function evaluated to order α_s^3 (NNLO), dashed lines to order α_s^2 (NLO) and the dotted lines to the first order in α_s (LO).

contain residual dependence on the renormalization scale, which should be accounted for when theoretical errors are estimated in QCD analyzes.

The renormalization scale dependence of the strong coupling constants α_s is determined in QCD. The logarithmic derivation $\partial\alpha_s/\partial\ln\mu^2$ from the second term in eq. (1.19) can be expressed as a power series in α_s and corresponding coefficients, so called β functions, which can be calculated in QCD:

$$\begin{aligned}
\frac{\partial\alpha_s}{\partial\ln\mu^2} &= \alpha_s\beta(\alpha_s) = -\frac{\beta_0}{4\pi}\alpha_s^2 - \frac{\beta_1}{8\pi^2}\alpha_s^3 - \frac{\beta_2}{128\pi^3}\alpha_s^4 - ... \qquad (1.20)\\
\beta_0 &= 11 - \frac{2}{3}n_f \\
\beta_1 &= 51 - \frac{19}{3}n_f \\
\beta_2 &= 2857 - \frac{5033}{9}n_f + \frac{325}{27}n_f^2
\end{aligned}$$

where the first two coefficients β_0 and β_1 are independent of the choice of the renormalization scale while the coefficients of terms proportional to α_s^n for $n > 3$ depend on the choice of the renormalization scale.

In the leading one-loop approximation, i.e. considering only the β_0 term in eq. (1.20), the solution of the renormalization group equation can be written in the following analytic form

$$\alpha_s(\mu_r^2) = \frac{\alpha_s(\mu_0^2)}{1 + b\cdot\alpha_s(\mu_0^2)\ln(\mu_r^2/\mu_0^2)}, \qquad (1.21)$$

where $b = \beta_0/4\pi$ and μ_0^2 is a reference scale. Referring to eq. (1.20), one can notice that β_0 consists of two terms with opposite sign, one of them depending on the number of quark flavors n_f. The first term (+11) is due to the gluon self-coupling (see Figure 1.2 top). It gives rise to anti-screening effects and hence to the rise of the strong coupling constant towards low μ_r^2. Such a term is absent in QED. The second term, involving $-\frac{2}{3}n_f$, is an analogy to screening effects in QED and its origin is due to quark loops (see Figure 1.2 bottom). It would eventually give rise to α_s with μ_r^2. However, since the number of quark flavors is six, the strong coupling constant has a decreasing behaviour with increasing μ_r^2.

At next-to-leading order (NLO), i.e. including the contribution of β_1 in eq. (1.20), an analytic solution exists as well. A comparison with the leading order solution and with NNLO (involving the term with β_2) is shown in Figure 1.3. One observes a relatively large correction of the NLO solution compared to the leading order solution, while adding one more order (full line) has a much smaller effect.

The NLO analytic solution of the renormalization group equation is often approximated by the log-log solution in the following form

$$\alpha_s(\mu_r^2) = \frac{1}{b \cdot \ln(\mu_r^2/\Lambda_{QCD}^2)} \left[1 - \frac{b}{b'} \frac{\ln\ln(\mu_r^2/\Lambda_{QCD}^2)}{\ln(\mu_r^2/\Lambda_{QCD}^2)} \right], \tag{1.22}$$

where $b' = \beta_1/4\pi\beta_0$ and Λ_{QCD} is a fundamental constant of QCD, ranging from $100 - 300\,\mathrm{MeV}$ and depending on the number of active quark flavors considered. This approximation is enough precise for $\mu_r^2 > m_c^2$, where m_c^2 is the mass of the c-quark.

1.5 QCD evolution

In Figure 1.5 the proton structure function $F_2(x, Q^2)$ is shown as a function of Q^2 for various values of fixed x. It is seen that the scaling behaviour, expected in the naive QPM, is observed only for values of Bjorken x about 0.13. In all other x-regions F_2 depends about logarithmically on Q^2. Furthermore, there is a strong dependence of F_2 on Bjorken x itself which is changing with Q^2, as it can be seen in Figure 1.4.

The physical picture of the scaling violation seen in Figure 1.5 is that the higher the virtuality of the exchanged photon is, the smaller structures in the proton can be probed. If the proton would consist only of valence quarks, no further structure would be revealed when smaller distances would be probed. In QCD, the proton is modelled as an object with large internal activity, where quark-antiquark pairs are created and annihilated in the sea of gluons. Hence, the proton reveals a rich structure when it is probed at smaller distances, corresponding to larger Q^2 scales.

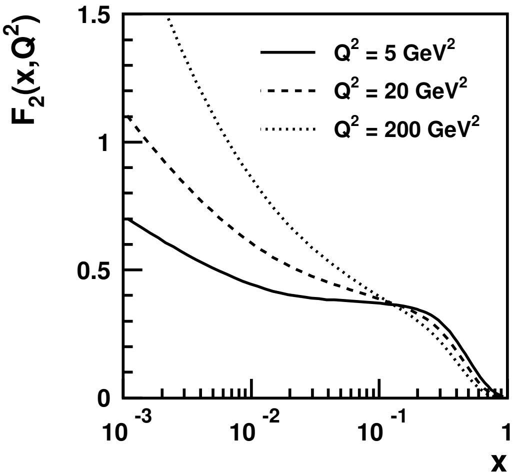

Figure 1.4: The proton structure function $F_2(x, Q^2)$ as a function of Bjorken x.

Although the scaling violation of the structure functions is expected in QCD, due to the overly difficult calculation of an exact result it must be evaluated approximately. Two models of evolution of the parton densities inside the proton are established and

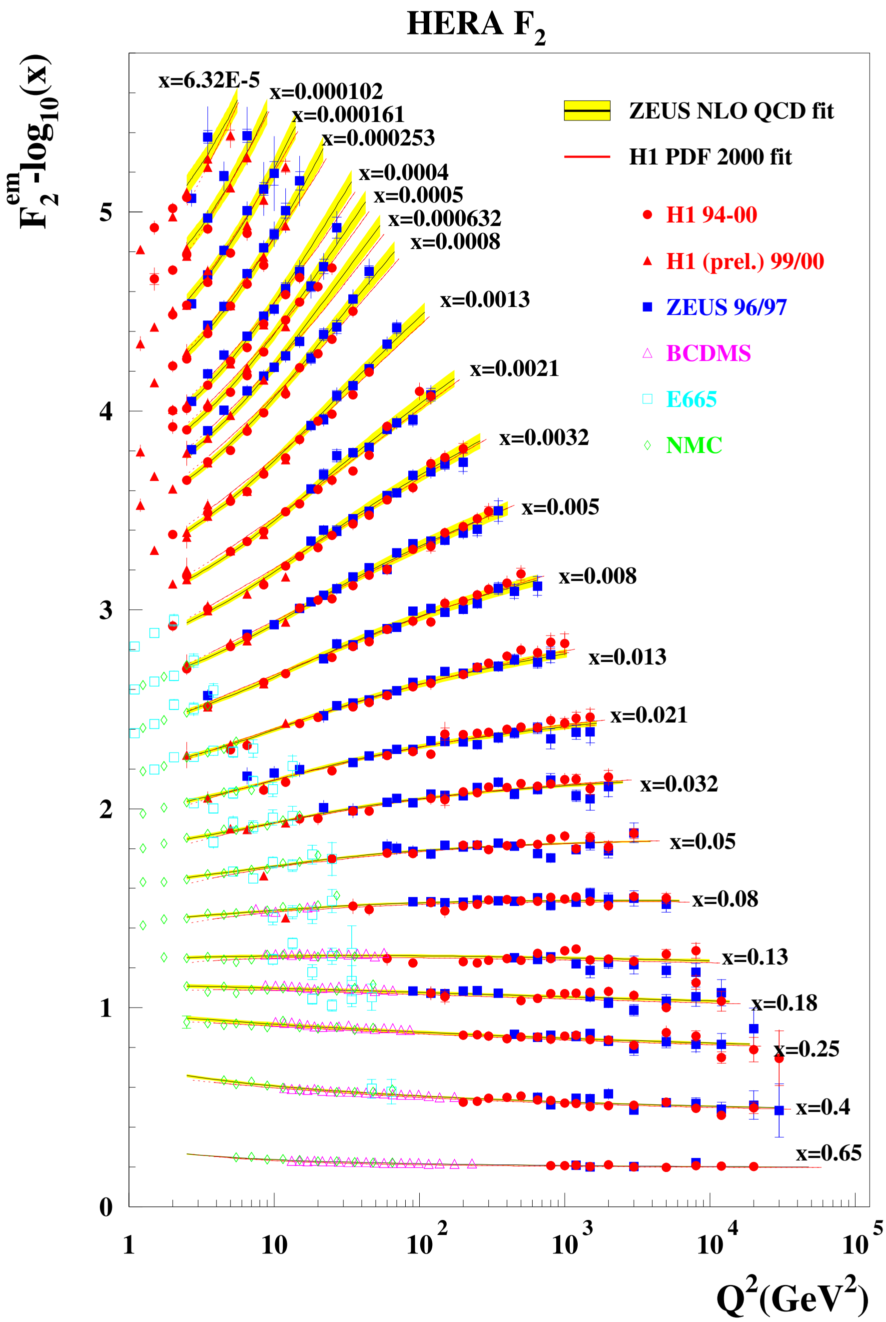

Figure 1.5: Measurement of the proton structure function $F_2(x, Q^2)$ as a function of Q^2 in bins of x by various fixed target and collider experiments. Lines correspond to NLO QCD fits by the ZEUS (black) and the H1 (red) experiment.

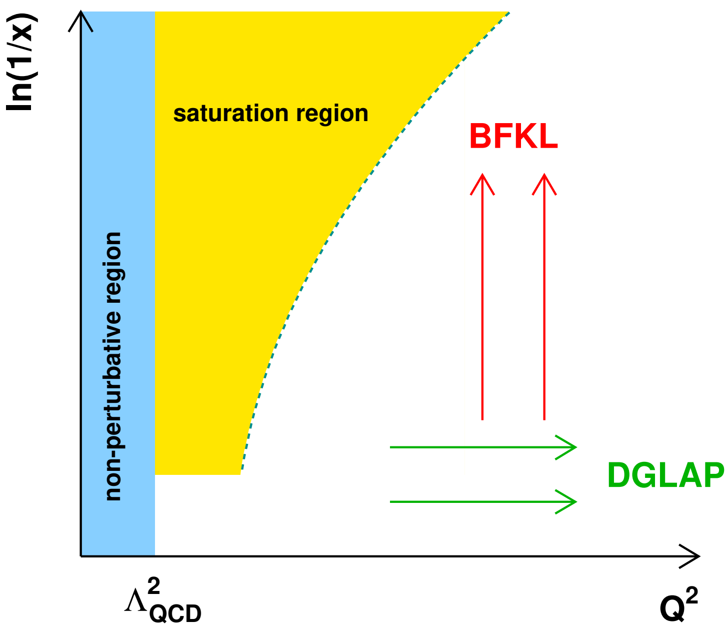

Figure 1.6: Schematic phase space diagram for deep inelastic scattering. Directions of DGLAP and BFKL evolutions are marked by arrows. In the non-perturbative region $Q^2 < \Lambda^2_{QCD}$ (blue rectangle) the coupling is large and not much is known here in terms of perturbative QCD. The saturation region (yellow area) can be understood by means of perturbative methods at low x.

will be briefly discussed in this section, termed as DGLAP [4, 5] and BFKL [6], which model the evolution of $F_2(x, Q^2)$ with Q^2 and x, respectively. An approximation lies in the fact that the models use only appropriate leading terms of the full QCD expansion. Thus the models may work only in a limited part of phase-space.

Another model, the CCFM approximation [7], attempts to combine features from both the DGLAP and BFKL approximations and provides a satisfactory description of many aspects of the data in a wide kinematic region.

The DGLAP, BFKL and CCFM evolutions describe the evolution of parton densities with Q^2 and/or with x via quark and gluon splitting thus generating increasingly rising density at low x. However, it is important to consider that at very high gluon densities, the gluons can recombine via the recombination process $gg \to g$ and thus damp the rise of $F_2(x, Q^2)$ towards low x. This process is within the DLLA framework taken into account in the GLR approximation [8].

1.5.1 DGLAP evolution

In the DGLAP (Dokshitzer, Gribov, Lipatov, Altarelli and Parisi) approximation [4, 5], only powers of $\alpha_s \ln(Q^2/Q_0^2)$ from the perturbative QCD expansion are considered in the *leading logarithm* approximation. Thus this approximation is valid only at large enough Q^2 where α_s is small and $\ln(1/x)$ terms are not important.

The evolution of quark and gluon densities with Q^2 is given by the following coupled equations

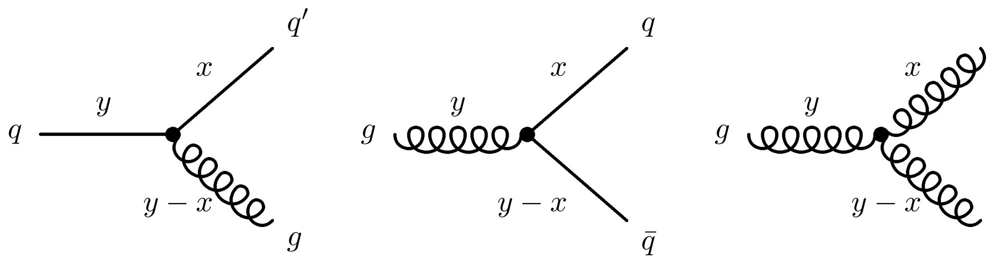

Figure 1.7: Graphs of the leading order DGLAP splitting functions $P_{ij}^{(0)}(x/y)$ for P_{qq} $(q \to qg)$, P_{qg} $(g \to q\bar{q})$ and for P_{gg} $(g \to gg)$ splittings (from left).

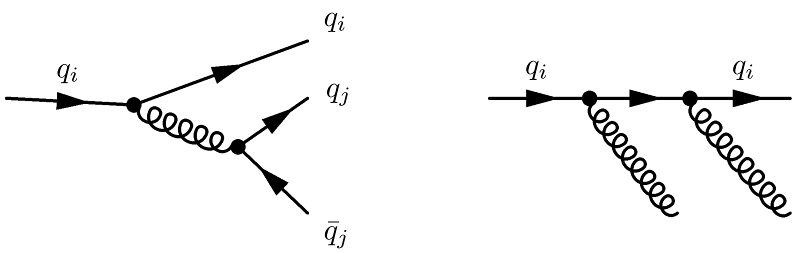

Figure 1.8: Feynman diagrams contributing to the NLO splitting functions $P_{qq}^{(1)}$ and $P_{\bar{q}q}^{(1)}$.

$$\frac{dq_i(x,Q^2)}{d\ln Q^2} = \frac{\alpha_s}{2\pi}\int_x^1 \frac{dy}{y}\left[\sum_j q_j(y,Q^2)\ P_{q_iq_j}\left(\frac{x}{y}\right) + g(y,Q^2)\ P_{q_ig}\left(\frac{x}{y}\right)\right], \tag{1.23}$$

$$\frac{dg(x,Q^2)}{d\ln Q^2} = \frac{\alpha_s}{2\pi}\int_x^1 \frac{dy}{y}\left[\sum_j q_j(y,Q^2)\ P_{gq_j}\left(\frac{x}{y}\right) + g(y,Q^2)\ P_{gg}\left(\frac{x}{y}\right)\right]. \tag{1.24}$$

The functions $P_{ij}(x/y)$ are the *splitting functions* (see Figure 1.7) describing, in their leading order, the probability to find a parton of specie i with momentum fraction x within a parton specie j with momentum y. For simplicity, q_i denote quark densities as well as anti-quark densities.

The functions $P_{ij}(x/y)$ are calculable in perturbative QCD as a power series of $\alpha_s(Q^2)$

$$P_{ij}\left(z,\alpha_s(Q^2)\right) = P_{ij}^{(0)}(z) + \frac{\alpha_s}{2\pi}P_{ij}^{(1)}(z) + ... \tag{1.25}$$

The functions $P_{ij}^{(n)}$ are presently known up to order $n = 2$, in the so called next-to-next-to-leading order approximation (NNLO). Examples of NLO Feynman diagrams are shown in Figure 1.8.

The evolution equations (1.23) and (1.24) look particularly simple when written in terms of moments. The nth-moment of a function $f(x)$ is defined as

$$f(n) = \int_0^1 x^n f(x)dx. \tag{1.26}$$

The re-written evolution equations describing the convolution of a density and a splitting function lead to a simple multiplication in momentum space:

$$\frac{dq_i(n,Q^2)}{d\ln Q^2} = \frac{\alpha_s}{2\pi}\left(\sum_j P_{q_iq_j}(n)q_i(n,Q^2) + P_{q_ig}(n)g(n,Q^2)\right), \quad (1.27)$$

$$\frac{dg(n,Q^2)}{d\ln Q^2} = \frac{\alpha_s}{2\pi}\left(\sum_j P_{gq_j}(n)q_i(n,Q^2) + P_gg(n)g(n,Q^2)\right). \quad (1.28)$$

Due to the probabilistic interpretation of the leading order splitting functions $P_{ij}^{(0)}$ these are positive for $x < 1$ and satisfy the following sum rules

$$\int_0^1 P_{qq}^{(0)}(z)dz = 0, \quad (1.29)$$

$$\int_0^1 z[P_{qq}^{(0)}(z) + P_{gq}^{(0)}(z)]dz = 0, \quad (1.30)$$

$$\int_0^1 z[2n_f P_{qg}^{(0)}(z) + P_{gq}^{(0)}(z)]dz = 0, \quad (1.31)$$

which correspond to quark number and momentum conservation.

An important feature of the DGLAP evolution is the strong ordering in momentum transfer squared and weak ordering in longitudinal momenta

$$Q^2 \gg k_{T,n}^2 \gg k_{T,n-1}^2 \gg ... \gg Q_0^2, \quad (1.32)$$

$$x < x_n < x_{n-1} < ... < x_1, \quad (1.33)$$

where Q_0^2 is the starting scale, typically of order of few GeV^2.

1.5.2 BFKL evolution

In the BFKL (Balitsky, Fadin, Kuraev, Lipatov) [6] approximation, only terms with powers of $\alpha_s \ln(1/x)$ are considered while terms involving $\alpha_s \ln(Q^2/Q_0^2)$ are neglected in the leading logarithm approximation. Thus BFKL is expected to be a good approximation in a different region than DGLAP, namely at very low x but at Q^2 large enough in order to work with reasonably small values of $\alpha_s(Q^2)$.

Unlike in DGLAP, there is no strong ordering in Q^2 while strong ordering in x, corresponding to time-ordering in the proton rest frame, is required

$$x \ll x_n \ll x_{n-1} \ll ... \ll x_1. \quad (1.34)$$

An *unintegrated gluon distribution* $f(x, k_T^2)$ is for $k_T^2 \neq 0$ defined as

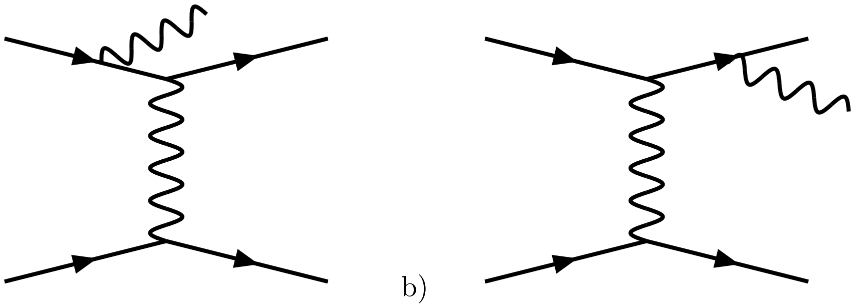

a) b)

Figure 1.9: Feynman diagrams of the first order QED corrections to the lepton-quark scattering corresponding to the initial (a) and final (b) state radiation of a photon from the interacting electron.

$$xg(x, Q^2) = \int_0^{Q^2} \frac{dk_T^2}{k_T^2} f(x, k_T^2), \tag{1.35}$$

for which the BFKL evolution equation reads

$$\frac{df(x, k_T^2)}{d\ln(1/x)} = \int dk_T'^2 K_L(k_T^2, k_T'^2) f(k_T^2, k_T'^2) = K_L \otimes f = \lambda f, \tag{1.36}$$

where $\otimes$ stands for convolution and K_L is the *Lipatov kernel* representing the sum over powers of $\alpha_s ln(1/x)$ terms. From the last equality in eq. (1.36) it is obvious that the function f follows a *power-law* behaviour in the variable x. The resulting gluon distribution can be expressed as

$$xg(x, Q^2) \sim f(Q^2) x^{-\lambda}. \tag{1.37}$$

Hence, the behaviour of the structure function is predicted to be proportional to $x^{-\lambda}$ (for a dominant gluon contribution) although the constant λ is not well constrained. It's value in the next-to-leading logarithm approximation (NLLA) is $\lambda \sim 0.17$ [9] while in the leading logarithm approximation (LLA) it is $\lambda = \frac{12\ln 2}{\pi}\alpha_s \sim 0.5$ [6].

1.6 Radiative QED corrections

Radiative QED corrections to the deep inelastic scattering are due to the emission of real photons, virtual loops or due to the exchange of an additional virtual photon. They are strongly suppressed by factors proportional to $\alpha_{QED} = 1/137$. However, in some regions of phase-space within the detector acceptance these corrections become important or even dominant.

Three major sources can be distinguished in the leading logarithm approximation (LLA) of QED radiative corrections. When the photon is emitted from the incoming electron almost collinearly, see Figure 1.9 (a), the process is called initial state radiation (ISR). The final state radiation (FSR), Figure 1.9 (b), is an analogy to ISR but the photon is emitted from the scattered electron. A third process is called the QED Compton scattering where the photon is emitted from the interacting electron, as in the case of ISR or FSR, but under large angles while the electron undergoes only a small variation of the direction due to the exchange of the virtual photon in the interaction with the proton. These events have a clear signature since the outgoing electron and the radiated photon occure back to back in the polar angle ϕ.

ISR events may be employed to measure the deep inelastic scattering at values of low Q^2. They are basically regular DIS events with the center of mass energy s decreased by the photon radiation. Hence the kinematics of such events must be reconstructed with a method insensitive to the incoming electron energy and with an account for a different center of mass energy s. Such a method can be e.g. the so called *sigma method* which will be introduced in Section 4.1.

1.7 The rise of $\mathbf{F}_2(x, Q^2)$ at low x

Precision measurements of inclusive cross sections by H1 and ZEUS have revealed a striking property of $F_2(x, Q^2)$, its rapid rise towards low x. The rate of the rise $(\partial F_2/\partial \ln x)$ is proportional to F_2 [10] at $x < 0.01$ thus suggesting a steep *power law* like rise as predicted by BFKL evolution. Such a behaviour, along with the $F_2(x, Q^2)$ increase with Q^2 at fixed low x, is well described by perturbative NLO QCD at $Q^2 \geq 5$ GeV^2. The gluon and quark densities, however, can not continue to rise indefinitely, such a behaviour would lead to violation of unitarity. Further progress in QCD is required to understand the low x behaviour of densities qualitatively, see for example [11].

The rise of $F_2(x, Q^2)$ can be studied using the following structure function derivative

$$\lambda(x, Q^2) = -\left(\frac{\partial \ln F_2(x, Q^2)}{\partial \ln x}\right)_{Q^2} . \tag{1.38}$$

The measurement of this quantity from the last H1 publication [10] is shown in Figure 1.10. Within experimental errors, the structure function derivative $\lambda(x, Q^2)$ does not depend on x, for $x < 0.01$. Thus the structure function $F_2(x, Q^2)$ can be parameterized as $F_2 \propto x^{-\lambda}$ for fixed Q^2. The form is identical to the BFKL approximation as well as to Pomeron [13] based parameterizations, though the λ increase with Q^2 is not predicted. The function $\lambda(Q^2)$ is determined from fits of the form $F_2(x, Q^2) = c(Q^2) \cdot x^{-\lambda(Q^2)}$ to the H1 structure function data, restricted to the region $x < 0.01$. Results are shown in Figure 1.11.

1.8 Saturation model

The saturation model of Golec-Biernat and Wüsthoff (GBW) [14, 15] is based on the *color dipole model* approach. In this model, the photon interacting with the proton can be described in the proton rest frame as a $q\bar{q}$ pair interacting with the gluonic content of the proton. An interesting feature of the model is that the cross section of the $q\bar{q}$ dipole interaction with the proton saturates at large separation distance of the quarks. This situation happens in two cases:

1. When $Q^2 \to 0$ the cross section of $\gamma^\star p$ interaction must tend to a constant and thus $F_2 \to 0$.

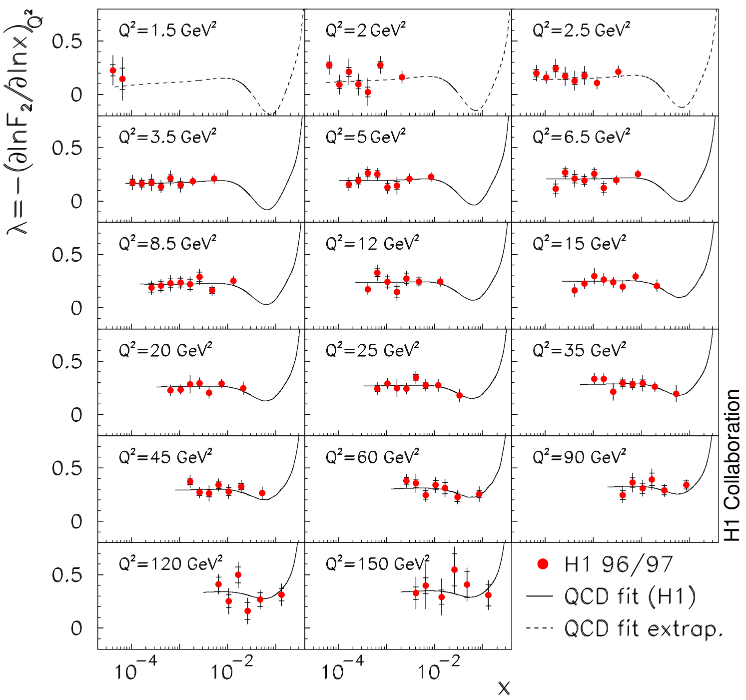

Figure 1.10: Measurement of the structure function derivative $\lambda(x, Q^2)$ [10]. The solid lines represent the NLO QCD fit to the H1 data [12] and the dotted lines represent the extrapolation of the QCD fit below $Q^2 = 3.5$ GeV^2.

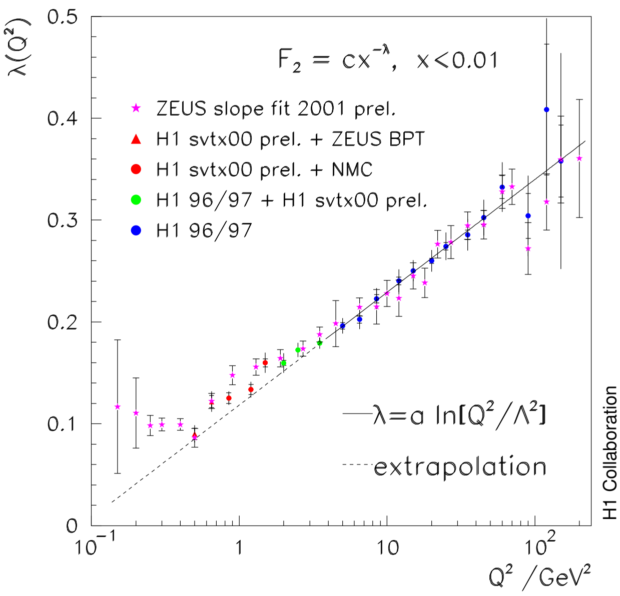

Figure 1.11: Determination of the function $\lambda(Q^2)$ from fits of the form $F_2(x, Q^2) = c(Q^2) \cdot x^{-\lambda(Q^2)}$ to F_2 structure function data. The straight line corresponds to a fit of the form $a \ln[Q^2/\Lambda^2]$ using H1 data (blue points) for $Q^2 \geq 3.5$ GeV^2, the dashed line to its extrapolation to lower values of Q^2.

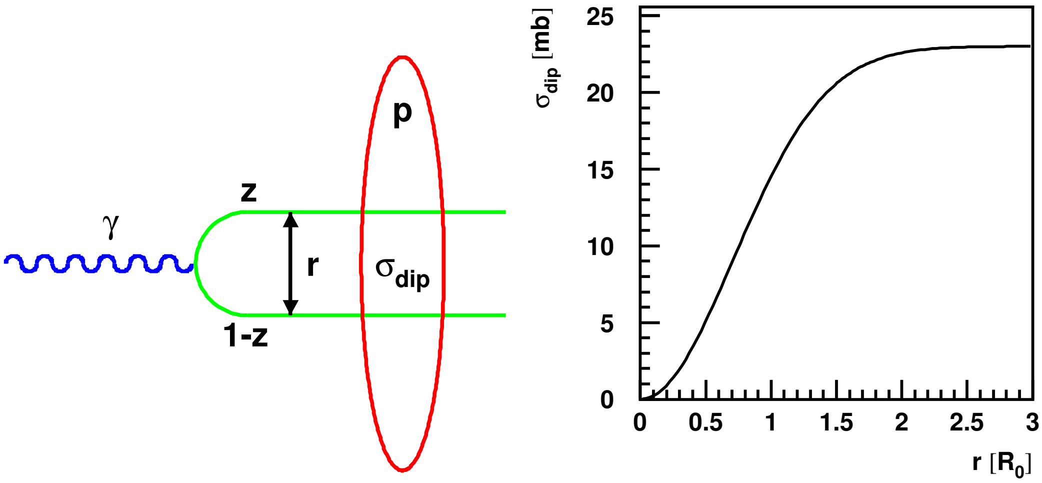

Figure 1.12: Dipole picture of $\gamma^\star p$ scattering (left) and dependence of the dipole cross section σ_{dip} on the size of the dipole r (right).

2. When $x \to 0$ partons within the proton are expected to saturate via particle recombination.

The $\gamma^\star p$ interaction cross section can be written as

$$\sigma_{T,L}^{\gamma\star p}(x, Q^2) = \int dz\ d^2\mathbf{r}\ |\Psi_\gamma^{T,L}(z, \mathbf{r})|^2\ \hat{\sigma}(x, r), \tag{1.39}$$

where $r \sim 1/Q^2$ is the transverse size of the dipole, z is the momentum fraction of the photon carried by the quark (see Figure 1.12) and $\Psi_\gamma^{T,L}$ is the photon wave function for transverse and longitudinal polarization, respectively. In the GBW model the dipole cross section is expressed as

$$\hat{\sigma}(x, r) = \sigma_0 \left[1 - exp\left(-\frac{r^2}{R_0^2(x)}\right),\right] \tag{1.40}$$

where $R_0^2(x)$ is the x-dependent *saturation radius*,

$$R_0^2(x) = \frac{1}{Q_0}\left(\frac{x}{x_0}\right)^{\frac{\lambda}{2}}, \tag{1.41}$$

where Q_0^2 is 1 GeV^2. In order to reach the photoproduction limit, the Bjorken variable x was modified to be

$$x = \frac{Q^2 + 4m_q^2}{W^2}, \tag{1.42}$$

where m_q is an effective quark mass and W denotes the $\gamma^* p$ center-of-mass energy. Fixing m_q to 140 MeV, the model has three parameters to be determined from the fit to the data: σ_0, λ and x_0. According to [14, 15], these three parameters were found to be

$$\sigma_0 = 23 \text{ mb}, \quad \lambda = 0.29, \quad x_0 = 3 \times 10^{-4}. \tag{1.43}$$

A remarkable feature of the dipole model is its universality. If, for example, the model parameters are determined from F_2 data, because of the fixed structure of the wave functions, the model predicts the longitudinal structure function without additional parameters.

DGLAP improved saturation model

Despite the remarkable success of the GBW saturation model in the description of various soft processes including diffraction, it was revealed that the model has a problem to describe the steep behaviour of F_2 at larger $Q^2 \gtrsim 20$ GeV^2. Hence, a modification of the model was proposed [16], modifying the low r behaviour of $\hat{\sigma}(x,r)$ while preserving saturation at large r. In this modification the effective dipole cross section reads as

$$\hat{\sigma}(x,r) = \sigma_0 \left[1 - exp\left(-\frac{\pi^2\, r^2\, \alpha_s(\mu^2)\, xg(x,\mu^2)}{3\sigma_0}\right)\right], \tag{1.44}$$

where the scale μ^2 is assumed to have the form $\mu^2 = C/r^2 + \mu_0^2$ and $xg(x,\mu^2)$ is the gluon distribution parameterized at initial scale Q_0^2 as

$$xg(x,Q_0^2) = A_g\, x^{-\lambda_g}\, (1-x)^{5.6}. \tag{1.45}$$

The exponent determining the large x behaviour was motivated by the MRST parametrisation of xg [17]. The gluon distribution (1.45) is evolved in LO DGLAP manner, neglecting the quark contributions. Thus the model has four more parameters to be determined from data: C, μ_0^2, A_g and λ_g. It was found [16] that the description of the recent $F_2(x,Q^2)$ data by H1, ZEUS and E665 experiments was significantly improved. While for the original version $\chi^2/ndf \approx 3$, the modified model yields $\chi^2/ndf = 1.18$ preserving the successful description of low Q^2 data and diffraction. A selection cut $x < 0.01$ was applied on $F_2(x,Q^2)$ data in order to avoid valence quark region at large x.

In physical terms the proposed formula (1.44) corresponds to the multiple scattering of the parent dipole on a nucleon with the exchange of two interacting gluons [18].

Chapter 2

Fractal structure of the proton

Although fractals are known for about hundred years, their intensive study started in the last third of the 20th century, with the developments of powerful computers. Benoit Mandelbrot, in his classical book [19], has initiated a wave of interest in fractals, self-repeating objects, usually constructed from simple equations yielding a peculiar richness in shape and structure (see Figure 2.1). It was found that many processes in nature have much in common with fractality and self-similarity, hence fractals are not only mathematical objects that look good and can be profitably used in computer graphics, but there is a deeper connection with nature itself.

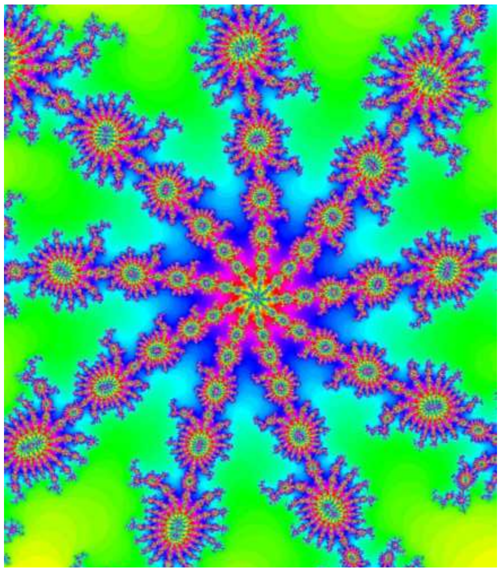

Figure 2.1: Mandelbrot set, constructed by iterating $z = z^2 + c$, where $z \in \mathbb{C}$.

In this Chapter, an introduction to fractal geometry is given in Section 2.1. A brief overview of connections to quantum mechanics is presented in Section 2.2. Finally, Section 2.3 describes a novel application to the proton structure functions which, as will be seen, describe the observed x and Q^2 behaviour over the complete Q^2 range, from the non-perturbative to the truly DIS region.

2.1 Introduction to fractal geometry

The formal definition of the term *fractal* was given by Benoit Mandelbrot [19]. It says that a fractal is a set the *Hausdorff dimension* of which differs from the topological dimension. This abstract definition can be understood more intuitively on an example of a fractal curve (see Figure 2.2). Compared to a normal straight line, the fractal curve is erratic such that in some sense it does not behave like a one-dimensional curve anymore. A characteristic property of such a curve is its self-similarity, i.e. the curve can be divided in sub-sets which are identical (at least statistically) to the original curve but are of different size.

Coming back to the Mandelbrot definition, an important quantity in describing fractals is their Hausdorff (often called fractal) dimension. The original intention of Hausdorff was to define a

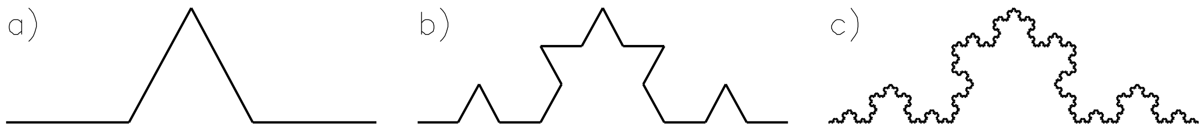

Figure 2.2: Construction of the Koch curve: (a) corresponds to the first iteration, (b) and (c) to the second and the fifth iteration, respectively.

measure being independent of the resolution or scale of a measurement, as well as independent of the shape of the considered object. Since the definition of the Hausdorff dimension is rather abstract, the concept of dimensions can be easier explained using an example of a more practical definition. Consider a curve, which is constructed by iterating in the following way: having an object (called generator) from Figure 2.2a), every line of the object is in a single step exchanged by the object itself but with reduced size. Then the step is repeated with the new object ad infinitum. The resulting curve is the so called *Koch curve* (see Figure 2.2 (c)). It is self-similar by construction, i.e. every little piece is a small copy of the curve itself. There are four copies of the whole curve each 3-times smaller than the curve itself. Alternatively, there are 16 copies of the curve but with size reduced 9-times. The fractal dimension can here be introduced as

$$d_f = \frac{\log(\text{number of self-similar objects})}{\log(\text{magnification factor})}, \tag{2.1}$$

where by magnification factor we mean how many times a small copy has to be enlarged to reach the size of the whole curve[1]. According to this formula, the dimension of the Koch curve is fractional

$$d_f = \frac{\log 4}{\log 3} = \frac{\log 16}{\log 9} = 1.26186\ldots \tag{2.2}$$

Roughly speaking, the fractal dimension describes how complicated or how large a self-similar object is.

There are further ways how to introduce fractal dimensions for various applications. A useful tool for studies within the framework of quantum mechanics is the notion of *fractal paths.*

Fractal paths

Let us explain the notion of the fractal paths again on the example of the Koch curve. What is the length of such a curve? There were 4 line segments in the first iteration, each of length $a/3$, where a is the total width of the curve. In the second iteration there are 16 line segments but with length $a/9$. In general, for the n-th iteration there are 4^n line segments with length $a/3^n$. Thus the length of the curve is $L = a(4/3)^n$. In the limit $n \to \infty$, the length L diverges with the number of iterations. This is an important observation, typical for fractal curves and paths.

[1]Equivalently, it is possible to use resolution instead of the magnification factor, then $d_f = \frac{\log N}{\log(1/\epsilon)}$, where N is the number of self-similar objects resolved with resolution ϵ.

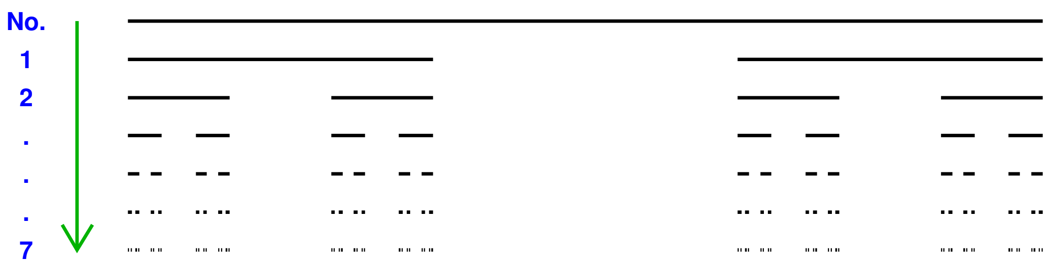

Figure 2.3: Cantor set fractal in iterations number 1-7 (from top). In each iteration step the middle segment is removed from every line.

The length $\Delta l = a/3^n$ represents the resolution under which the structure of the curve can be probed since it corresponds to the length of a line segment in the n-th iteration. This means that more deeper details of the curve are not distinguishable, and the length of the curve at this particular resolution is $L = 4^n \Delta l$. Expressing n in terms of Δl and a one obtains

$$L = 4^n \Delta l = e^{\frac{\log 4}{\log 3} \log \frac{a}{\Delta l}} \Delta l = a^{d_f} \Delta l^{1-d_f} \sim \Delta l^{d_t - d_f}, \tag{2.3}$$

where $d_f = \log 4/\log 3 \approx 1.26$ is the fractal dimension of the curve and $d_t = 1$ is the topological dimension of the generator (for line it is 1). This is another important observation, the measured length of a fractal curve depends on the measurement resolution as a *power law*, characterized by its exponent.

The fact that the fractal dimension d_f can be even smaller than the topological dimension d_t is demonstrated by the so called *Cantor set*, see Figure 2.3. When the number of iterations $n \to \infty$ a set of infinite number of unconnected points is obtained and the total length of the curve $L \to 0$. The fractal dimension of this set is $d_f = \log 2/\log 3 \approx 0.63$ and thus smaller than its topological dimension $d_t = 1$.

An example of a fractal curve with dimension $d_f = 2$ is the *Hilbert curve*. Its sixth iteration is depicted in Figure 2.4. When iterated till infinity the curve eventually covers the whole square as a rigid object, albeit created from a line. This sort of fractal paths[2] is in particular interesting because of its close connection to paths of quantum particles as will be explained in the next section.

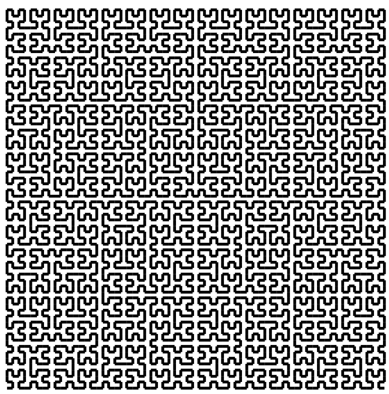

Figure 2.4: Plane-filling Hilbert curve in the sixth iteration.

A popular and most often cited example of a measurement of a fractal curve length is the measurement of the length of a coastline [20, 19]. The measured length is intuitively expected to be different if the smallest scale that one can resolve is 10 km or when it is 1 m such that more details can be included. From the log-log plot of length versus resolution one can obtain the fractal dimension of a particular coastline, which e.g. for the rugged coastline of Norway is $d_f \approx 1.5$ while d_f is close to 1 for the smooth coastline of South Africa.

It is important to note that fractals in nature (e.g. coastlines, trees etc.) have *stochastic* fractal properties, i.e. their statistical characteristics are fractal-like although they are not constructed as exact mathematical objects (as is e.g. the Koch curve).

[2] Another example is e.g. the Peanno curve or Brownian path.

2.2 Quantum mechanics and fractals

Many objects and processes in nature exhibit self-similar properties. An obvious question is: is there any indication that fractality appears in quantum mechanics? The answer is yes. Feynman and Hibbs [21] have shown in 1965 that typical unmonitored quantum paths are non-differentiable curves, stochastically self-similar. Their calculation demonstrates that the paths have fractal dimension $d_f = 2$ in the presence of an arbitrary local potential. Furthermore, they show a close relation to Heisenberg's uncertainty principle and thus to quantum commutation relations, the essence of quantum physics.

An intuitive heuristic argument [22] for a non-relativistic case is the following: according to Heisenberg's uncertainty relation

$$\Delta x \Delta p \sim \hbar, \tag{2.4}$$

where Δp can be expressed as $\Delta p = m(\Delta x/\Delta t)$, after substitution one obtains:

$$(\Delta x)^2 \sim \Delta t. \tag{2.5}$$

Assuming propagation according to such a quantum behavior between two points in spacetime, where the time interval T is divided into N subintervals of length Δt, the following relation for the length of the path holds:

$$L = N\Delta x = \frac{T}{\Delta t}\Delta x \sim \frac{1}{\Delta x}, \tag{2.6}$$

where the last step employs eq. (2.5). Since for fractal paths we have seen that $L \sim (\Delta x)^{1-d_f}$ (see eq. (2.3)), when $\Delta t \to 0$ a comparison with eq. (2.6) gives $d_f = 2$. Thus assuming Heisenberg's relation for massive quantum particles, the resulting quantum path is consistent with a fractal path with fractal dimension $d_f = 2$. The argumentation can be done more rigorous and more generally in the presence of a local potential[3], see [21, 22] or Appendix B of this thesis.

2.2.1 Brownian motion and Schrödinger equation

The Brownian motion describes a motion of a molecule in a liquid of other molecules. Collisions of molecules are changing their momenta which results into a typical pattern (see Figure 2.5) of chaotic trails. The process is very well described assuming that the change of momentum of a molecule depends only on the last collision (locality) and that the process is random (stochasticity). Referring to [22, 23, 24] for details, it can be shown that such a process is stochastically self-similar and that a molecule trail has the fractal dimension $d_f = 2$. An interesting result is that the equality $d_f = 2$ holds independently of the number of space dimensions. The Brownian motion is an example of a microscopic model which is lying beneath a statistically described macroscopic process, called *diffusion*.

Diffusion is a process of everyday experience, for example spreading of chemical smells (e.g. perfumes) in a room, melting of sugar in coffee etc. Statistically, diffusion is described by the so called *diffusion equation*:

[3]For example, for the Compton potential or the harmonic oscillator $d_f = 2$ holds.

$$\left(\frac{\partial}{\partial t} - d\Delta\right) p(\vec{x}, t) = 0, \tag{2.7}$$

where $p(\vec{x}, t)$ is a probabilistic density (or concentration in chemistry applications) and d is the diffusion coefficient describing the velocity of the process.

There is a close relation between diffusion (Brownian motion) and quantum mechanics. As is well known [24, 25], substituting imaginary time ($t \mapsto it$), the Schrödinger equation for free massive particles can be easily re-assembled when the diffusion coefficient $d \mapsto \hbar/2m$

$$\left(\frac{\partial}{\partial t} - \frac{i\hbar}{2m}\Delta\right) \psi(\vec{x}, t) = 0. \tag{2.8}$$

According to this similarity between the two processes, it is not surprising that quantum paths could have similar properties as Brownian trails of molecules in liquid, namely the fractal dimension $d_f = 2$. What is a missing part in this picture is a microscopic model of quantum physics, as is the Brownian motion for the diffusion process.

Figure 2.5: A numerical simulation of Brownian path trail in two space dimensions.

2.2.2 Velocity dependent potentials

The previous discussion of quantum paths having fractal dimension $d_f = 2$ was made with two assumptions: the particle is considered to be point-like[4], following the non-relativistic quantum mechanics equation of motion (Schrödinger equation) in a local potential field. Such a field can be, for example, the Compton potential, the harmonic oscillator or free particle motion as well. Note that local fields change dynamics of the particle motion, while the fractal dimension remains constant. One may ask how the fractal dimension changes for the case of potentials which depend on particle velocity or momenta. This happens for instance when a massive charged particle interacts with the electro-magnetic field or in condensed matter and nuclear physics. In such cases the Lagrangian contains a velocity dependent term, hence, the corresponding action also contains a velocity dependent term.

In the following I shall focus on results. For more details concerning the evaluation of fractal dimensions from action see [22] or Appendix B for the case of a local potential. Suppose that the velocity dependent action reads as

$$S = \int \left(\frac{m}{2}\dot{x}^2 + V_0|\dot{x}|^\alpha + U(x)\right) dt, \tag{2.9}$$

[4]Equivalently this can be expressed as the requirement that the probed scales are much larger than the particle's wavelength.

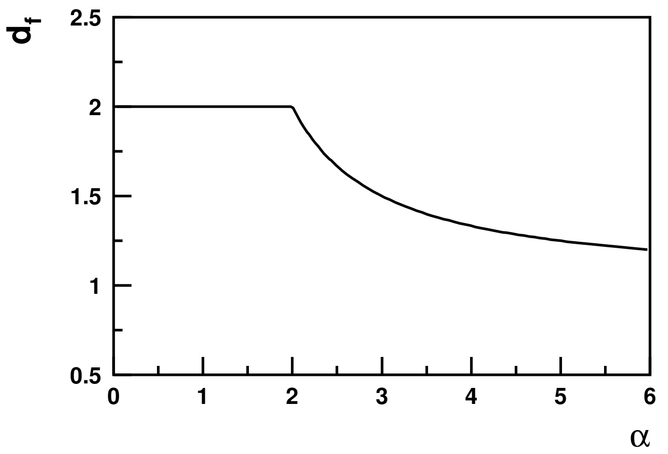

Figure 2.6: Critical exponent (identified with fractal dimension) versus potential parameter α corresponding to velocity dependent action (2.9).

where the second term corresponds to the velocity dependent term in the Lagrangian[5] and $U(x)$ is the local potential. It can be shown [22] that the fractal dimension corresponding to the velocity dependent term is

$$d_f = \frac{\alpha}{\alpha - 1}. \tag{2.10}$$

For $\alpha = 2$ the fractal dimension calculated according to eq. (2.10) agrees with $d_f = 2$ as in the case of pure local potential.

The overall behaviour of the quantum mechanical path dimension according to the action (2.9) is driven by the $\dot{x}$ term with larger exponent. The dependence of d_f on α is shown in Figure 2.6. For $\alpha < 2$ the kinematic term dominates while for $\alpha > 2$ the velocity dependent term takes over. The result is supported by numerical studies [26].

2.2.3 Relativistic quantum mechanics and QFT

Classic quantum mechanics, considered so far in this introduction, gives hints that a study of fractal properties of quantum theories may be useful in deeper understanding the theories themselves. However, in relativistic quantum mechanics and in particular in Quantum field theories the situation is different in many aspects. An important difference is that time is treated equally as a spatial coordinate. Hence, particles can propagate backward in time (antiparticles). In field theories the total number of particles is not conserved and depends on the resolution power of a probe. Furthermore, the position of a particle is not an observable as is the case in classic quantum mechanics. This means the concept of particle paths is not adequate anymore to evaluate fractal dimension of a particle propagation and other non-local measure must be introduced. The situation becomes even more complicated in case of non-abelian field theories as is Quantum Chromodynamics.

Let us briefly summarize attempts and results to evaluate fractal dimensions, i.e. the critical behaviour of a system, in areas outlined above.

[5]However, a non-gaussian form of the velocity dependence in the Hamiltonian does not correspond to the same form in the action due to the Legendre transformation between Hamiltonian and Lagrangian and expressing momentum p by velocity $\dot{q}$. For instance, a p^4 form in the Hamiltonian yields $\dot{q}^{5/4}$ in the action.

Dirac equation

The relativistic Dirac equation was introduced by Dirac to avoid difficulties of non-linear (in space and time) derivatives in the Klein-Gordon equation. It was found to satisfy all requirements of special relativity and quantum mechanics and to describe real quantum systems. For free spin-$\frac{1}{2}$ particle it is written as

$$(i\partial\!\!\!/ - m)\psi = 0, \tag{2.11}$$

where $\partial\!\!\!/$ stands for $\gamma^\mu \partial_\mu$, m is the mass of the particle represented by Dirac bispinor ψ and $\hbar = c = 1$. The Dirac equation is linear in the derivatives.

Various models were proposed in order to understand this equation. Namely, the chessboard model of Feynman [21, 27] or the relativistic random walk models by Kac [28] and Ord [29]. In the latter model, called *spiral model*, one finds that if the random walks occur on a typical length scale Δx which is much larger than the Compton wave length λ, i.e. $\Delta x \gg \lambda$, then $d_f = 2$ as in the non-relativistic quantum mechanics. In the opposite case, when $\Delta x \ll \lambda$, $d_f = 1$ holds and the trajectories are smooth curves.

Quantum Field Theories

As was already mentioned, in quantum field theories the number of particles is not conserved and the position of a particle is not an observable. In order to overcome these difficulties two possible ways were pursued

- The length of propagation can be studied using lattice simulation via the *hopping parameter expansion*. The fractal dimension is estimated from the scaling behaviour of the system when the spacing of the lattice a tends to zero, $a \to 0$.
- A dimensional observable can be introduced, having e.g. the volume as naive dimension. Evaluating this observable in field theory may give a scaling dependence from which it is possible to deduce the corresponding fractal dimension. This way has been applied in quantum gravity.

The first way was employed to study the free Dirac-Wilson fermion propagator on the lattice [30]. The fractal dimension of the fermion propagator was found to depend on its component. For the unitary component the equality $d_f = 2$ holds. Considering the γ_μ component gives $d_f = 1$, i.e. smooth lines and no fractal behaviour. The result is supported by numerical simulations in various numbers of space dimensions. In order to understand the result in the context of the non-relativistic case, the γ_μ component is dominant in the relativistic domain while the unit-matrix component is dominant in the non-relativistic domain. Hence, the low energy non-relativistic approximation is consistent with the previous result, $d_f = 2$, of classic quantum mechanics.

Quantum Chromodynamics

In the previous section, non-interacting fermions were considered. The question may be asked what happens in case of non-abelian quantum field theory as Quantum Chromodynamics which is describing the strong interactions of quarks and gluons. In principle it is possible to extend the definitions of propagation length, used for free fermions, to the case of strongly interacting quarks. However, there are computational difficulties when one tries to evaluate corresponding fractal dimensions numerically.

In Quantum Chromodynamics, the mechanism of quark confinement is a long-distance phenomenon. At small distances, corresponding to large scales μ_f (see QCD Section of this thesis), quarks are almost free particles. On the other hand, at large distances (small scales) the strong interaction sets in and keeps quarks together. Hence, in order to understand confinement the infrared behavior of QCD should be studied. In terms of DIS kinematics it means low four-momentum transfer squared $Q^2 \sim M_p^2$, where $M_p^2 \approx 1$ GeV^2 is the mass of the proton. In other words, the resolution power of the photon probe is comparable to the Compton wave-length of the proton.

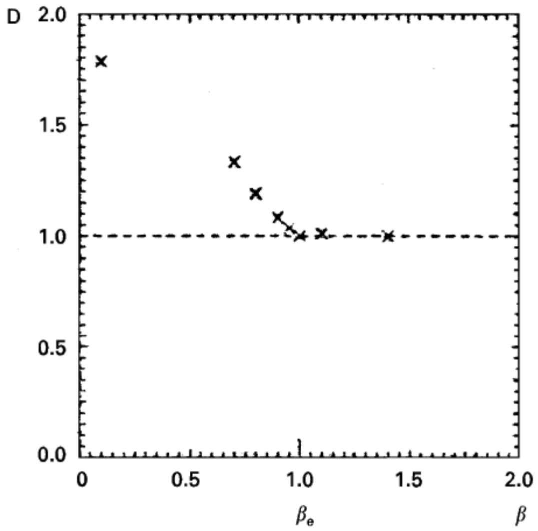

Figure 2.7: Fractal dimension d_f of the monopole current density versus β for U(1) group in 4D. The plot is taken from [31].

To discriminate a confined phase from a non-confined phase a non-local order parameter is used, called Wilson loop[6]. The parameter measures the response of the gauge fields to an external quark-like source passing around its perimeter, along the loop. It was realized that the geometry of the loop (perimeter, area) plays a crucial role. Kröger [32] proposed to use closed fractal paths with $d_f = 2$, similar to Hilbert curve from Figure 2.4, for the geometry of the loops.

The fractal geometry of the closed monopole current loops was suggested to be measured by Polikarpov et al. [33, 31]. The fractal dimension was used as an order parameter to distinguish confined and non-confined phase. In general, results from lattice simulations suggest that the fractal dimension of monopole current loops $d_f \approx 1$ in the non-confined phase, while in the confined phase the monopole current loops are fractal curves with non-trivial dimension $d_f > 1$, see Figure 2.7 for lattice simulation in $D = 4$, group U(1). The non-confined phase corresponds to $\beta > \beta_c$ while the confined phase corresponds to $\beta < \beta_c$, where $\beta_c \approx 1$.

2.2.4 Measurements of fractal dimensions

As can be seen from the previous section, there are various suggestions that fractal geometry may play a role in quantum field theories. However, the motivation is coming from theory and lattice simulations rather than from experimental measurements. Before outlining feasible ways to measure quantum systems geometry, let us ask the following apparent question:

Why is it interesting at all to measure fractal geometry and dimensions of quantum systems?

There is a couple of reasons at hand:

[6]Alternative loops are e.g. Polyakov loop and the 't Hooft loop.

- It was shown that fractal dimensions are related to the commutation relations, which can not be measured directly.

- Fractal dimensions depend on the action, hence their evaluation could give additional information on the content of the Lagrangian.

- There is a fundamental question about monitored and unmonitored quantum behaviour, namely dimensions of quantum paths. In other words, what part of the observed result is generated by the measurement itself and what would be the quantum system without the measurement interaction.

- It was demonstrated that the fractal dimension could be used as an order parameter to distinguish between the confined and non-confined phase.

- Phenomenological models based on fractal geometry can be constructed in order to describe various phenomena of quantum physics.

- A most apparent reason is that the real quantum systems may not have much in common with fractal geometry and thus an experimental measurement is essential to clarify this question.

An experiment to measure the fractal dimension of a free particle was proposed by Abbot and Wise [34]. The idea is that a path of an emitted electron is monitored using a source of light. The emitted electron is passing a sequence of screens with several holes in each of them. A photon from the light source between the screens eventually collides with the electron so that by measuring the scattered photon one can deduce by which hole the electron has passed and hence the topology of its trajectory. However, since the electron undergoes an interaction with the photon, results from this experiment could be interpreted as the erratic fractal path of the electron is created by monitoring of the electron rather than to be inherited property of an electron path. An alternative experiment, which avoids the problem of monitored versus free path geometry, was suggested by Kröger [35].

In the field of QCD, deep inelastic scattering is an apparent candidate for a fractal dimension measurement of the strong interacting particles within the proton. In DIS experiments, the exchanged photon with four-momentum transfer squared Q^2 can resolve structures of spatial size $\sim 1/Q$. Thus by changing Q^2 one can zoom into the structure of the proton. In a similar way also the Bjorken x variable can be employed. Its interpretation as the momentum fraction carried by a struck particle within the proton, consequently, allows to probe the structure of the proton in momentum space.

2.3 Fractal model of the proton structure

The fractal structure within the proton may be investigated by constructing a naive model, reflecting self-similarity, which can be fitted to the data [3, 36]. Before coming to that, it is useful to define dimensions for densities and to introduce a framework in which the model is built.

2.3.1 Densities and fractal dimension

The definition of a dimension, given in eq. (2.1), may be generalised for the case of non-discrete fractals. In this generalisation, the magnification factor is a real number z and the number of self-similar objects is represented by a density function $f(z)$. Taking into account that the dimension may change with scaling, a *local dimension* is defined as

$$d_f(z) = \frac{\partial \log f(z)}{\partial \log z}. \tag{2.12}$$

For ideal mathematical fractals, discussed in the previous section, $d_f(z)$ is constant for the whole fractal. Introducing a scale dependent dimension is natural because many fractals in nature (e.g. plants or coastlines) are not mathematically ideal and usually have a fractal structure only within a certain region of magnification. In such a region, the dimension is approximately constant, $d_f(z) = d$, and, following eq. (2.12), the density function $f(z)$ reads as

$$\log f(z) = d \cdot \log z + d_0, \tag{2.13}$$

where d_0 defines the normalisation. Hence, $f(z)$ has a *power law* behaviour, $f(z) \propto z^d$.

More generally, fractals may have e.g. two *independent* magnification factors, z and y. In this case the density $f(z, y)$ is written in the following way

$$\log f(z, y) = d_{zy} \cdot \log z \cdot \log y + d_z \cdot \log z + d_y \cdot \log y + d_0. \tag{2.14}$$

Here the dimension d_{zy} represents the dimensional correlation relating the z and y factors. The function $f(z, y)$ satisfies a power law behaviour in z for fixed y and in y for fixed z as well. The correlation term is the only term that can be added without violating the power law scaling in both z and y.

A feature, which deserves to be mentioned, is that there is a certain freedom in selecting magnification factors without changing a shape of the function $f(z, y)$. It is possible to use any non-zero power of a factor multiplied by a constant: $z \to az^\lambda$. The only effect of such a change is a redefinition of the dimensional parameters $d_{\{z,y,zy\}}$ and of the normalisation d_0, respectively.

2.3.2 Model construction

In quantum chromodynamics the behaviour of the sea quark densities is driven by gluon emissions and splittings. The deeper the proton structure is probed, the more gluon-gluon interactions can be observed. These, in analogy to fractals, may follow self-similarity, i.e. a scaling behaviour described by a power law. Indeed, there is a number of experimental hints for a self-similar structure, apart from theoretical considerations. As an example, Figure 2.8 shows the unintegrated u-quark density for fixed momentum transfer Q^2 and fixed Bjorken x, respectively. For $x \lesssim 0.01$ (below the valence quark region) the unintegrated density function in log-log scale is linear. A linear behaviour is also exhibited by the unintegrated density as a function of Q^2 for fixed x. Refering to eq. (2.13), this suggests that x and Q^2 could be treated as appropriate magnification (scaling) factors. This is supporting the idea that the proton structure exhibits self-similar properties and may be described as a fractal object.

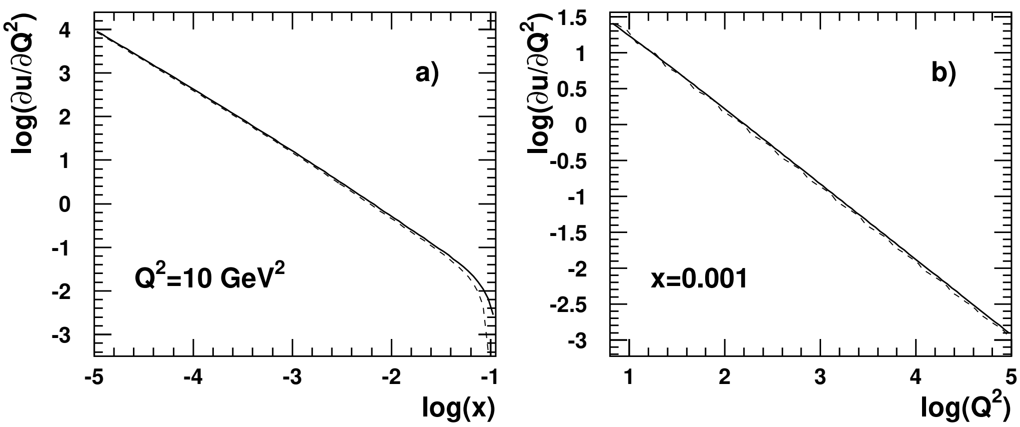

Figure 2.8: Logarithm of the unintegrated u-quark density $\partial u(x, Q^2)/\partial Q^2$ as a function of Bjorken x (a) and Q^2 (b). The full and dashed lines correspond to GRV parametrisations in LO and NLO [37], respectively.

Magnification factors are supposed to fulfil some criteria. They should be positive, non-zero and have no physical dimension. The two latter requirements concern the selection of Q^2 as a magnification factor. The physical dimensionality may be removed by dividing Q^2 by a constant Q_0^2. For the case of $Q^2 = 0$, the non-zero requirement is not fulfilled, however, the access to this region is needed for integration of unintegrated densities. Thus instead of Q^2 a choice of $1 + Q^2/Q_0^2$ as a magnification factor is appropriate. According to the freedom in the magnification factor selection, mentioned above, other equivalent choices are also possible, e.g. $Q_0^2/(Q_0^2 + Q^2)$, $(Q_0^2 + Q^2)/1\text{GeV}^2$ or similar combinations. It is also more appropriate to use $1/x$ as a magnification factor rather than x itself: when the structure is probed deeper, x goes to zero while a magnification factor is expected to rise.

The concept of self-similarity, when applied to proton confinement structure, leads to a simple parametrisation of quark densities within the proton in a straightforward way based on eq. (2.14). Using magnification factors $1/x$ and $1 + Q^2/Q_0^2$, an unintegrated quark density may be written in the following general form

$$\begin{aligned} \log f_i(x, Q^2) &= d_1 \cdot \log\frac{1}{x} \cdot \log(1 + \frac{Q^2}{Q_0^2}) + d_2 \cdot \log\frac{1}{x} \\ &\quad + d_3 \cdot \log(1 + \frac{Q^2}{Q_0^2}) + d_0^i \end{aligned} \tag{2.15}$$

where i denotes a quark flavour. Conventional, integrated quark densities $q_i(x, Q^2)$ are defined as a sum over all contributions with quark virtualities smaller than that of the photon probe, Q^2. Thus $f_i(x, Q^2)$ has to be integrated over Q^2,

$$q_i(x, Q^2) = \int_0^{Q^2} f_i(x, q^2)\; dq^2. \tag{2.16}$$

	d_0	d_1	d_2	d_3	Q_0^2[GeV^2]	χ^2	χ^2/ndf
all fit	0.339	0.073	1.013	-1.287	0.062	136.6	0.82
	±0.145	±0.001	±0.01	±0.01	±0.01		
d_2 fixed	0.523	0.074	*1*	-1.282	0.051	138.4	0.82
	±0.014	±0.001	*const.*	±0.01	±0.002		

Table 2.1: Results of the fit. The first row corresponds to a fit to all parameters, in the second row parameter d_2 was fixed to 1. The number of F_2 data points is 172, total errors were used for the χ^2 calculation.

Solving eq. (2.16), the following analytical parametrisation of a quark density is obtained

$$q_i(x, Q^2) = \frac{\mathbf{e}^{d_0^i}\, Q_0^2\, x^{-d_2}}{1 + d_3 - d_1 \log x} \times \left(x^{-d_1 \log(1+\frac{Q^2}{Q_0^2})} (1 + \frac{Q^2}{Q_0^2})^{d_3+1} - 1 \right). \tag{2.17}$$

Notice that in this parametrisation only the normalisation parameter d_0^i depends on the quark flavour while the other parameters are flavour independent. This assumption means that all quarks exhibit a fractal structure, the dimensions d_i and the magnification factors are common for all of them and they differ in normalisation only.

The proton structure function F_2 is related directly to the quark densities $F_2 = x \sum_i e_i^2 (q_i + \bar{q}_i)$. Thus the assumption about the flavour symmetry of eq. (2.17) allows to express F_2 directly in the form given on the r.h.s. of eq. (2.17) with x^{-d_2} replaced by x^{-d_2+1} and with a common normalisation factor $\mathbf{e}^{d_0}$:

$$F_2(x, Q^2) = \frac{\mathbf{e}^{d_0}\, Q_0^2\, x^{-d_2+1}}{1 + d_3 - d_1 \log x} \times \left(x^{-d_1 \log(1+\frac{Q^2}{Q_0^2})} (1 + \frac{Q^2}{Q_0^2})^{d_3+1} - 1 \right). \tag{2.18}$$

Fit to the data

The five parameters d_i and Q_0^2 are determined using recent data from the HERA experiments H1 [12] and ZEUS [38] in the range $1.5 \le Q^2 \le 120$ GeV^2 (H1) and $0.045 \le Q^2 \le 0.65$ GeV^2 (ZEUS). Additionally a cut $x < 0.01$ is applied to exclude the valence quark region. The fit parameters are given in Table 2.1 and the corresponding description of the $F_2(x, Q^2)$ data is shown in Figures 2.9 and 2.10. The χ^2 was calculated with total errors, adding the statistical and systematical errors in quadrature. When the relative normalisation of the H1 and ZEUS data, which cover different Q^2 regions, was fitted no change beyond 1% was imposed by the fits. Thus the normalisations of the data sets were left untouched.

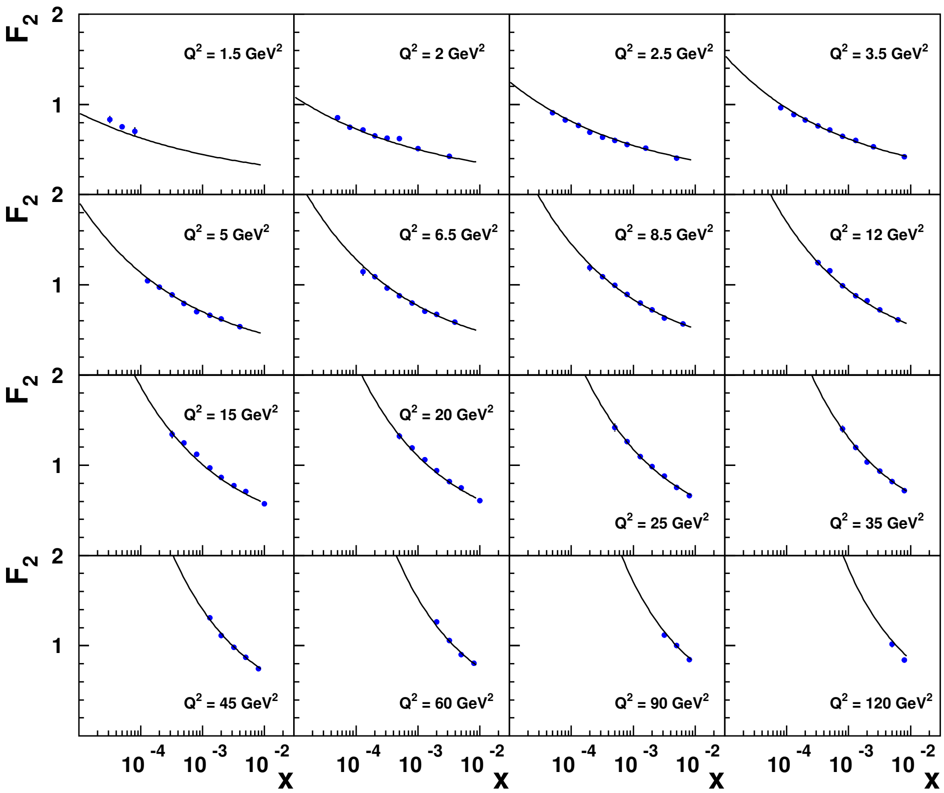

Figure 2.9: Measurement of the structure function $F_2(x, Q^2)$ as a function of x in bins of Q^2 by the H1 experiment [12]. The curve represents the fit to 4 parameters, which is indistinguishable from the 5 parameter fit in this kinematic region.

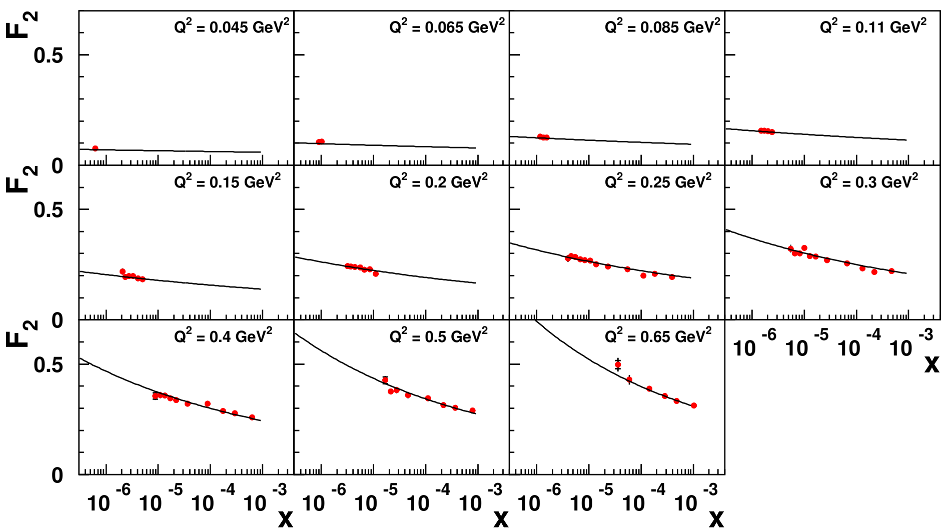

Figure 2.10: Measurement of the structure function $F_2(x, Q^2)$ as a function of x in bins of Q^2 by the ZEUS experiment [38]. The curve represents the same fit to 4 parameters as in Figure 2.9. It is indistinguishable from the 5 parameter fit in this kinematic region too.

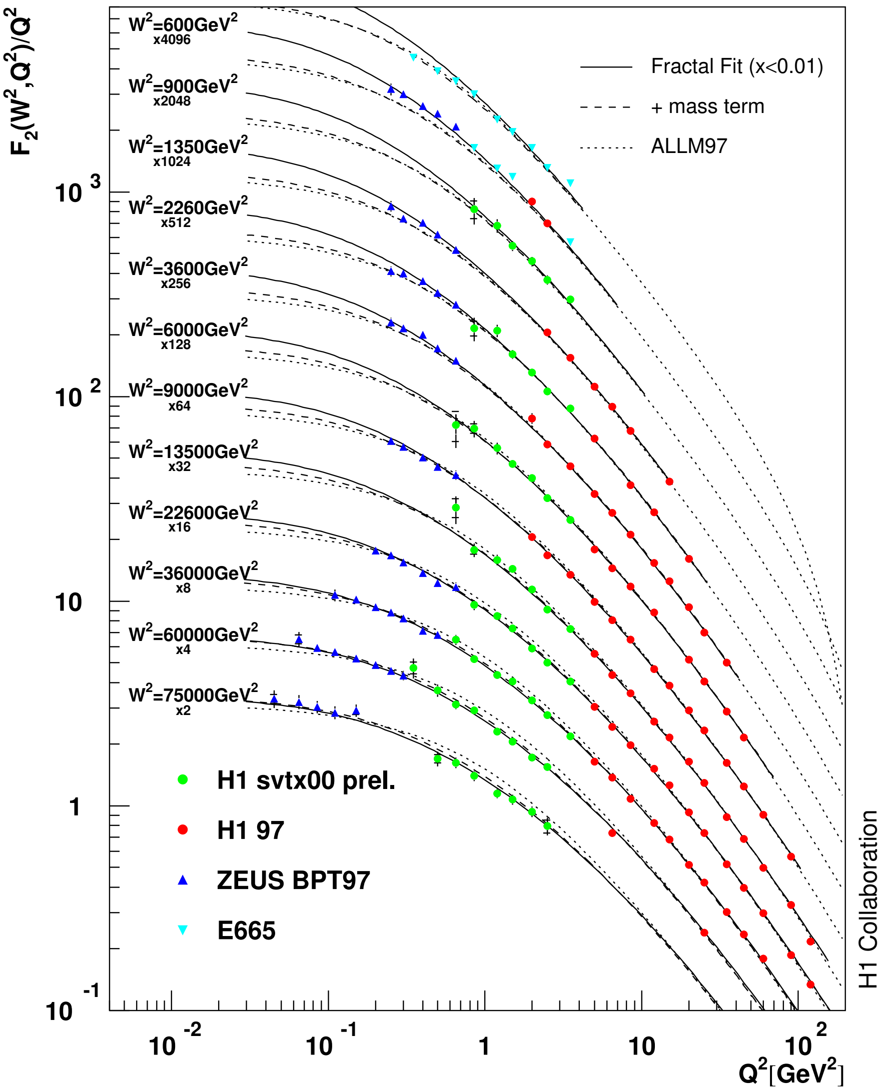

Figure 2.11: Virtual photon-proton cross-section $\sigma_{\gamma^\star p} \propto F_2(W^2, Q^2)/Q^2$ as a function of Q^2 in W^2 bins. H1 (points) and ZEUS (triangles) measurements are shown along with the fit to four parameters (full line), the fit with the mass term included (dashed line) and with the ALLM97 parametrization (dotted line). The fractal fit to all five parameters is indistinguishable from the four parameter fit in the region of measured data.

2.3.3 Extension to the photoproduction limit

The ratio $F_2(W^2, Q^2)/Q^2$ is proportional to the virtual photon-proton cross-section $\sigma_{\gamma^\star p}(W^2, Q^2)$. In the limit $Q^2 \to 0$ and fixed W^2 the parametrization (2.18) behaves like Q^2 only for $d_2 = 1$. This may be easily shown when the unintegrated structure function $f(x, q^2)$ is introduced

$$F_2(x, Q^2) = \int_0^{Q^2} f(x, q^2)\ dq^2 \tag{2.19}$$

the parametrisation of which is identical to (2.15), with d_2 replaced by $d_2 - 1$ and d_0^i replaced by d_0. If $F_2(x, Q^2)$ behaves like Q^2 for $Q^2 \to 0$ then $f(x, q^2)$ has to behave like a constant for any $x = Q^2/(W^2 - M_p^2) \to 0$. That is possible only if the divergent term, involving d_2, is zero, i.e. for $d_2 = 1$. In this case, since other logarithmic terms go to zero, the ratio $F_2(W^2, Q^2)/Q^2$ for $Q^2 \to 0$ approaches the value $\mathbf{e}^{d_0}$.

Indeed, in the fit with d_2 as a free parameter a value very close to 1 is obtained. Fixing $d_2 = 1$ thus reduces the number of parameters to four and the corresponding fit gives a very similar value of $\chi^2/\mathrm{ndf} \doteq 0.82$ as the fit to all five parameters.

Another way how to reach the photoproduction limit is to introduce a *mass term* in the calculation of Bjorken x, which is usually neglected at high W^2:

$$x \to x + \frac{m^2}{W^2}, \tag{2.20}$$

where m is an effective mass of a proton constituent and it is fitted as another parameter in the fit to the data. In such a case, the ratio $F_2(W^2, Q^2)/Q^2$ always converges when $Q^2 \to 0$ and the photon-proton cross-section $\sigma_{\gamma p}$ has a power law behaviour of the form $(W^2)^{d_2-1}$. The result of the fit with the mass term is shown in Figure 2.11 as a dashed line. The same data as in the previous fit were used, complemented by photoproduction data to fix the fit in $Q \to 0$ limit. Hence, neither E665 nor preliminary H1 data, displayed in the Figure 2.11, were used. The behaviour of the fit at low W^2 is similar to ALLM97 while at high W^2 it approaches the fractal fit without the mass term.

Since this way of reaching the photoproduction limit yields a reasonable behaviour of the photoproduction cross section and since masses of particles cannot be neglected in the very low x region, hereafter the fit with the mass term is preferred.

2.3.4 Negativity of the d_3 dimension

One of surprising facts in the fractal model fit to the data is a negativity of the dimension d_3, related to the scaling in the variable $(1+Q^2/Q_0^2)$. This fact was merely mentioned in the original paper [3] since it comes as a result of the fit. The situation gets more confusing if one takes into account the dependence of the dimension on the variable x via the dimensional correlation d_1. At some value of rather low x the dimension is approaching zero and for even lower x it becomes positive. Beyond a discussion whether negative dimensions are physical or not, the author would like to mention that prior to a dimensional analysis it is necessary to specify precisely what, how and in which kinematic range is measured. An example can be again the Koch curve. Its fractal dimension can be calculated from counting the self-similar pieces as well as from measuring its length, see Section 2.1. In the latter case the length scales as a power law but with the dimension related to the length resolution Δl being $1 - d_f$, rather than d_f itself. This is due to the dimensionality of the length measure and due to the inverse relation between the resolution and the magnification factor. A similar situation would happen if the dimension would be measured via e.g. measuring the area covered by the Koch curve. Here the exponent of the length resolution Δl would be $2 - d_f$.

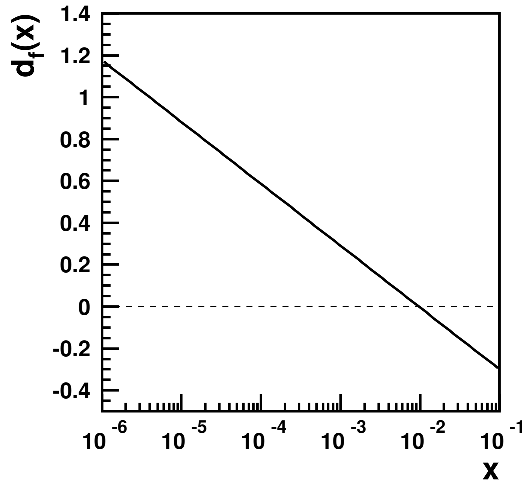

Figure 2.12: Fractal dimension d_f corresponding to dimension d_3 and dimensional correlation d_1 as a function of x.

In the fractal model an unintegrated density $f_i(x, Q^2)$ is parameterized. Its physical dimension is GeV^{-2} what after integration over Q^2 gives the conventional parton density with no physical dimensionality. This is an analogy to a measurement of the fractal dimension by an area since GeV^{-1} is a length measure. Refering to eq. (2.3) for $d_t = 2$ corresponding to an area measure, one thus obtains the following relation interconnecting d_3 to the fractal dimension in length

$$2 - d_f = -2\, d_3, \tag{2.21}$$

where the factor of -2 on r.h.s. comes from the inverse conversion of the magnification factor to the resolution and due to scaling of $(1 + Q^2/Q_0^2)$ as inverse length squared. The latter fact is slightly hidden in the removal of the physical dimensionality by Q_0^2, however, for the discussion on the negativity of the d_3 dimension it is not even necessary.

Furthermore, as was already mentioned, the dimension related to $(1 + Q^2/Q_0^2)$ is x-dependent via the dimensional correlation d_1. Hence, the fractal dimension corresponding to dimension d_3 and correlation d_1 can be expressed as

$$d_f = 2\left(1 + d_3 + d_1 \cdot \log\frac{1}{x}\right). \tag{2.22}$$

It is visualized in Figure 2.12 as a function of x using parameters obtained from the fit to the data. At approximately $x = 0.01$ and below the fractal dimension is positive as expected. On the contrary, it becomes negative for $x \gtrsim 0.01$. This high x region is out of applicability of the fractal model in the presented form since there is a sizeable contribution of valence quarks. These play the role of a seed for the low x structure, in the fractal picture. Hence extrapolating the fractal dimension into that region is meaningless.

Intuitive explanation of the dimensional behaviour seen in Figure 2.12 is that the deeper is the proton structure probed in terms of contributing momenta the more degrees of freedom (dimensions) has its spacial evolution.

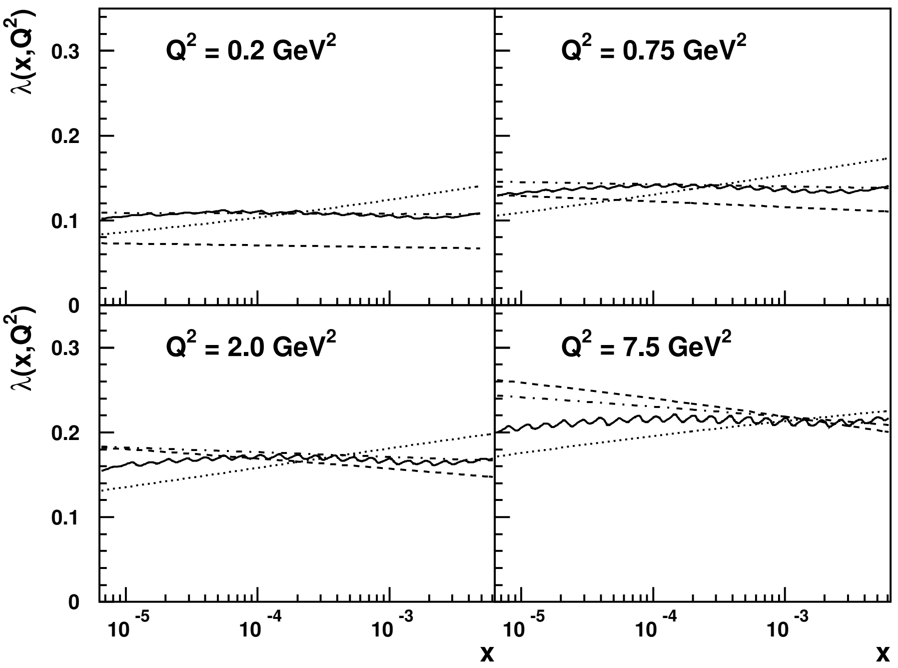

Figure 2.13: Exponent $\lambda(x, Q^2)$, characterizing the speed of the rise of F_2 towards low x, as a function of x in bins of Q^2. Fractal model with (dot-dashed line) and without (dashed line) mass term is compared to the original (dotted line) and DGLAP improved (full line) version of the GBW saturation model. The full line is rugged due to the evaluation of the model structure function $F_2(x, Q^2)$ on a grid.

2.3.5 Saturation

Although there is no explicit saturation mechanism built in the naive fractal model, it is not without interest to compare the low x behaviour of the model with that of models with saturation built in. In this section, the GBW saturation model (see Section 1.8) is employed and a comparison is done in terms of the structure function derivative

$$\lambda(x, Q^2) = -\left(\frac{\partial \ln F_2(x, Q^2)}{\partial \ln x}\right)_{Q^2}, \tag{2.23}$$

which corresponds to the rate of the rise of F_2 towards low x, as was discussed in Section 1.7. Figure 2.13 displays the x-dependence of $\lambda(x, Q^2)$ in bins of Q^2. The fractal model is represented by dot-dashed lines (mass term included) and by dashed lines (without mass term). The dotted and full lines correspond to the GBW saturation model in its original form and in the DGLAP improved one, respectively. One can notice that the original saturation model draws the $\lambda(x)$ dependence down towards low x. This is due to the saturation effect which asymptotically slows down the rise of F_2 from the power-law behaviour to logarithmic one. On the other hand, the DGLAP improved saturation model has a different behaviour. At larger x it is consistent with the fractal model and slightly rising towards low x while at some point the rise is tamed and eventually $\lambda(x)$ decreases as in the case of the original saturation model.

Note that the DGLAP improved saturation model was originally aimed to improve the description of medium and large Q^2 data while preserving success of the original version to describe low Q^2 data and diffraction.

Formally, saturation effects in the fractal evolution can be added for example as follows

$$\frac{\partial f(z)}{\partial \log(z)} = d\ f(z) - d_1 f(z) - K f(z)^2, \tag{2.24}$$

where z is a magnification factor (eventually $1/z$ can be treated as a resolution). The first term on the r.h.s. corresponds to a normal fractal evolution, hence d is the fractal dimension. The second term slows down the evolution by a factor proportional to $f(z)$. The effect of such a term is only in a change of the original dimension $d \mapsto d - d_1$. The last term on the r.h.s. of eq. (2.24) is non-linear and it suppresses the evolution by a factor proportional to $f(z)^2$. Hence, absorbing the second term into the first one, for simplicity, a solution reads as

$$f(z) = \frac{\mathbf{e}^{Cd}\ d\ z^d}{1 + \mathbf{e}^{Cd}\ K\ z^d}, \tag{2.25}$$

where C is an integration constant. From eq. (2.25) it is seen that as long as $\mathbf{e}^{Cd}\ K\ z^d \ll 1$, the density $f(z)$ evolves like a normal fractal density with dimension d. On the other hand, for $\mathbf{e}^{Cd}\ K\ z^d \gg 1$, the density is constant, i.e. $f(z) \to d/K$. The parameter K may be fitted to the data. It is found to be negligible and consistent with zero.

2.3.6 Pion structure function

The previous sections were focused on the proton structure function $F_2(x, Q^2)$ since there are the most precise data on F_2. Recently the ZEUS collaboration published [39] a new determination of the pion structure function $F_2^\pi(x, Q^2)$, in the region of low Q^2, low x. Although the data are not as precise as are those of the proton, they are valuable for understanding the pion structure in the low x region and for a comparison with the proton case.

Phenomenologically, there is no fundamental difference in the fractal picture between the proton structure function F_2 and the pion structure function F_2^π. Hence, the same parametrisation form as in eq. (2.18) can be used to fit the pion data on F_2. Unfortunately the number of low x points ($x \lesssim 0.01$) which can be used for such a fit is too low, see Figure 2.14.

An interesting, albeit naive comparison with the proton structure function $F_2(x, Q^2)$ in the fractal picture can be done in the following way: assuming that fractal dimensions are *universal* for both the proton and the pion as well as the scale Q_0^2, the only difference comes from the normalisation. A fractal structure develops from a seed, hence, it scales with the seed size. The size of the seed can be proportional e.g. to the number of valence quark pairs, i.e. to the number of confining flux tubes, or the number of valence quarks themselves. Although it is not clear how the seed scales, neither the available data gives hint, for a demonstration the scaling according to the number of confining flux tubes will be considered hereafter.

There are three combinations of valence quarks in the proton case and one in the pion case, thus from seed scaling one would expect a relation of this sort

$$F_2^\pi(x, Q^2) \approx \frac{1}{3} F_2^p(x, Q^2). \tag{2.26}$$

This is indeed close to an observation of ZEUS in [39], see Figure 18, where instead of factor 1/3 the data suggest ≈ 0.361. Furthermore, one should have in mind that e.g. $x_p = 10^{-3}$ in the

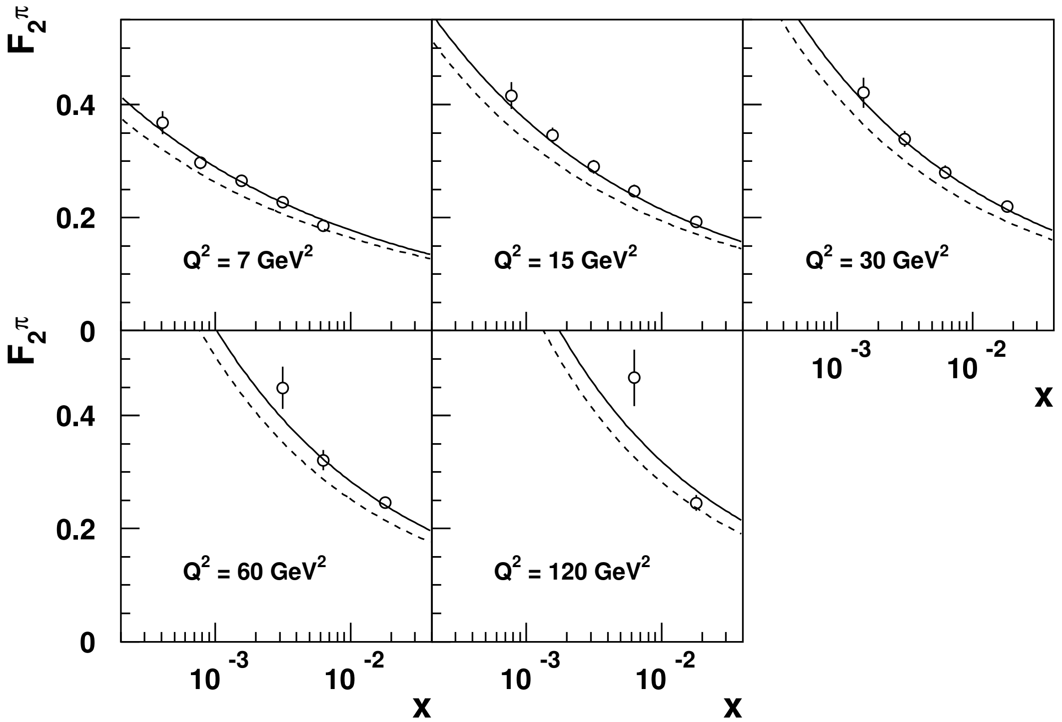

Figure 2.14: The pion structure function $F_2^\pi(x, Q^2)$ as determined by ZEUS [39] in the range of low x. The fractal model naive prediction (full line) is compared to the same prediction without x-dependence correction (dashed line). The prediction of the fractal model uses a fit to the proton structure function F_2.

proton is not the same as $x_\pi = 10^{-3}$ in the pion due to a different length of the fractal evolution, starting from high-x, from the valence quark region. Due to the number of the valence quarks it is intuitive to expect, in the QPM picture, that e.g. $x_p = 1/3$ corresponds to $x_\pi = 1/2$, hence, approximately $x_p = \frac{2}{3}x_\pi$. Absorbing this relation to eq. (2.26) the following naive expectation based on the fractal picture is obtained

$$F_2^\pi(x, Q^2) = \frac{1}{3}F_2^p(\frac{2}{3}x, Q^2). \tag{2.27}$$

Figure 2.14 shows the measured data in the low x region along with estimates based on eq. (2.26) and eq. (2.27). Qualitatively, the fractal model prediction gives $\chi^2/ndf = 0.81$ on these data, what is about the same value as for the case of the fractal fit to the proton structure function F_2^p. Typical precision of the data is about 4-5 %, not including the normalisation uncertainty.

Although formula (2.27) seems to describe the data indeed very well[7], it should be emphasized, however, that ZEUS data on F_2^π have a large uncertainty on their normalisation due to the model-dependence of the pion flux, see Section 10.3 in reference [39]. The above presented measurement corresponds to a particular selection of the pion flux, obtained from the hadronic reactions. Another possibility is to employ the additive quark model, which results into F_2^π approximately two times higher. The latter result is consistent with the assumption in the fractal picture that the seed scaling is proportional to the number of quarks.

Although the existing data on F_2^π do not constrain the normalisation of the structure function and hence scaling of the seed, they suggest a universality of fractal dimensions in the proton and pion.

[7]Compared to the data description by various models presented in [39], Figure 18 and 19.

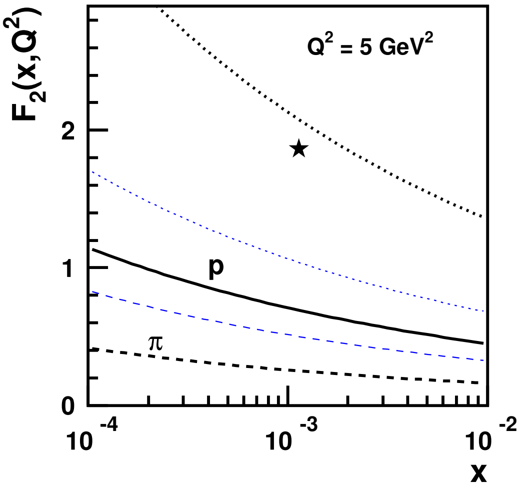

Figure 2.15: The structure function F_2 as a function of Bjorken x for $Q^2 = 5\,\mathrm{GeV}^2$ for proton (full line), pion (dashed line) and pentaquark (dotted line). Thin lines correspond to a different scaling scheme, see text.

A verification of the assumed universality of the fractal dimensions and of the seed scaling would be possible by studying structure functions of another particle, with different numbers of valence quarks than mesons and baryons. In the context of the recently opened topic of *pentaquarks* [40], these are naturally a good candidate. Following the above naive mathematics with five valence quarks instead of three, an expected structure function $F_2^\star(x, Q^2)$ for a pentaquark at low x would be

$$F_2^\star(x, Q^2) = \frac{10}{3} F_2^p(\frac{5}{3}x, Q^2). \tag{2.28}$$

Figure 2.15 shows $F_2^\star$ compared to F_2^p and F_2^π in a bin of $Q^2 = 5$ GeV^2. The speculative $F_2^\star$ is significantly larger than the other structure functions, hence, one would expect that effects of shadowing or saturation enter much sooner than in the case of the proton and pion structure functions. On the contrary, if a different scaling scheme is chosen, e.g. proportional to the number of the valence quarks (thin lines in Figure 2.15), the structure function for a pentaquark may be much closer to that of the proton.

Chapter 3

The H1 detector at HERA

3.1 HERA accelerator

HERA (Hadron Electron Ring Accelerator) at the DESY laboratory in Hamburg is the first facility to provide colliding beams of electrons and protons. It is designed to accelerate 210 bunches of electrons (or positrons) and 210 bunches of protons to energy of 27.55 GeV and 920 GeV, respectively. Bunches separated by 96 ns are accelerated in two independent storage rings housed in a tunnel of circumference 6.3 km. Not all of the bunches collide, some of them, called pilot bunches, pass through the detectors without having collided, and they are used for background and timing studies.

The center of mass energy at HERA is 314 GeV which is equivalent to a 50 TeV incident electron beam on a fixed target. This provides an extension of two orders of magnitude in the accessible kinematic range in x and Q^2 compared to fixed target experiments. The electron and proton bunches are arranged to intersect at two interaction points, around which the H1 (North Hall)

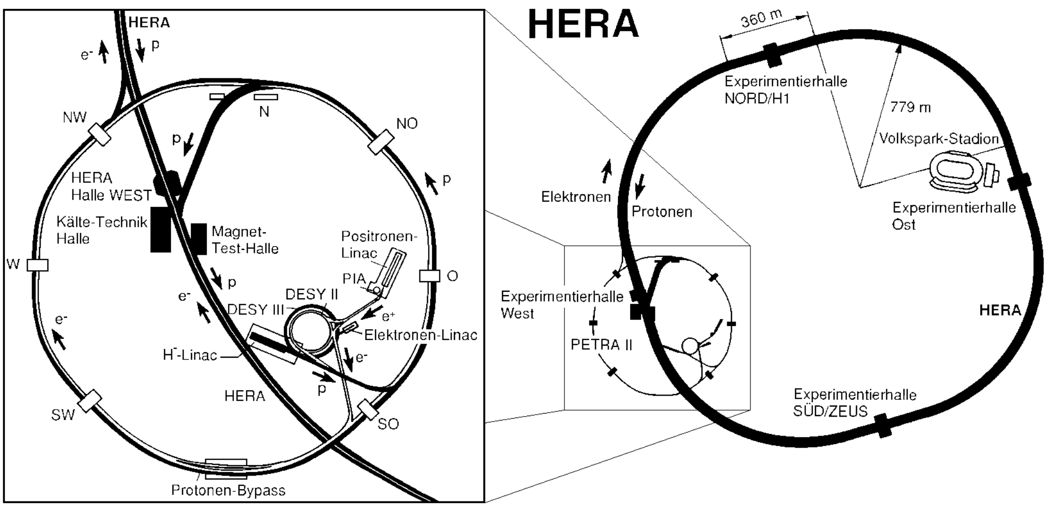

Figure 3.1: The HERA accelerator at DESY and injection system

and ZEUS (South Hall) experiments are located. Furthermore there are two fixed target experiments, HERMES (East Hall) and HERA-B (West Hall), where only one of the beams is used. A schematic layout of the HERA facilities at DESY is shown in Figure 3.1.

The positrons from a 500 MeV linear accelerator are injected into a storage ring where they are accumulated and then injected into the synchrotron DESY II which increases their energy up to 7 GeV. In the next step they are transferred into the PETRA ring where the energy is raised up to 14 GeV after accumulating up to 70 bunches. Bunches are then injected into HERA. This is repeated until HERA is filled with up to 210 bunches of positrons.

A whole new chain of pre-accelerators was built in order to inject protons into HERA. A linear accelerator delivers a 50 MeV negatively charged hydrogen ion beam which is stripped upon entering into the DESY III synchrotron. Inside DESY III the protons are captured into 11 radio frequency buckets with the final bunch spacing and the final total number of particles per bunch, unless losses happen during transfers and ramping. The protons are then accelerated up to 7.5 GeV and transferred to PETRA, which can accumulate up to 70 bunches and accelerate them up to 40 GeV. Finally they are transferred into the HERA proton ring.

3.2 Detector overview

The H1 detector [41] is a multipurpose device designed to study various aspects of ep scattering. In order to employ fully the physics potential of HERA, the detector has to perform a number of vital tasks, which are:

- **Electron detection:** the reliable identification and energy measurement of scattered electrons is crucial to study NC DIS events. A particular challenge is region of high inelasticity y where the signal is contaminated by photoproduction background.
- **Hadron detection:** calorimetry with fine granularity and good resolution is needed in order to measure the hadronic final state in various processes covering the full phase space.
- **Charged particle tracking:** charged particle momentum measurement and identification are required for the investigation of many processes at HERA and for the background suppression using tracking detectors covering almost the whole 4π solid angle. A magnetic field bends the tracks and allows the momentum to be determined, while energy loss measurements enable particle identification in a restricted momentum range.
- **Luminosity measurement:** accurate determination of the luminosity delivered to the experiment is vital for calculation of cross sections. At HERA the Bethe-Heitler reaction $ep \to ep\gamma$ is measured which allows to monitor the luminosity at the percent level.
- **Triggering and readout:** the high bunch crossing rate at HERA and the very high backgrounds from beam-gas and beam-wall interactions require that the detector must be able to distinguish physics processes from the background, digitize and read out a large number of detector channels (> 250000) while minimising dead time. A fast, pipelined, multi-level trigger system, in combination with high-speed digitization and readout, is therefore employed.
- **Muon identification:** heavy flavour, rare Standard Model and exotic physics processes are possibly detected through the production of muons in the final state.

The H1 detector is approximately cylindrically symmetric around the beam axis. The *coordinate system* of H1 is right handed and defined with the z axis parallel to the proton direction, the y axis vertical and the x axis perpendicular to the others, see Figure 3.2. The origin is defined as the nominal interaction point. The side of the detector situated on the positive side of z axis (relatively to the interaction region) is referred to as the "forward" part. The negative side, corresponding to the outgoing electron direction, is referred to as the "backward" region. Apart from the H1 coordinate system two more coordinate systems are introduced. In the *vertex coordinate system* the origin of the H1 coordinate system is moved in the point where the beam is crossing $z = 0$ plane. Furthermore, if the axes are ortonormally rotated in the way that the z-axis is parallel to the beam, the system is called the *beam coordinate system*. Introducing the latter system is important due to the fact that it is the natural coordinate system for the beam interactions. Hence, in order to ensure e.g. the consistency of fiducial cuts in data and simulations, these should be done in the beam coordinate system.

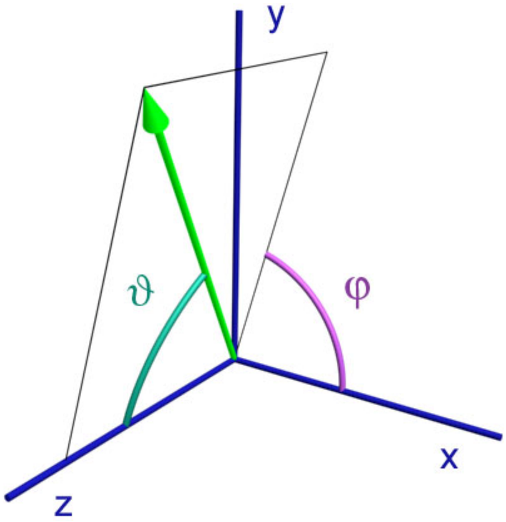

Figure 3.2: A 3D illustration of the H1 coordinate system.

An isometric projection of the H1 detector is shown in Figure 3.3. Starting the description from the interaction point, silicon trackers surround the beam pipe $\boxed{1}$ in central and backward region (not shown). The central $\boxed{2}$ and forward $\boxed{3}$ trackers enclose the silicon trackers and the beam pipe. The Liquid Argon (LAr) electromagnetic $\boxed{4}$ and hadronic $\boxed{5}$ calorimeters mounted in the Liquid Argon cryostat, surround the central trackers. The SpaCal electromagnetic and hadronic calorimeters $\boxed{12}$ are situated in the backward region. The Backward Drift Chamber (BDC) is mounted on the SpaCal calorimeter at the front side. A superconducting coil $\boxed{6}$ of radius 3 m is placed outside the LAr calorimeter and provides uniform magnetic field of 1.2 T. This field is compensated by another superconducting coil $\boxed{7}$ in order not to influence the HERA accelerator. The large iron return yoke $\boxed{10}$ returns the magnetic flux and completes the magnetic circuit of the solenoid. It also serves as a tail catcher to detect hadronic showers not contained by the LAr calorimeter. The muon chambers $\boxed{9}$ are used for muon identification. The measurement of muon tracks in the forward region is provided by a toroid $\boxed{11}$ equipped with drift chambers. The plug calorimeter $\boxed{13}$ surrounds the beam pipe in the forward region. The whole detector is covered by concrete shielding in order to prevent radiation in the experimental hall. The electron tagger at position $z = -33\,\mathrm{m}$ upstream the interaction point (in HERA tunnel) detects electrons with a very small scattering angle. In conjunction with the photon detector at $z = -102.9\,\mathrm{m}$ it monitors the luminosity by the bremsstrahlung process $ep \rightarrow ep\gamma$. This reaction has a well known cross section.

The above components will be described in more detail in the following sections. A special focus is paid in Section 3.3 and 3.4 to the SpaCal calorimeter and the BST silicon tracker, respectively, because of their importance for the presented measurement.

3.2.1 Track detectors

The H1 tracking system is divided into two main components; the central tracker (CTD), covering the polar angle range $15° < \theta < 165°$, and the forward tracker (FTD), covering the region

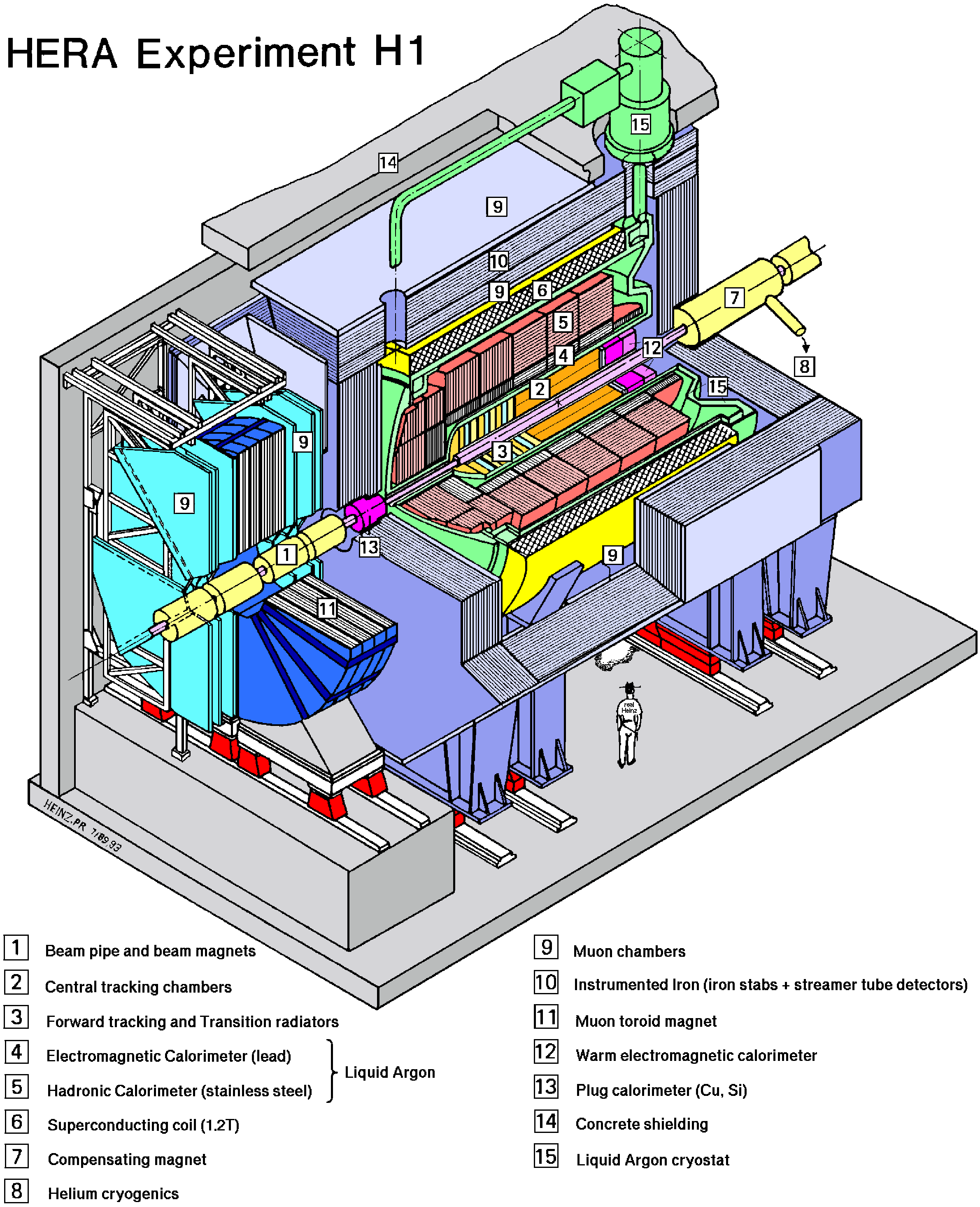

Figure 3.3: Isometric view of the H1 detector at HERA, DESY Hamburg, status of 1992.

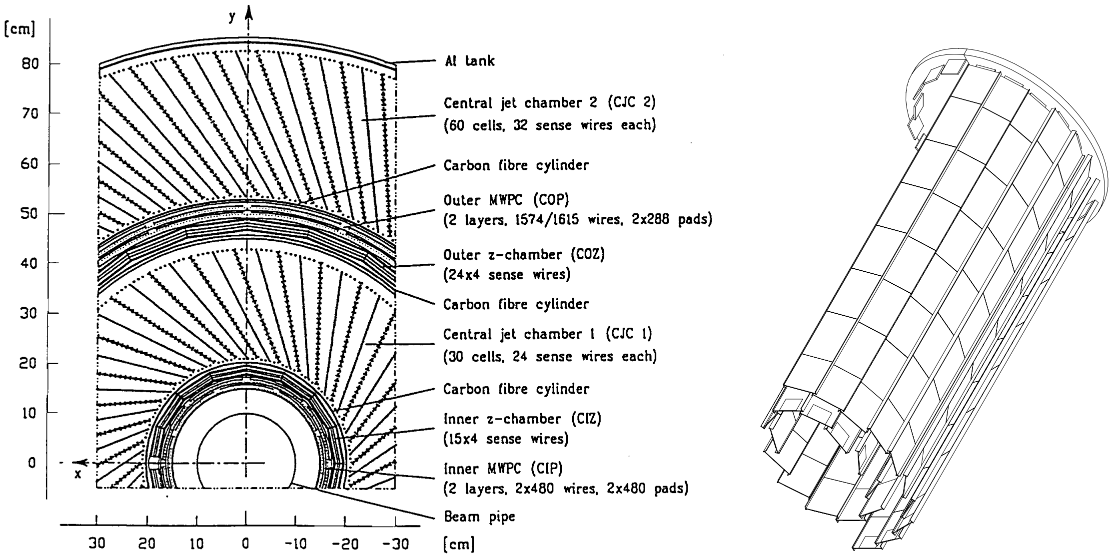

Figure 3.4: Radial view of the central tracker (left) and isometric view of the central silicon tracker CST (right).

$7^\circ < \theta < 25^\circ$. In addition, the backward region is covered by a backward drift chamber (BDC) in front of the SpaCal calorimeter and covers the angular range $151^\circ < \theta < 177.5^\circ$. The central and backward silicon trackers (CST and BST) provide precision measurement of tracks close to the interaction point.

Both the central and forward trackers consist of drift and multi-wire proportional chambers (MWPC). The drift chambers are used for precise trajectory measurements of charged particles; enabling a determination of the particle momentum. Hits can be located within $\sim 150\,\mu$m in the drift direction. The coordinate parallel to the wire can be determined by charge division of the pulses recorded at each end of the wire, to a precision of $\sim 1\%$ of the wire length (i.e. $\sim 2\,$cm in the case of 2 m long CTD wire). The MWPCs have an intrinsic spatial resolution limited by the wire spacing and is worse than that of the drift chambers. However, they have rapid response time to passing of charged particles and therefore are useful for triggering purposes.

The Central Tracker

The central tracker consists of a number of interleaved drift chambers, MWPCs and silicon trackers (see Figure 3.4). Reconstruction of trajectories in the central region is based mainly on two concentric drift chambers, CJC1 and CJC2, while the z vertex position is mainly reconstructed by CIZ and COZ chambers. The central track chambers are complemented by the central silicon tracker CST and the backward silicon tracker BST which is described in detail in Section 3.4 and will not be mentioned here.

The CJCs have drift cells defined by 2200 mm long wires strung parallel to the beam axis and inclined by about 30° with respect to the radial direction, so that the drift direction is approximately perpendicular to high momentum tracks. The chamber has an inner radius of 200 mm, an outer radius of 795 mm and a length of 2640 mm . The inner chamber, CJC1, has 30 cells with 24 wires each, and the outer chamber, CJC2, has 60 cells with 32 wires each. A spatial resolution of $170\,\mu$m in the r-ϕ plane and 2.2 cm in z was measured which compares well with the design goals. The particle momentum is reconstructed from the curvature of the track caused by the magnetic field. The CJC allows the measurement of the particle momentum with a precision $\sigma_p/p^2 < 0.01\,\mathrm{GeV}^{-1}$. Particle identification is assisted by measurement of the specific energy loss, dE/dx, along the track, with a typical resolution of 10%. The event interaction vertex determination relies essentially on CJC reconstructed tracks.

Two thin drift chambers with wires perpendicular to the beam axis enable a better measurement of the track position in the z-coordinate than is possible from charge division of the CJC signals. The inner z-chamber (CIZ) is located inside CJC1, and the outer chamber (COZ) lies between CJC1 and CJC2. They provide track elements with typically $200\,\mu$m resolution in z and about 2% in ϕ.

Linking these track elements to those obtained from the jet chambers gives the design resolution for the momentum of charged tracks $\sigma_p/p^2 \approx 3 \times 10^{-3}\,\mathrm{GeV}^{-1}$ and for the polar angle $\sigma(\theta) \approx 1\,\mathrm{mrad}$.

Two cylindrical MWPC chambers are also part of the central tracker. The inner multiwire proportional chamber (CIP) is closest to the interaction region and is composed of 60 sectors in z-direction and 8 sectors in ϕ. The outer multiwire proportional chamber (COP) lies between COZ and CJC2. It is composed of 18 sectors in the z-direction and 16 sectors in ϕ. The CIP and COP both consist of double cell layer, with wires parallel to the z-axis. The fast timing signals, with a time resolution better than the separation between two successive HERA bunch crossings (75 ns for CIP and 60 ns for COP), are used to define vertex-pointing tracks for the purpose of triggering.

The Forward Tracker

The Forward Tracking Detector (FTD) consists of three identical modules, known as supermodules, which contain planar drift chambers, MWPCs and a layer of transition radiator material and radial drift chambers.

Each planar module contains three planar wire drift chambers, rotated by 60° to each other in azimuth. These chambers consist of four wire planes in the z direction with 32 wires per plane each. This design enables to provide a space point reconstruction in the $x - y$ plane with a spatial resolution of $\sigma_{xy} \simeq 160\,\mu$m.

The radial drift chambers consist of planes of sense wires strung out from the beam pipe, such that the maximum drift length for each wire increases with distance from the beam-axis. The radial chambers thus provide an accurate measurement of the azimuthal angle, together with a moderate measurement of the radial coordinate using charge division. Each radial chamber has 48 cells in ϕ with 12 sense wires in z-direction.

One forward MWPC is are located in each supermodule, consisting of a double layer of wires strung along the vertical axis (i.e. the y-axis). The MWPCs in the first submodule are used in conjunction with the CIP and COP to provide a trigger on tracks originating from the vertex. All three submodules are used to produce a trigger on tracks in the forward region.

The Backward Drift Chamber

The Backward Drift Chamber (BDC) is mounted on the front surface of the SpaCal calorimeter. It is designed to provide a better measurement of the scattered electron angle than the SpaCal calorimeter.

The BDC consists of four double layers of drift chamber planes in eight octants with sense wires strung in the radial direction. Each double layer is staggered in order to resolve the ambiguity of the track position in the drift coordinate. The layers are rotated by $11.5°$ with respect to one another in ϕ to enable construction of track segments from the intersection of hits in the layers. The BDC is designed to provide a space point resolution in the radial coordinate of $\sigma(r) = 0.4\,\mathrm{mm}$ and in the ϕ coordinate of $\sigma(r\phi) = 0.8\,\mathrm{mm}$.

3.2.2 Calorimetry in the H1 detector

The H1 tracking system is complemented by the H1 calorimeter system in order to measure the total energy of both charged and neutral particles produced in the interaction. There are four detectors which provide energy measurements: the Liquid Argon, SpaCal, tail catcher and plug calorimeters. The SpaCal calorimeter is described in more detail in Section 3.3 and will not be mentioned here.

The Liquid Argon Calorimeter

The Liquid Argon (LAr) Calorimeter provides the basic measurement of hadronic energy. Above $Q^2 \simeq 100\mathrm{GeV}^2$ the scattered electron in DIS is also detected in this calorimeter.

The LAr calorimeter covers the angular range of $4° < \theta < 154°$ and is mounted in a large argon cryostat. The calorimeter consists of an electromagnetic section with lead absorbers, corresponding to a depth of between 20 and 30 radiation lengths, and a hadronic section with steel absorbers. The total length of the LAr calorimeter is between 4.5 and 8 hadronic interaction lengths. The calorimeter is highly segmented in both sections, with a total of around 45000 cells. The orientation of the absorber plates is such that the angle of incidence of particles is always greater than $45°$.

Test beam studies of LAr calorimeter modules have demonstrated energy resolutions of $\sigma(E)/E \simeq 0.12/\sqrt{E} \oplus 0.01$ with E in GeV for electrons and $\sigma(E)/E \simeq 0.5/\sqrt{E} \oplus 0.02$ for charged particles. The very fine granularity of the LAr allows the longitudinal shower development to be used for efficient e/π separation. The overall electromagnetic energy scale is presently known to 1-3%, and the absolute scale of the hadronic energy measurement is known to 2-4%.

The Tail Catcher

The tail catcher (TC) provides a coarse measurement of the energy of hadronic showers leaking out of the LAr detector. The TC is divided into the central barrel and the forward and backward end-caps. The energy resolution of the TC detector has been measured to be $\sigma(E)/E \simeq 100\%/\sqrt{E}$. The overall energy scale is known to 35%.

beam gas interactions	50	kHz
cosmic μ in barrel	700	Hz
tagged γp	25	Hz
$e\bar{e}$ total	15	Hz
DIS low Q^2	2.2	Hz
DIS high Q^2 (e in LAr)	1.4	min^{-1}
Charged current DIS $p_T > 25$ GeV	30	h^{-1}
W production	0.5	d^{-1}

Table 3.1: The event rates at HERA 1 design luminosity $\mathcal{L} = 1.5 \times 10^{31} cm^2 s^{-1}$ [41].

The Plug Calorimeter

The plug calorimeter (PLUG) covers the extreme forward direction $0.6° < \theta < 3°$. Its primary task is to minimize the loss of transverse momentum due to hadrons emitted close to the beam pipe. The design value of the energy resolution of PLUG is $150\%/\sqrt{E}$.

3.2.3 The H1 trigger

Interactions at the H1 detector are dominated by background events rather than physics events. In order to select interesting physics processes, the H1 detector is equipped with a trigger system. The philosophy of the trigger is to minimize the dead-time of the experiment, which is the time following a trigger in which the signals from the subsystems are being read and therefore the subsystems are insensitive to new events. For the background rate of 10 kHz, the H1 trigger is designed and able to reduce the event rate to $\approx$ 50 Hz with a dead time of about 10%. For detailed information of events rates see Table 3.1. Background events that have to be considered include

- interactions between beam electrons or protons with the residual gas in the beampipe;
- interactions between off momentum beam particles and the walls of the vacuum chamber;
- synchrotron radiation;
- cosmic rays.

The HERA bunch crossing interval of 96ns is short when compared with the response times of many subdetectors. For example in the drift chambers the maximum drift time is of the order of 1 μs (for detailed information see Table 3.2). Consequently the readout is *pipelined* in synchronisation with the HERA clock (HCKL). For at least 24 bunch crossings the information is being stored whilst an initial trigger decision (L1) is determined. The L1 trigger thus turns out to be deadtime free.

The H1 trigger is of a multilevel design. Each successive level processes more precise data and takes longer time to make a better trigger decision of keeping events. The trigger information is centrally controlled by the Central Trigger Logic (CTL) which makes a global decision based on combination of all subsystem trigger information.

width of proton bunch	1.4	ns
distance to next satellite bunch	5	ns
flight time to backward ToF	6	ns
flight time to barrel muon system	20	ns
bunch crossing interval	**96**	**ns**
longest drift time in CJC	1	μs
integration time of LAr preamplifier	1.5	μs
delay of first level trigger	2.5	μs
front end readout time	~ 1	μs

Table 3.2: Time scales at HERA and H1 [41].

Level 1 The level 1 trigger consists of nine different trigger systems, each based on the information given by a subdetector. The outputs of these systems are called *trigger elements*, i.e. {yes/no} decisions encoded in bits. The types of information from which trigger elements are created include:

- **Calorimeter energy:** signals in LAr and Spacal are summed in *towers* and compared to thresholds in order to find jet and electron candidates.
- **Z-vertex:** information from central tracker MWPCs is used to determine the position of the interaction vertex.
- **Time-of-flight:** the ToF systems described in Section 3.2.5 are used to generate triggers for in-time events or veto for background events.
- **Muon tracks:** the central muons system generates triggers for muons in iron return yoke. The forward muon system information is processed by a sophisticated trigger system which extracts a t_0 and pointing track candidates from the drift chamber signals.

Trigger elements are then combined into so called *subtriggers*. Up to 128 subtriggers can be defined in order to select interesting physics events (physics triggers), to monitor detection efficiency (monitor triggers) or to select cosmic ray events for calibration purposes (cosmic triggers). The rate of each subtrigger is computed separately and can be prescaled if needed. The final level decision of L1 is given by the logical OR of all subtriggers and is distributed to the front end electronics of all subsystems to stop the pipeline.

Level 2 The L2 trigger provides a complex decision based on more detailed information. The systems are based on topological array [42] and more sophisticated neural technology [43], both of which are suited to make decisions based on correlations in multi-dimensional space. The decision of the level 2 trigger, which is ready after a period of typically $20\,\mu$s, defines whether a fast rejection will be applied or whether the event is to be treated further.

Level 3 This level was proposed as further intermediate trigger step to suppress event rate but has not been put into operation in the first phase of HERA.

Level 4 The level 4, which is integrated in the central data acquisition system, is based on a farm of approximately 30 fast RISC processor boards. Each processor reconstructs a complete event to which it applies a series of selection criteria depending on those subtriggers that triggered the event. For example, one of the most important rejection algorithms relies on the event (x, y, z) vertex constraint. Events which pass the L4 are written to tape at a typical rate of 10 Hz. The average size of one event is 130 kB. L4 also creates separate

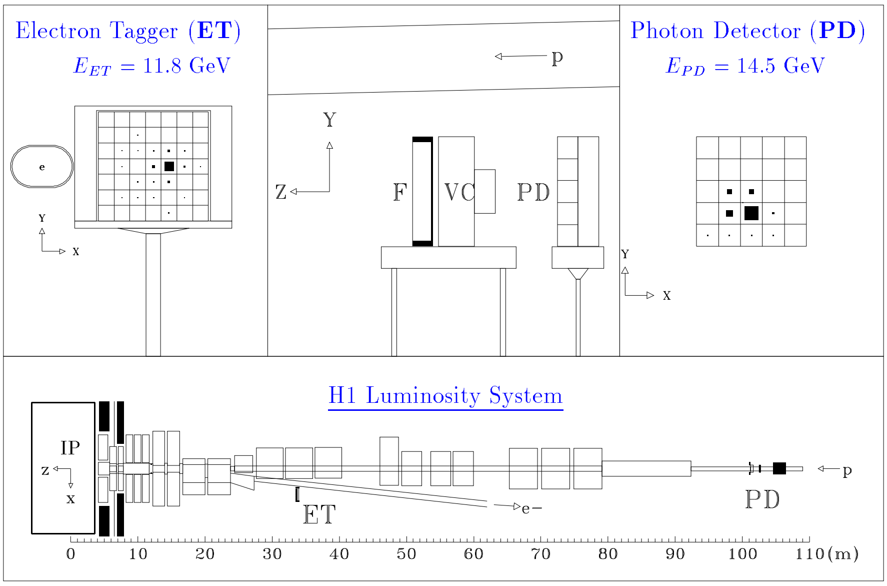

Figure 3.5: Schematic view of the H1 luminosity system.

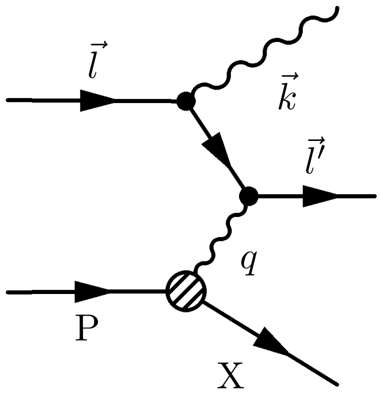

Figure 3.6: Bethe-Heitler process ($\vec{k} \parallel \vec{l} \parallel \vec{l}'$) in *ep* scattering.

streams of events for the purposes of monitoring and calibration of some subdetectors. A small fraction of events rejected by L4 are brought off and written to tape to enable monitoring of the effects of the L4 decisions.

The full event reconstruction is processed by dedicated workstations within typically a day of data taking. The events are also classified into different physics classes dependent on physics area of interest. This can be considered as the fifth level (L5) of the H1 trigger system. The full events are written to Production Output Tapes (POT) and stored.

3.2.4 The H1 luminosity system

A fast luminosity measurement is provided at the H1 detector by small angle electron and photon detectors in the electron direction, which are installed in the accelerator tunnel (see Figure 3.5).

Furthermore, this system allows for detection and triggering on scattered electrons at very low $Q^2 \lesssim 10^{-2}$ GeV^2.

The luminosity measurement is enabled by the Bethe-Heitler radiative process $ep \to e\gamma p$ (see Figure 3.6). This process has a large, well known and exactly calculable cross-section [44], which allows to use this reaction to accurately measure the luminosity. The sum of outgoing e and γ energies is constrained, in the limit $Q^2 \to 0$, to the electron beam energy, i.e. $E_e = E_{e'} + E_\gamma$. The thresholds are applied at 5 GeV to both energies to remove noise and trigger threshold effects.

The electron and photon detectors are TIC1/TIBr crystal calorimeters, with a resolution of $\sigma(E)/E \simeq 10\%/\sqrt{E}$. The electron tagger (ET) is located at position $z = -33$ m and the photon detector (PD) at $z = -103.1$ m. The electron detector detects electrons with an energy fraction between 0.2 and 0.8 with respect to the beam energy and angles $(180° - \theta) \leq 5$mrad and is also used as a trigger for photoproduction interactions, in which case it is combined with a veto against there being a photon in the small angle photon detector. The ET consists of 49 crystal calorimeters read out by photomultipliers. The PD consists of 25 crystals of the same design as the ET. A lead filter (F), which protects the photon detector proper from the high synchrotron radiation flux, is mounted before the ET together with Cerenkov Veto Counter (VC) which rejects events with photons originating from interactions in the filter.

3.2.5 The Time-of-Flight Detectors

Fast scintillation detectors at H1 are needed in order to distinguish real *ep* interactions from proton induced background appearing upstream the detector. The particles produced from *ep* interaction will arrive at a different time than particles produced from the background interactions relative to the nominal time of the bunch crossing. This is caused by different path lengths and different times of interactions. Background events produced near the nominal vertex cannot be distinguished from genuine *ep* interaction in this way, the scintillation counters, however, give a significant reduction of the background.

The Time-of-Flight (ToF) system consists of a number of components. Scintillators are mounted between the backward end-cap of the return yoke and the beam pipe (BToF), within the unused gaps of the PLUG absorber (PToF) and around the beam pipe in the region of the FMD (FToF). In addition, the inner and outer veto walls are situated backward of the return yoke at $z = -6.5$ m and $z = -8.1$ m respectively. These are known as the Veto Wall and detect particles (mostly muons) from the proton beam halo.

The SpaCal calorimeter, which is close to the beampipe in the direction of the incoming protons, is also used for ToF purposes.

3.2.6 Muon Detection

Detection of muons is provided at H1 by two systems. The Central Muon System (CMD) consists of streamer tube chambers inside the instrumented iron return yoke. The Forward Muon System (FMD) consists of four sets of drift chambers designed to measure the polar angle θ, and two sets of drift chambers designed to measure the azimuthal angle ϕ.

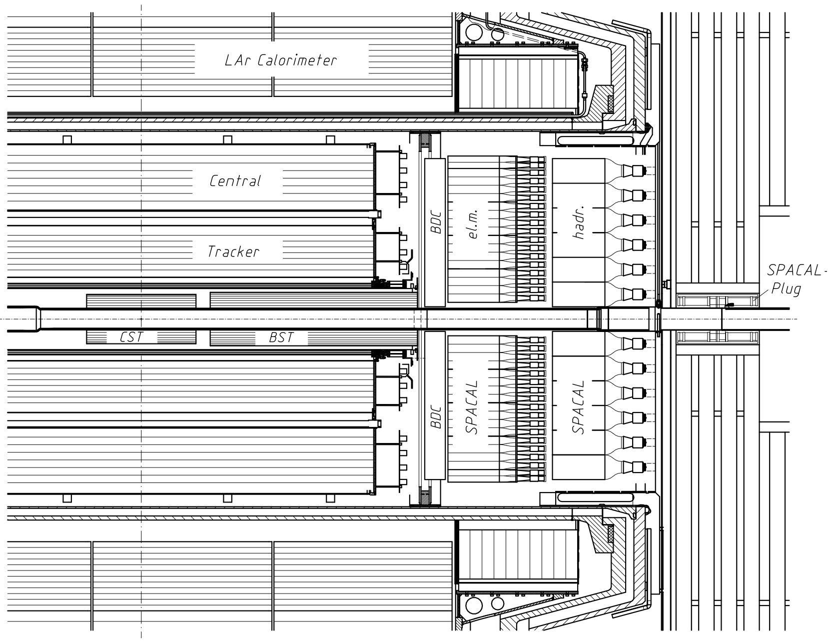

Figure 3.7: The position of the SpaCal calorimeter in the backward part of the H1 detector.

3.3 The SpaCal calorimeter

This section briefly describes the SpaCal calorimeter design and parameters; for a detailed description of SpaCal see [45, 46]. The name of the calorimeter is an abbreviation for *Spaghetti Calorimeter* and refers to the calorimeter design.

Figure 3.7 shows the position of the SpaCal in the backward region of the H1 detector. The front face z-position is -150 cm in the H1 coordinate system. The SpaCal has a diameter of 160 cm (see Figure 3.8) and consists of electromagnetic (EM) and hadronic (HAD) sections with an active depth of 25 cm each.

The SpaCal is built in the H1 detector as a replacement of a lead-scintillator calorimeter (BEMC). Thus its technical parameters are determined by the arrangement of other H1 subdetectors. The depth is limited by the distance between the end of the central tracker and the return yoke. The maximum weight of SpaCal depends on the inner rails of the cryostat which can support 8 tons in the backward region [46]. Technical parameters of the EM and HAD sections are summarized in Table 3.3. The acceptance of the HAD section is increased to 178.7° by a backward plug section (BPLUG) which is mounted on the return yoke.

The electromagnetic section of SpaCal consists of 1192 cells with an active volume $40.5 \times 40.5 \times 250\,\mathrm{mm}^3$ each. A front view of the SpaCal electromagnetic section is shown in Figure 3.8. The cells consist of lead sheets with grooves into which scintillating fibers are laid. Incident particles shower in the lead and cause the fibers to scintillate. The light is then collected at one end of the fibers and measured by a photomultiplier (PMT). The profile of a lead sheet is shown in Figure 3.9. The lead/fiber ratio is 2.27:1. A 2-cell-unit, see Figure 3.10, consists of 52 stacked lead plates with 4680 fibers each. Eight of these pairs are held together to form a supermodule.

The HAD section consists of 136 cells of $120 \times 120 \times 250\,\mathrm{mm}^3$ providing an equivalent of one nuclear interaction length. The fibers are of the same type as in the EM section but have a

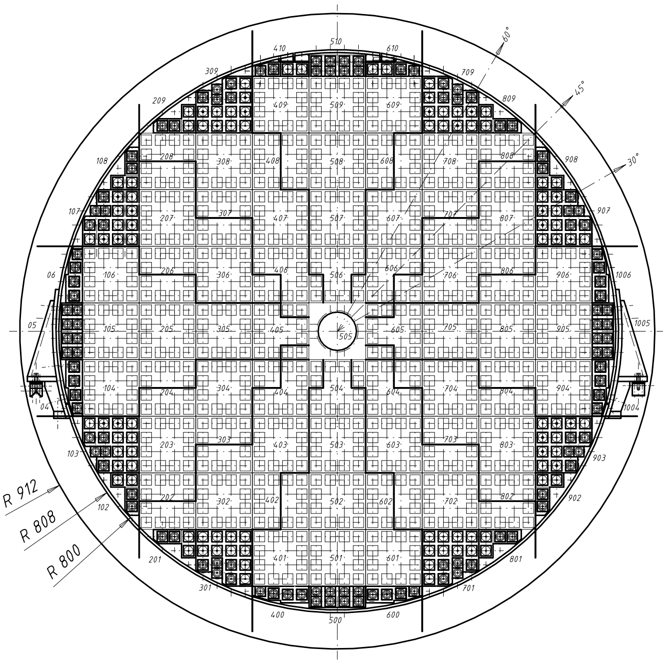

Figure 3.8: The XY cross section view of the electromagnetic SpaCal calorimeter.

	Electromagnetic	Hadronic
Fiber Diameter	0.5 mm	1.0 mm
Fiber Type	Bicron BCF-12	Bicron BCF-12
Pb/Fiber Ratio	2.3:1	3.4:1
Pb-Fiber Density	$7.3\,g/cm^3$	$7.7\,g/cm^3$
PMT Type	Hamamatsu R5505	R2490-06
Cell Size	$40.5 \times 40.5\,mm^2$	$120 \times 120\,mm^2$
Number of Cells	1192	136
Angular Coverage	$\leq 177.5°$	$\leq 178°$
Active Length	25 cm	20 cm
Radiation Length	0.91 cm	0.85 cm
Interaction Length	25 cm	20 cm
Molière Radius	2.55 cm	2.45 cm

Table 3.3: Technical parameters of the SpaCal Calorimeter.

larger diameter of 1.0 mm. The construction of the HAD section is similar but the cells are assembled individually.

The BPLUG consists of 12 cells of trapezoidal cross-section which are arranged in a ring surrounding the beam pipe and four veto layers of 8 mm width. At the inner radius of 5.7 cm a tantalum frame shields against synchrotron radiation from the beam. The veto layers are used to measure potential energy leakage into the beam pipe.

The PMTs have to operate in the 1.2 T magnetic fields. The chosen PMTs (Hamamatsu mesh-dynode type) provide a typical gain of 10^4, a factor of 100 smaller than in case of no field [47]. Each supermodule is furnished with a high-voltage (HV) distribution module which provides a high-voltage for PMTs. A calibration module (CAM) is attached to the rear of each supermodule. A CAM contains control electronics and two pulsed LEDs which feed light through

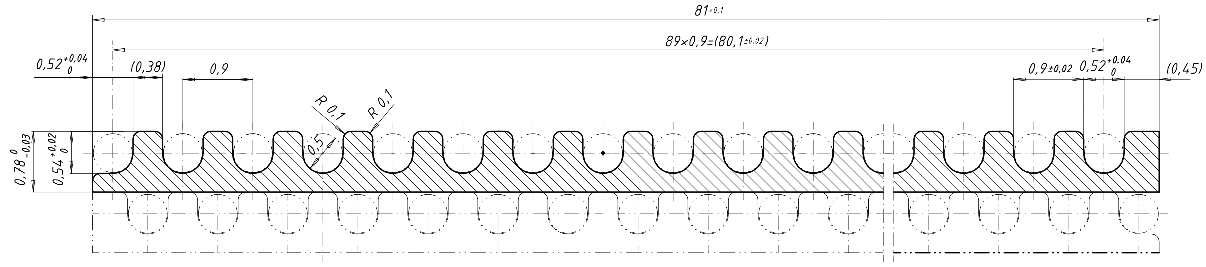

Figure 3.9: The profile of lead sheets (Electromagnetic SpaCal).

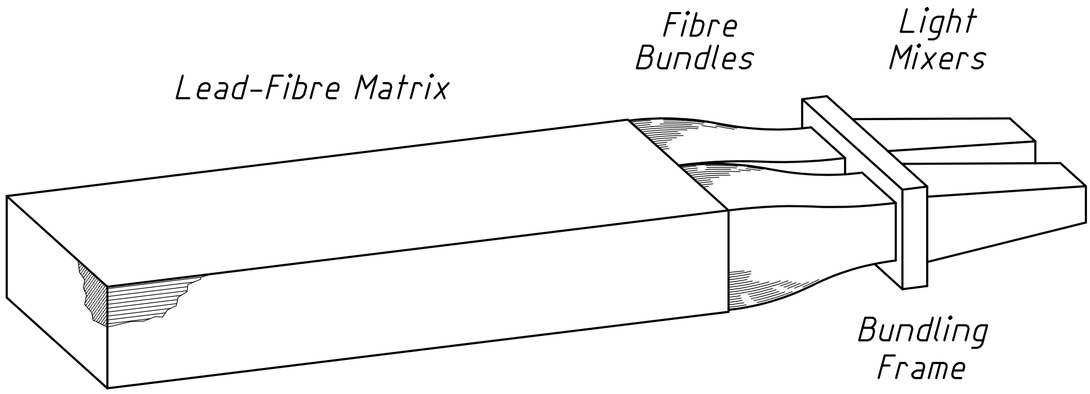

Figure 3.10: The module of Electromagnetic Spacal calorimeter.

fibers into light mixers and PMTs. Potential instabilities of the light output of each LED are monitored by photodiodes. The LEDs are typically pulsed at a rate of 1 Hz, synchronised to empty HERA bunches. LED pulses are used to monitor the stability of the photomultiplier gains and therefore important for the calibration of the calorimeter [48].

3.4 The Backward Silicon Tracker

The Backward Silicon Tracker (BST) serves for the precise measurement and identification of the scattered electron in the backward region, corresponding to four momentum transfers squared Q^2 between approximately 0.3 GeV^2 (for the shifted vertex position) and 20 GeV^2 (for the nominal vertex position). Inclusive *ep* DIS measurements can benefit from the BST in two ways

- At **high y**, where the BST due to its low sensitivity to neutral particles is able to suppress their contribution to electron signals in SpaCal.
- At **low y**, where the hadronic final state is going forward, hence, the vertex reconstruction efficiency is too low in the standard track detector due to missing acceptance. In this case the vertex can be reconstructed from the electron side, using BST.

Moreover, the polar angle is measured independently of the central tracker vertex with an accuracy of about 0.2 mrad.

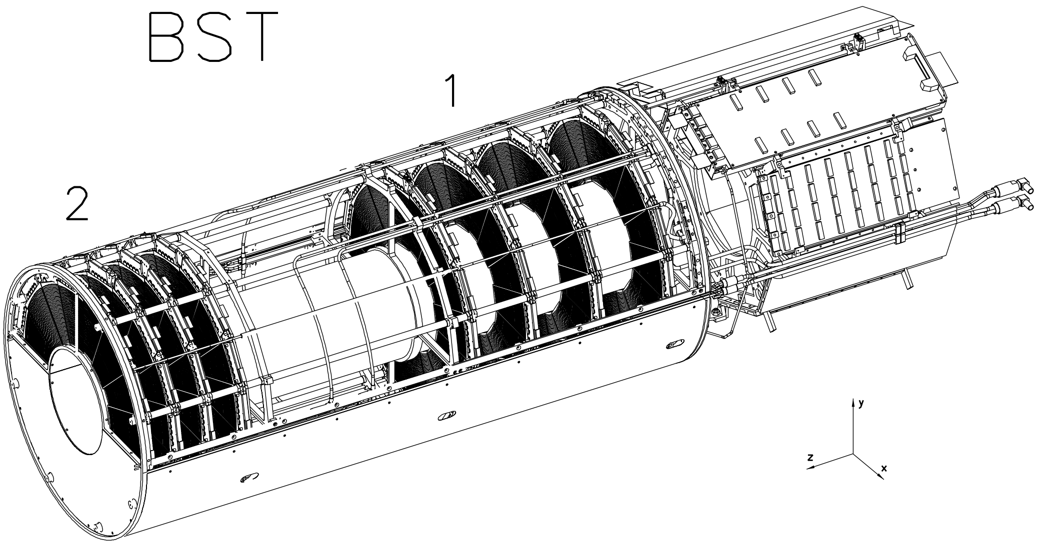

Figure 3.11: Isometric view of the Backward Silicon Tracker. The part marked by label 1 corresponds to BST as it was used during 1997 HERA running. The park marked by label 2 was added to improve the BST acceptance at larger values of Q^2.

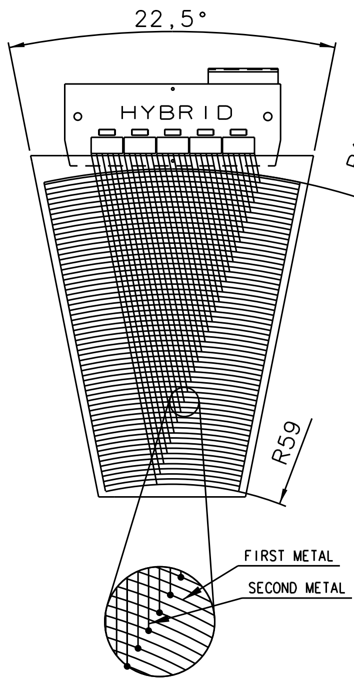

Figure 3.12: The Backward Silicon Tracker wafer.

The detector itself (see Figure 3.11) is composed of two symmetric half shells, enclosed by inner and outer shield made from G10 foil carrying a double sided 35 μm Cu layer. Each half shell contains 8 planes of active sensors, called *wafers*, aligned symmetrically around the detector z-axis. There are 16 sensors on each plane.

Wafers

The active sensors (see Figure 3.12) are made from 250 μm thick n-type silicon. A single minimum ionizing particle creates about 22000 electron-hole pairs, which is sufficient to produce a clear signal. Applying a depletion voltage between p-side and n-side of the silicon sensors creates a reverse biased p-n-junction.

The contribution of the wafers to the dead material in front of SpaCal is less than 3% of X_0. However, due to electronics, mechanics and cabling, the BST contributes to the dead material by a significantly larger factor of 10-30% of X_0, depending on the angular range.

Each sensor has 1280 concentric AC coupled p^+ strips with a pitch of 48 μm, every second of them is being read out. Hence there are 640 readout channels per sensor. The wafer has a double metal layout which allows to route the signals from all p-strips to the outer radius where the possible radiation damage is lower than inside. The disadvantage of this arrangement consists in a lowered S/N ratio of ≈ 15 as compared to ≈ 30 for single metal BST wafers later installed.

Data Acquisition

The large number of readout channels requires a highly integrated front-end system. Furthermore, due to the high bunch repetition rate of 10.4 MHz the system is equipped with multi-event pipeline buffers in order to separate the processing stage and the online hit finding procedure from the front end data.

The BST data processing chain consists of a number of steps

1. **Front end readout** - signals from strips are driven via bonded wires directly to the front end electronics, which is placed on boards glued to wafers, so called *hybrid boards*. The main components of these boards are five Analog Pipeline Chips (APC), which were developed especially for H1, five digital decoder chips and one analog cable driver. The decoder chips generate steering signals for the APC chips from only four signal lines per wafer.

   Each APC chip handles the sampling of 128 parallel channels. It consists of low power, low noise charge sensitive preamplifiers followed by a storage array of pipeline capacitors. The depth of the pipeline is 32 bunch crossings in order to keep information about BST till the first level trigger decision is taken within about 2.5 μs. When the trigger stops the sampling, the pipeline can be re-read by the input preamplifier and the charge is stored on a latch capacitor of each channel. The process of sampling and reading is controlled by a special *sequencer code* running on the OnSiRoC module (see below).

2. **Repeater Boards** - voltage supply, signal transmission and APC steering is realized via repeater boards mounted behind the active BST area and connected to hybrids by *strip lines*. The boards consist of eight multi-layer printed circuit boards placed concentrically around the beam pipe. The sixteen detectors of two sectors each are connected to one repeater board. An output amplifier is used to transmit the signal via about 30 m long coaxial cables to the electronic trailer next to the H1 detector.

3. **OnSiRoC** - The Online Silicon Readout Controller VME module was developed in order to control sampling and readout of APC chips on the hybrid board. It contains a single channel sequencer, a programmable unit, power supply system, pedestal memory, buffer and channel counters, channel sampling ADC and raw data memory. The complete analog readout and digitization needed is about 1 ms, hence, no additional dead time is introduced by the system.

   For the BST, the OnSiRoC is used mainly for the sequencer code running whilst the other functions are distributed to further VME modules[1]. The hybrid electronics and bias voltages are supplied by *converter cards* while the analog to digital signal conversion and hit recognition is done on commercial *Power PC boards* equipped with 10 MHz FADC.

4. **PowerPC and online data processing** - Signals from wafers are digitized by 12-bit ADCs, which are via PCI interface connected to Power-PC-based VME modules. Here the signal is online processed by a hit finding algorithm. Since the BST delivers a data flow of about 40000 digital signals per event, the data size has to be reduced by orders of magnitude within short time of about 10 ms, to fit to the 4 kbyte storage space for the BST readout branch.

5. **Hit reconstruction** - The hit reconstruction procedure is initialized by using $n = 64$ events in order to estimate values of pedestal and noise per each channel. These are derived from common mode[2] corrected amplitudes A_i, pedestals P_i and noise squared N_i applying weight $w = 1/n$ and using the following iteration formula

$$\begin{aligned} P_i' &= (1-w)P_i + A_i, \\ N_i' &= (1-w)N_i + w(A_i - P_i)^2. \end{aligned} \tag{3.1}$$

   The hit finding procedure determines common mode and common slope for each APC chip by a straight line fit to amplitudes with pedestals subtracted versus channel number. In this procedure the noisy strips, outliers and signals are masked out in order not to bias the common mode estimate. The correct amplitude is then calculated according to

$$A_i = A_i^0 - P_i - (C_k + S_k \cdot i), \tag{3.2}$$

   where A_i^0 is the raw amplitude of the strip i with the pedestal P_i of the APC k with the common mode C_k and the common mode slope S_k. A sliding window is used to search for hit clusters. Since the particles pass through the BST almost perpendicularly a window width of three channels is sufficient. The cluster is treated as a signal if the sum of the amplitudes squared in the window exceeds a certain threshold which actually depends on the noise.

6. **Offline data processing** - The offline BST reconstruction code (BSTREC) is searching for tracks in the BST by means of calculating *triplet sagitta* $s = (r_1 + r_3)/2 - r_2$ between the hit coordinates r_i measured in three successive planes i. This quantity exhibits a clear signal from tracks at top of a low combinatorial background, hence, it can be used for track searches. However, the detector must be well aligned prior to this procedure.

[1] The CST operation uses the OnSiRoC module also as a low voltage power supply.

[2] Hereafter by *common mode* is meant a collective modulation of the strip amplitudes, which must be subtracted in order to reconstruct hits correctly.

For the physics analysis a special track founding algorithm was developed [49], hereafter called *BST electron finder*. This algorithm performs track reconstruction in the BST using additional information from SpaCal in order to recognize electrons and to extend the BST acceptance.

Apart from the steps described above, a precision analysis based on the BST requires a careful treatment of detector efficiency, noise and various effects which can enter both data as well as Monte Carlo simulations. These are in more detail described in analysis Section 4.4. The alignment procedure is introduced in Section 4.3.

Chapter 4

Data analysis

The data samples, analyzed in this thesis, were taken in 1999/2000 during two special *minimum bias* running periods. The notion 'minimum bias' refers to the fact that the trigger setup was simplified in order to achieve high trigger efficiency and low prescales, hence, to minimize the errors of the measured cross section. Both data samples were taken with proton beam energy of 920 GeV and electron beam energy of 27.55 GeV.

Minimum bias

The sample was taken at HERA during the November/December 1999 running period with a total luminosity of about 2700 nb^{-1} and the interaction vertex at the nominal position. Hereafter the sample is denoted as **mb99**.

Shifted vertex

The sample was taken at HERA in the summer 2000. In a dedicated HERA run the interaction vertex was shifted by +70 cm thereby accessing a region of lower Q^2 than at nominal vertex position. The total luminosity collected was about 607 nb^{-1}. Compared to a similar run taken in 1995 [50] the statistics is about four times larger and the BST is newly installed. Hereafter the sample is for clarity denoted as **svtx00**.

This chapter continues with the description of the kinematics reconstruction, in Section 4.1. Section 4.2 contains information about triggers used in the analysis. Detector alignment and calibration are described in Section 4.3 and 4.5, respectively. Section 4.4 is devoted to the treatment of the backward silicon tracker BST. Run and event selections are introduced in Section 4.6 and 4.7 respectively. Adjustments of the Monte Carlo simulations are explained in Section 4.8 and 4.9. Finally, a measurement of the inclusive scattering cross section and an analysis of the F_2 rise are presented in Section 4.10 and 4.11. The chapter is closed by a determination of F_L in Section 4.12.

4.1 Kinematics reconstruction

The kinematics of DIS events was introduced in Section 1.1. It is described by the four momentum transfer Q^2, the Bjorken variable x and/or the inelasticity y. These variables are bound together by the approximate relation $Q^2 = xys$, where s is the square of the center of mass energy and can be evaluated as $s = 4E_eE_p$ since the masses of particles are negligible.

The precise reconstruction of the kinematics is essential for DIS cross section measurements. There are various methods existing, involving a measurement of the scattered electron as well as of the hadronic finale state.

In terms of the scattered electron energy E'_e and the polar scattering angle θ_e the kinematic variables are evaluated according to the following relations

$$y_e = 1 - \frac{E'_e}{E_e}\sin^2\frac{\theta_e}{2} \qquad\qquad Q^2_e = 4E'_eE_e\cos^2\frac{\theta_e}{2} = \frac{E'^2_e\sin^2\theta_e}{1-y_e}. \tag{4.1}$$

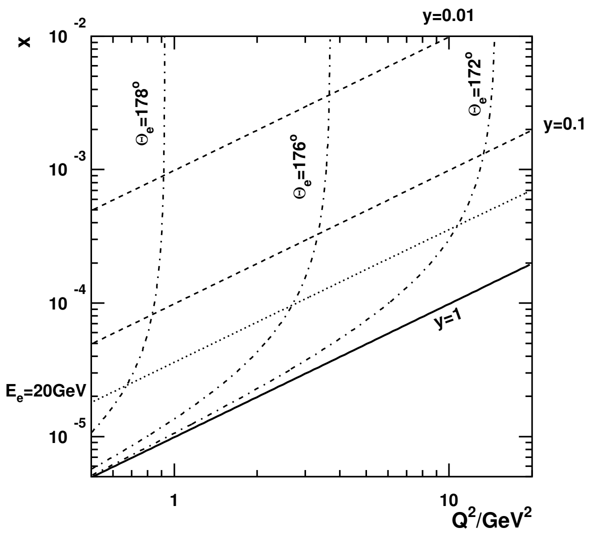

Figure 4.1: Kinematic plane in the region of low Q^2 and x. Dashed and dotted lines correspond to constant inelasticity y and scattered electron energy E'_e, respectively. Dot-dashed lines correspond to constant electron scattering angle θ_e.

The variable x is calculated as $x_e = Q^2_e/s\,y_e$. Equations (4.1) define the so called *electron method*, which is not dependent on the reconstruction of the hadronic final state. The prefix e is used to denote this method.

Analyzing the above formula for large scattering angles $\theta_e > 150°$, where the scattered electron is detected in SpaCal, the inelasticity variable y depends predominantly on the scattered electron energy. Hence, the large y domain corresponds to low energies E'_e. On the other hand, at low y, where $E'_e \sim E_e$, the determination of Q^2 is almost entirely defined by the scattered electron angle (see Figure 4.1).

Relations for measurement errors are obtained from eq. (4.1) in a straightforward way:

$$\begin{aligned}
\frac{\delta Q^2}{Q^2} &= \frac{\delta E}{E} \oplus \tan\frac{\theta_e}{2}\delta\theta_e, \\
\frac{\delta x}{x} &= \frac{1}{y}\frac{\delta E}{E} \oplus \tan\frac{\theta_e}{2}\left(x\frac{E_p}{E_e} - 1\right)\delta\theta, \\
\frac{\delta y}{y} &= \frac{1-y}{y}\frac{\delta E}{E} \oplus \frac{1-y}{y}\cot\frac{\theta_e}{2}\delta\theta_e.
\end{aligned}$$

Based on these equations the following conclusions can be drawn for the kinematics reconstruction

- Due to the factor $1/y$ the resolutions of x and y deteriorate at low y.
- The resolution of Q^2 is good for most of the HERA kinematic range, except at high θ_e due to the factor $\tan\theta_e/2$.
- The effective incoming electron energy is often reduced by the emission of a real photon. This effect is not taken into account in the former equations, leading to a biased event kinematics for this type of events.

Apart from the electron side, the kinematics can be reconstructed from the hadronic final state measurement. However, since the apparatus is not perfectly hermetic and does not cover the full 4π angle, leakage of particles must be treated carefully. In the H1 detector, due to the large difference in beam energies, effects of particle leakage are most pronounced along the outgoing proton beam. Hence, a method to reconstruct kinematics from hadronic variables should use variables which are most insensitive to these losses.

A method to determine x and Q^2, proposed by A. Blondel and P. Jacquet [51], does not require any jet identification algorithm or proton structure hypothesis. Replacing the momentum transfer $q = k - k'$ in eq. (1.2) by $(p_h - p)$, where p_h is the four-momentum of the total outgoing hadronic final state, gives

$$y = \frac{p \cdot (p_h - p)}{p \cdot k} \qquad\qquad p_h = \sum_h (E_h, p_{xh}, p_{yh}, p_{zh}). \tag{4.2}$$

In a similar manner, the transverse electron momentum $E_e^{'} \sin\theta_e$ in eq. (4.1), due to momentum conservation, may be replaced by the total transverse momentum p_t of the hadronic finale state. Furthermore, it is useful to introduce a new variable, corresponding to the total $E - p_z$ of the whole hadronic final state

$$\Sigma = \sum_h E_h(1 - \cos\theta_h). \tag{4.3}$$

After straightforward mathematics and neglecting the particle masses one finally obtains the following relations

$$y_h = \frac{\Sigma}{2E_e} \qquad\qquad Q_h^2 = \frac{p_t^2}{1 - y_h}, \tag{4.4}$$

where p_t is the total transverse momentum of the hadronic flow. In analogy with the electron method, the variable x is calculated as $x_h = Q_h^2/s\, y_h$. The index h was used as an abbreviation for 'hadron' to denote this method. A combination of Q_e^2 and y_h leads to the mixed method [52] which uses the best measurement of Q^2 and avoids the $1/y$ divergency of the electron method.

As in the case of the electron method, due to the presence of the electron beam energy E_e in eq. (4.4) both the hadron and the mixed methods are sensitive to collinear real photon emission from the incoming electron. This sensitivity can be significantly reduced by replacing factor $2E_e$ by the total $E - p_z$ of all particles, i.e. $\Sigma + E_e'(1 - \cos\theta_e)$. The corresponding method is called *sigma method* and combines the measurement of both electron and hadronic final state. The kinematics is reconstructed as follows

$$y_\Sigma = \frac{\Sigma}{\Sigma + E_e'(1 - \cos\theta_e)} \qquad\qquad Q_\Sigma^2 = \frac{E_e'^2 \sin^2\theta_e}{1 - y_\Sigma}. \tag{4.5}$$

The resolution of the y_Σ variable is similar to that of the y_h variable while it is more robust against photon radiation[1] from the initial electron and hereafter will be preferred. A resolution study of kinematics reconstruction methods described above can be found in [53].

L1 subtrigger	Definition	L2 condition	L4 finder
s0	IET > 1 ‖ CIET > 2 v:3, f:1	R> 10 cm	-
s3	IET > 2 ‖ CIET > 3 v:3, f:1	-	-
s9	IET > 0 v:3, f:1, t:3, z:0	-	high y finder

Table 4.1: Subtriggers, used in this analysis, are based on the backward calorimeter SpaCal. Subtrigger s9 is complemented by vertex and track requirement (see text) and subtrigger s0 by a SpaCal radius cut at the trigger level L2. The high y finder at trigger level L4 is based on subtrigger s9.

4.2 Trigger

A brief description of the H1 trigger system was presented in Section 3.2.3. For both data samples, i.e. mb99 and svtx00, the setup of the relevant triggers was identical. Subtriggers, used in this analysis, are listed in Table 4.1. Each subtrigger requires a minimum energy deposit in the SpaCal calorimeter, corresponding to a certain IET/CIET threshold. CIET refers to the central region of the SpaCal calorimeter while IET to the bulk part. Apart from SpaCal energy deposits a combination of additional trigger elements is required. The elements of type 'v' are related to the requirement on absence of VETO, BToF, VLQ and Spacal ToF background signals. The element f:1 demands a check of FToF and PLUG veto signals. More important is the element z:0 of the L1 vertex trigger [54], which is based on the fast histogramming of hits in z-chambers CIP and COP (Section 3.2.1) and to the search for the histogram maximum. Finally, t:3 refers to the track requirement in the central or forward tracker.

L2 conditions are complementary to L1 subtriggers. In both data samples, analyzed in this thesis, only subtrigger s0 contains an L2 condition: the requirement that the energy deposit in the SpaCal plane satisfies $\max(|x_{Sp}|, |y_{Sp}|) > 8\,\mathrm{cm}$, where x_{Sp} and y_{Sp} are coordinates of the energy deposit.

At L4 trigger level a special finder to search for high y events is defined, based on subtrigger s9. The following requirements must be met in order to flag an event as the high y candidate:

- $R_{max} > 15\,\mathrm{cm}$ - at least one cluster is required to have the radius in the SpaCal plane larger than 15 cm.
- $E_{max} > 2\,\mathrm{GeV}$ - at least one cluster has energy exceeding 2 GeV.
- $R^{cl}_{min} < 5\,\mathrm{cm}$ - at least one cluster has a transverse size smaller than 5 cm.

The above conditions are, however, implemented in the analysis code[2], and the L4 finder is not used explicitly. Such a procedure is safe due to the special L4 setup in mb99 and svtx00 running periods, when events were neither rejected nor prescaled by the L4 farm. Hence, due to the fact that all events are present on data tapes and in order to minimize errors coming from high y finder inefficiencies, the L4 finder is not further considered in this analysis.

Subtrigger selection

There are three particular analyzes performed on the two data sets mb99 and svtx00 in this thesis. The analyzes of the bulk regions are based on subtriggers s0 and s3. In the case of

[1] However, radiative effects are much reduced by analysis cut on total $E - p_z$, which will be introduced in Section 4.7.

[2] With an exception of the radius cut, where a lower value of 12 cm is used for the event selection.

a)

Data sample	Subtriggers	Comment
mb99	s0 s3	bulk region
mb99	s9	high y analysis
svtx00	s0 s3	bulk region

b)

Subtriggers	mb99	svtx00
s0	1.21	1.15
s3	1.46	1.44
s9	1.10	1.00

Table 4.2: Subtrigger selection for analyzed data samples (a) and average prescales of relevant subtriggers (b).

the mb99 data, a special analysis of the very high y region was done based on subtrigger s9 alone. A similar analysis on svtx00 data could not be performed due to the low efficiency of trigger elements based on tracks and vertex reconstruction. This effect was caused by shifting the vertex out of nominal region of track trigger elements during these runs, from the middle part of the central tracker towards its $+z$ edge. The selection of subtriggers is summarized in Table 4.2.

Event weighting

Due to the high rate of DIS interactions (especially at low Q^2) and due to the high rate of background events (at high y), some subtriggers exhibit high rates. The detector readout speed is limited by hardware abilities, therefore such subtriggers are *prescaled*. Although a subtrigger gives a trigger signal for particular events, not all of them are recorded onto tape. The fraction of events recorded depends on the so called *prescale factor*. For example, if the factor is four, every fourth event (statistically) triggered by the subtrigger is read out and recorded. A signal from a subtrigger generates a *raw* trigger bit. If the prescale condition is passed an *actual* trigger bit is set. Prescales are *run-dependent* and calculated according to actual conditions by a so called *AutoPresale* algorithm.

The above described prescale procedure implies that recorded events must have assigned a weight, depending on prescales and subtriggers active in an event. The purpose of the weighting algorithm, used in this analysis, is to divide the total phase space of measured DIS interactions into non-overlapping regions with only one subtrigger assigned to each of them. Subtriggers with smaller prescale are given priority in case more than one trigger condition was satisfied. In a weighting process only the corresponding subtrigger for each region is taken into account, other subtriggers are ignored. The weight of the event is equal to the subtrigger prescale factor.

The algorithm is graphically sketched in Figure 4.2. A set of subtriggers (a) divides the overall phase space into a number of regions, which are covered by one, two or three subtriggers. Assume that the prescale factors $P()$ are ordered as follows: $P(T1) > P(T3) > P(T2)$. The application of the described selection algorithm implies a division of phase space into three regions, see Figure 4.2 (b), each covered exclusively by one subtrigger. The event weight is equal to the prescale factor of the subtrigger which covers the corresponding region and actually triggered this event. Therefore no statistical weight calculation is needed. An advantage of this algorithm is that it allows to use *average trigger prescales* instead of run-dependent prescales[3] in order to minimize effects of large trigger weights. Average prescales for considered subtriggers are listed in Table 4.2 (b). Subtrigger s9 has the lowest prescale and in the svtx00 data set it was essentially unprescaled. However, as already mentioned, this is due to the low efficiency of this subtrigger in the svtx00 data.

[3]As long as the prescale hierarchy is conserved for all analyzed runs. This requirement is equivalent to the demand that the division of phase-space, see Figure 4.2 (b), is identical for all runs.

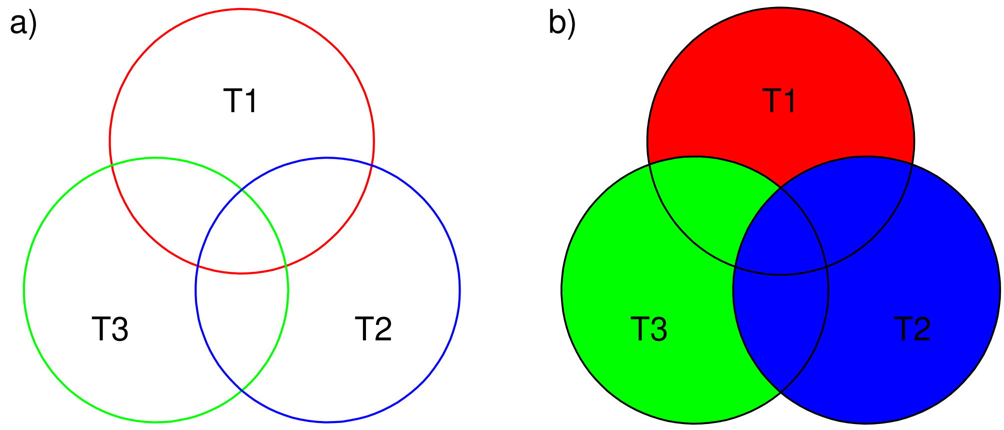

Figure 4.2: An illustration of the event weighting algorithm based on subtrigger prescales. In figure (b), for example, the prescale factors $P()$ are ordered as follows: $P(T1) > P(T3) > P(T2)$.

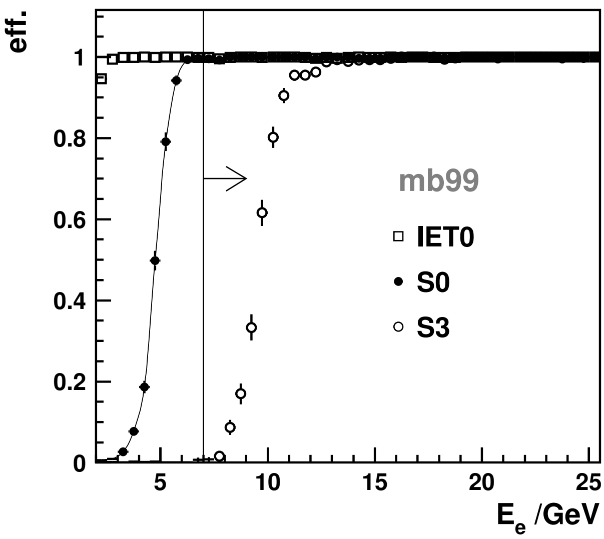

Figure 4.3: The efficiencies of subtriggers s0 (closed points), s3 (opened points) and of the IET0 trigger element as a function of electron energy E_e for mb99 (a). The arrow corresponds to the energy cut $E > 6.9$ GeV used in the analysis based on s0 and s3 subtriggers.

Trigger performance

The knowledge of subtrigger efficiencies is essential for precision cross section measurements due to their direct influence on the measurement results. The efficiency of a subtrigger is calculated as a fraction of events with the raw bit set *on* in a sample of events triggered by an independent set of subtriggers or a more general subtrigger.

Subtrigger s0 deserves a special attention due to the fact that it covers a major part of phase-space of the subtrigger s3 and hence it works as a back-up subtrigger compensating s3 inefficiencies. The s0 subtrigger is highly efficient in the whole phase-space considered. The efficiency of subtrigger s0 is in the mb99 data set is determined from the data using a sample of events triggered independently of the SpaCal triggers. In the svtx00 data the H1 trigger system was

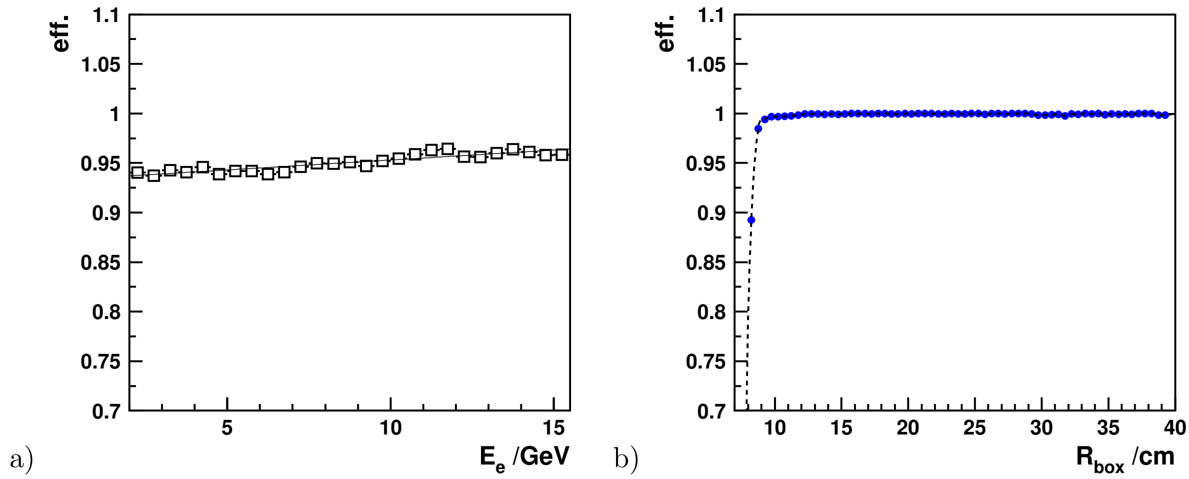

Figure 4.4: The efficiency of the t:3 trigger element of subtrigger s9 as a function of the SpaCal cluster energy (a). The efficiency of the L2 trigger level condition of subtrigger s0 as a function of $R_{box} = \max(|x_{Sp}|, |y_{Sp}|)$ in the SpaCal plane (b).

essentially based on the SpaCal triggers only. Thus the s0 efficiency was determined using events triggered by the s0 trigger element CIET with another cluster in the IET trigger element acceptance, and vice versa. Figure 4.3 shows the trigger efficiency for the s0 subtrigger as a function of cluster deposit energy for the mb99 data set. The efficiency of subtrigger s0 is practically identical to that of the IET>1 || CIET>2 subtrigger condition. The trigger threshold was set to approximately 6 GeV, where the efficiency is seen to steeply rise towards higher energies and it reaches a plateau of about 100% efficiency at ≈ 7 GeV.

In the same manner the efficiency of the s3 subtrigger is evaluated, see Figure 4.3 (open points). Since the trigger threshold was set higher than that of the s0 subtrigger, namely to approximately 12 GeV, the subtrigger efficiency saturates at about 100% at higher energies.

The efficiency of subtrigger s9 is composed of the efficiency of the IET>0 trigger element and of the trigger element t:3 related to tracks in the tracker. As in the case of subtrigger s0, the efficiency of IET>0 trigger element was evaluated on a sample of events triggered by non-SpaCal triggers. Figure 4.3 (a) shows the efficiency (open squares) as a function of cluster deposit energy. In the region of the high y analysis based on the s9 subtrigger it is seen to be 100% efficient (above 3 GeV).

The efficiency of the trigger element t:3 was determined from a sample of events triggered independently on the tracking trigger elements. A raw trigger bit of monitor subtrigger s10 was required. This subtrigger serves for monitoring purposes of the t:3 trigger element. It is identical to the s9 subtrigger except of omitting the t:3 element. The result of the efficiency study is presented in Figure 4.4 (a) as a function of the cluster deposit energy. The trigger element t:3 is seen to be about 95% efficient.

Finally, the efficiency of the L2 trigger level condition (see Table 4.1) of the subtrigger s0 was investigated on a sample of events, triggered by s3 and s9 subtriggers. This condition requires the energy deposit in the SpaCal plane satisfies $R_{box} = max(|x_{Sp}|, |y_{Sp}|) > 8\,\text{cm}$, where x_{Sp} and y_{Sp} are coordinates of the energy deposit. The efficiency is plotted as a function of R_{box} in the SpaCal plane in Figure 4.4 (b) for the mb99 data set. For both data samples the behaviour of the efficiency is as expected. Due to the coarse segmentation on the trigger level L2 the efficiency reaches a plateau of almost 100 % efficiency at about 8.5 cm, while below it falls steeply down. Hence a cut o$R_{box} > 8.5\,\text{cm}$ is performed in the analysis for events triggered exclusively by s0.

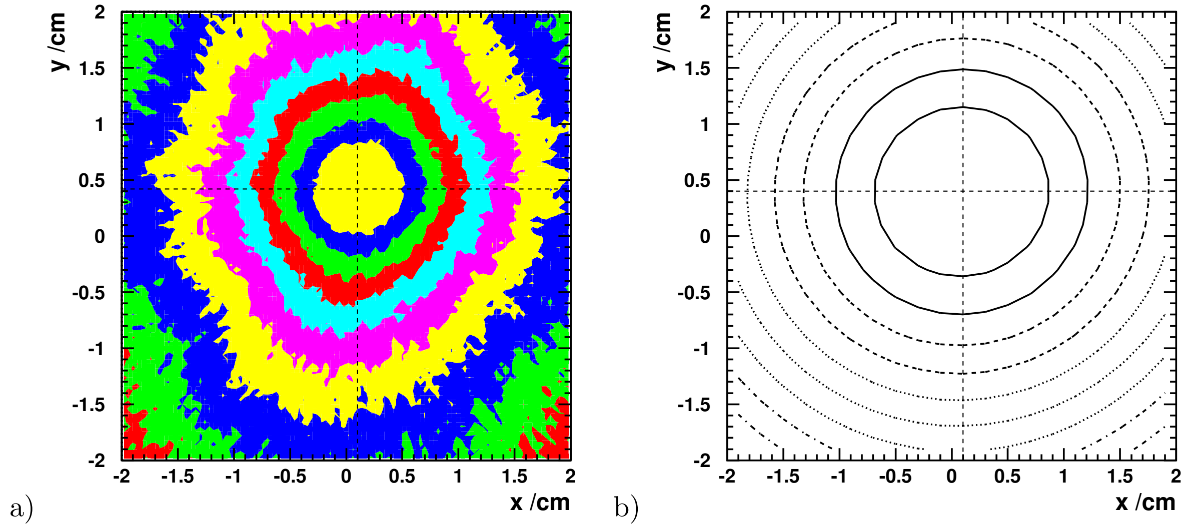

Figure 4.5: A density contour plot of lines connecting electron and photon clusters in QED Compton events set (a) and an acoplanarity minimization contour plot of the functional from eq. (4.7) (b). The full ("bulk") data sample taken in 2000 was used to complement the svtx00 sample by larger statistics.

4.3 Alignment

Precision measurements of the deep inelastic cross section require the kinematics to be reconstructed accurately including the control of the measured phase-space. For both of these tasks the determination of the detector positions is essential. In the presented analysis the detector alignment can be done using *ep* data and it is performed before any further steps are taken.

In this section the alignment of the backward calorimeter SpaCal and of the backward drift chamber BDC is described in Section 4.3.1. The alignment of the backward silicon tracker BST involves a special procedure and it is described separately in Section 4.3.2.

4.3.1 SpaCal and BDC

The H1 detector coordinate system is defined by the central drift chambers in the central tracker, which was introduced in Section 3.2.1. The central jet chambers CJC1 and CJC2 are used for the transverse, $r-\phi$, coordinate measurement, while the z chambers CIZ and COZ determine the z coordinates.

The alignment of the backward calorimeter SpaCal is in the first step performed using *QED Compton events*. In these events the outgoing electron, which is almost parallel to the beam due to the very low Q^2, radiates a real photon. Thus both particles can be detected under large polar angles. They enter the SpaCal almost back-to-back in azimuth so that their total transverse momentum is close to zero. The alignment is based on an algorithm [53] which is connecting both electron and photon SpaCal clusters in a sample of QED Compton events. The density of these connections is largest at the (x,y) position where the beam is crossing the SpaCal plane. Use of Compton events requires large statistics, hence, the analyzed mb99 and svtx00 data sets were complemented by the bulk data taken in 1999 and 2000, respectively. As an example, in Figure 4.5 (a) the resulting contour plot in the central part of SpaCal is shown for the svtx00 data. The run-dependent beam position in the SpaCal x-y plane was subtracted off and thus the highest density is expected to be in the middle of the plot, at (0,0) coordinates. The fact that the density peak is shifted implies a SpaCal misalignment. The SpaCal alignment constants can be obtained directly from the contour plot, from the position of density maximum. They are listed, along with alignment constants for the BDC, in Table 4.3 below. In a similar manner the mb99 data are analyzed complemented by the 1999 bulk data. It can be seen that the whole apparatus was at a constant position, apart from a small effect on δx for SpaCal, over the years 1999 and 2000.

Alternatively to this procedure one can minimize the acoplanarity in order to determine alignment constants [55]. The acoplanarity is defined as

$$A = \phi_1 - \phi_2, \tag{4.6}$$

where ϕ_1 and ϕ_2 are the azimuthal angles of the outgoing electron and photon. In the ideal case the acoplanarity is expected to be close to π. There are various ways how to obtain alignment constants from the acoplanarity, e.g. by minimizing a functional of the form

$$f_A = \sum_{ev.} \frac{(\pi - A)^2}{\sigma^2}, \tag{4.7}$$

where the summation extends over all events in the QED Compton sample and the acoplanarity measurement error squared, σ^2, for a given event is defined as

$$\sigma^2 = \frac{\sigma_x^2\, x_1^2 + \sigma_y^2\, y_1^2}{(x_1^2 + y_1^2)^2} + \frac{\sigma_x^2\, x_2^2 + \sigma_y^2\, y_2^2}{(x_2^2 + y_2^2)^2}. \tag{4.8}$$

In this equation (x_1, y_1) and (x_2, y_2) are positions of the electron and photon clusters in the SpaCal x-y plane for a particular event. The position measurement errors σ_x and σ_y are in the case of SpaCal about 0.3 cm. A contour plot obtained from minimising the functional f_A, eq. (4.7), is shown in Figure 4.5 (b) as a function of x and y. The coordinates corresponding to the minimal value of the functional are the alignment constants. The results of both methods are in very good agreement and are used further in this analysis to align the SpaCal calorimeter in x and y.

The z-position of SpaCal was determined using a comparison of the polar angle measurement of the scattered electron by the central tracker (θ_{CT}) and by the SpaCal (θ_{Sp}). A correction of the z position follows from the distribution of the quantity

$$\Delta z_{Sp} = z_{cl} \left(1 - \frac{\tan \theta_{Sp}}{\tan \theta_{CT}} \right), \tag{4.9}$$

where z_{cl} is the position of a particular SpaCal cluster corresponding to the θ_{Sp} measurement. The distribution of Δz is shown in Figure 4.6 (a). The peak position of the distribution corresponds to the z-shift of the SpaCal with respect to the assumed position, represented by z_{cl} position of a SpaCal cluster.

The backward drift chamber BDC was aligned to the SpaCal by a further polar angle measurement comparison. Figure 4.7 shows the difference of polar angle measurements before (a) and after alignment (b) of the BDC chamber. In analogy to the case of the SpaCal alignment in z-coordinate, the following quantity was employed

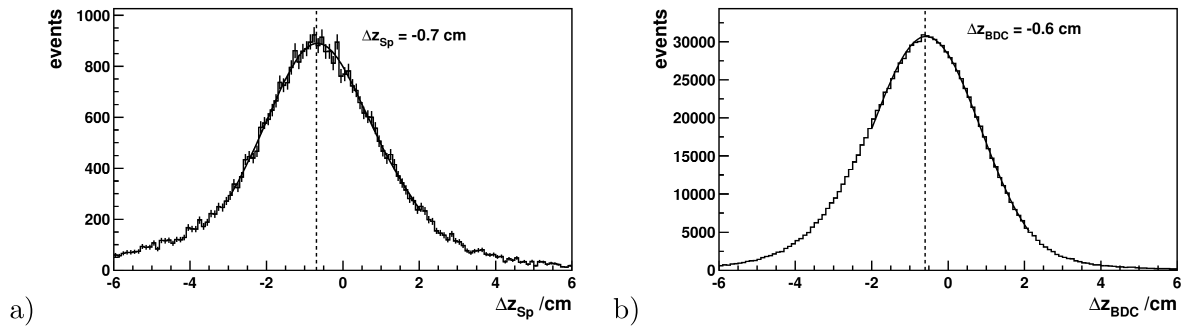

Figure 4.6: SpaCal (a) and BDC (b) shifts in the z-coordinate, as defined in eq. (4.9) and eq. (4.10), respectively. Both BDC and SpaCal were aligned in the x-y plane.

	mb99		svtx00	
	SpaCal	BDC	SpaCal	BDC
Δx	0.095	0.03	0.145	0.03
Δy	0.42	0.20	0.42	0.20
Δz	-0.70	-0.80	-0.70	-0.70

Table 4.3: Alignment constants for correction of SpaCal and BDC positions in mb99 and svtx00 data.

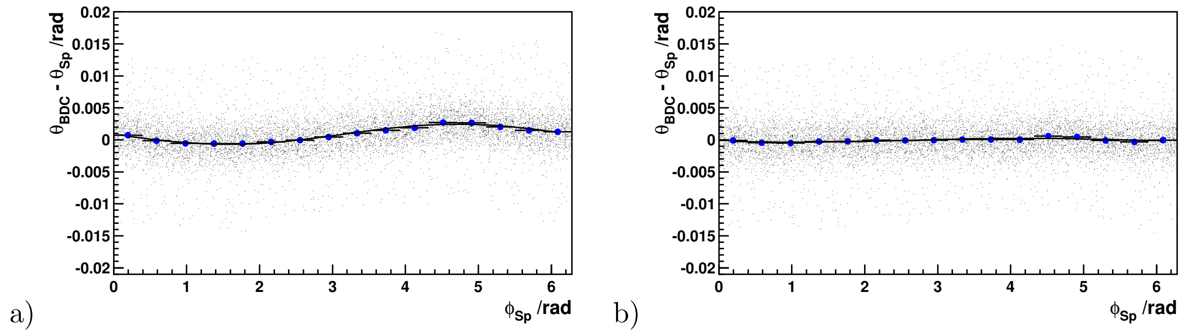

Figure 4.7: Difference in the polar angle measurements $\theta_{BDC} - \theta_{Sp}$ of BDC and SpaCal as a function of the azimuthal angle ϕ before (a) and after (b) BDC alignment.

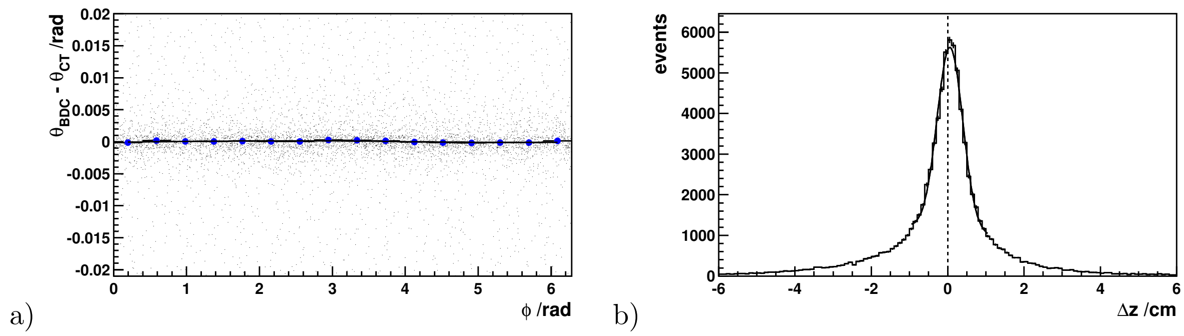

Figure 4.8: Difference in the polar angle measurements $\theta_{BDC} - \theta_{CT}$ of BDC and CT as a function of the azimuthal angle ϕ after the BDC alignment (a). BDC alignment as cross checked with the central tracker polar angle measurement.

$$\Delta z_{BDC} = z_{BDC}\left(1 - \frac{\tan\theta_{BDC}}{\tan\theta_{Sp}}\right), \tag{4.10}$$

where z_{BDC} is the z-position of the track segment in the BDC corresponding to the measurement of θ_{BDC}. As in the case of SpaCal, the peak position of the z_{BDC} distribution, see Figure 4.6 (b), corresponds to a z-shift of the BDC w.r.t. to the originally assumed z-position of the chamber. The alignment constants for both SpaCal and BDC are summarized in Table 4.3.

The polar angle measurement of the aligned BDC position was compared to that of the central tracker, in order to cross-check the alignment of the BDC. Figure 4.8 shows the difference in polar angle measurement by the BDC and by the central tracker (a) and a distribution of a quantity similar to that from eq. (4.10) but with the SpaCal polar angle θ_{Sp} exchanged to the central tracker θ_{CT} measurement (b). It can be seen that the alignment of the BDC, as obtained by aligning the BDC to SpaCal, is consistent with the central tracker position and approximately 1 mm correction is suggested and implemented in the final BDC alignment.

4.3.2 BST alignment

In order to benefit from the high spatial resolution of the backward silicon tracker BST an accurate internal and external alignment of the detector planes is essential. The minimization program *Millepede* [56] was applied in order to obtain a high quality alignment without biases. Millepede is a special package for least squares fits with a very large number of parameters. It takes advantage of the subdivision of parameters into two classes, *global* and *local* parameters. Global are those parameters common to the whole analysis while local parameters are present only in subsets of the data. For example, in an alignment application the detector alignment constants are the global parameters while parameters corresponding to tracks in each particular event are the local ones. The interest is only in optimal values of the global parameters. A practical limit for the number of global parameters in Millepede is between one thousand and ten thousand.

In the BST alignment 128 global parameters were used, corresponding to the radial positions of 128 detector wafers. A clear sample of BST high energy tracks was selected, using electrons in SpaCal with $E > 20\,\mathrm{GeV}$ which originate from a well measured central vertex and each track was within Millepede fitted by a straight line. Hence, for each event 128 global plus 2 local parameters were fitted in the χ^2 minimization procedure. The global parameters, due to the

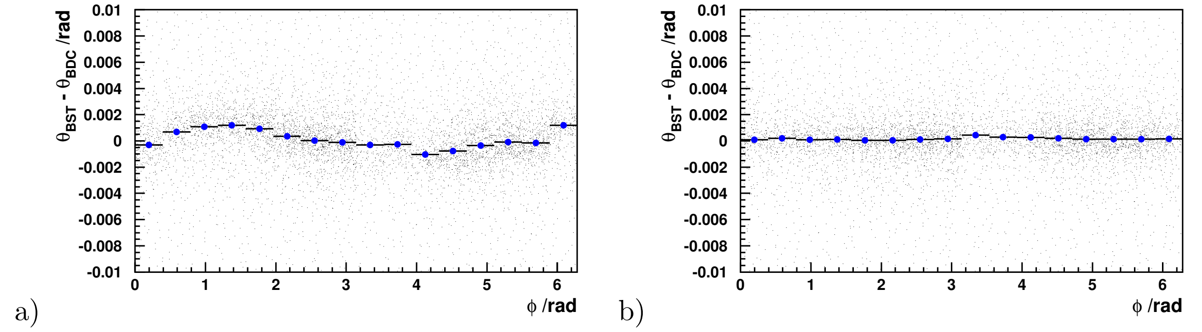

Figure 4.9: Difference $\theta_{BST} - \theta_{BDC}$ in the polar angle measurements of BST and BDC as a function of the azimuthal angle ϕ before (a) and after (b) the BST alignment (mb99 data).

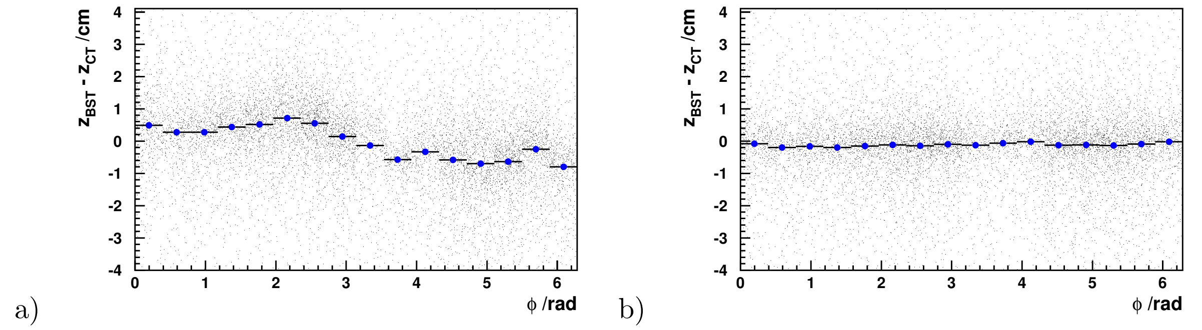

Figure 4.10: Difference $z_{BST} - z_{CT}$ in the interaction vertex z-coordinate measurement of BST and central tracker as a function of the azimuthal angle ϕ before (a) and after (b) the BST alignment (mb99 data).

special structure of the minimization matrix, were separated from the local ones. In order to correctly match the BST position into the H1 coordinate system, the positions of the CT vertex and of the BDC track segment were added to the fitted BST hits.

Figure 4.9 shows a comparison of the polar angle measurement by the BST and the BDC as a function of ϕ before (a) and after (b) application of the BST alignment. The comparison of the measurement of the interaction vertex z-position by the central tracker and by the BST is displayed in Figure 4.10 as a function of ϕ before (a) and after (b) the BST alignment. Finally, Figure 4.11 shows the effect of the BST alignment on the difference of the polar angle measurement by the BST and the BDC (a) and of the z-coordinate measurement by the BST

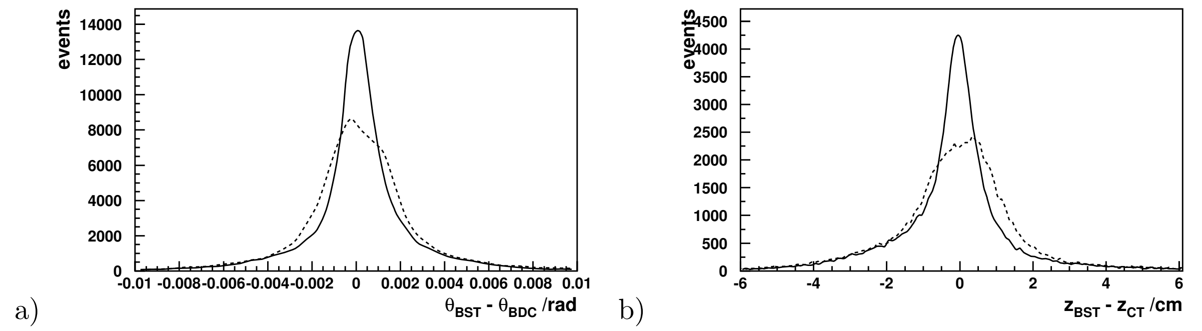

Figure 4.11: Difference $\theta_{BST} - \theta_{BDC}$ in the polar angle measurements (a) and difference $z_{BST} - z_{CT}$ in the interaction vertex z-coordinate measurement (b) both before (dashed line) and after (full line) application of the BST alignment (mb99 data).

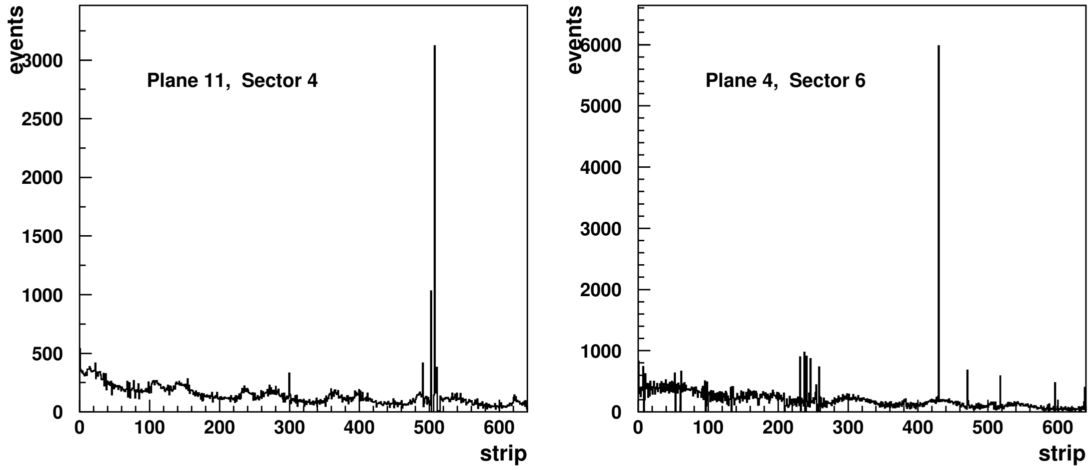

Figure 4.12: Distribution of hit rate as a function of strip number for two examples of BST wafers (mb99 data).

and the central tracker (b).

4.4 BST efficiencies

The measurement of the deep inelastic cross sections requires an accurate knowledge of the detector response which has to be implemented into the Monte Carlo simulation. In the presented analyzes the backward silicon tracker BST is the main detector component to measure the scattered electron polar angle as well as the interaction vertex position. Thus prior to physics analysis the BST response and efficiencies was studied in detail.

4.4.1 Noise treatment

The first step in order to understand the BST response has to deal with its noise. In general, there are two kinds of noise observed in the data

- **Noisy strips** - irregularities in the Si crystal structure cause a few strips to have a very high hit rate.
- **White noise** - thermal or electronic effects cause random noise hits, not correlated to real particles.

Examples of wafers with noisy strips are shown in Figure 4.12 which displays the distribution of hits on a wafer as a function of the strip number. Large peaks correspond to noisy strips while the rate of most of the strips is much lower.

The noisy strips for the whole BST are identified and enlisted in a table. For both mb99 and svtx00 data the number of noisy strips is about 1700 to be compared with the total number of $8 \times 16 \times 128 \times 5 = 81920$ BST channels, i.e. 2% of the strips are noisy. During the analysis any hits corresponding to those noisy strips are removed from the data. The Monte Carlo simulation

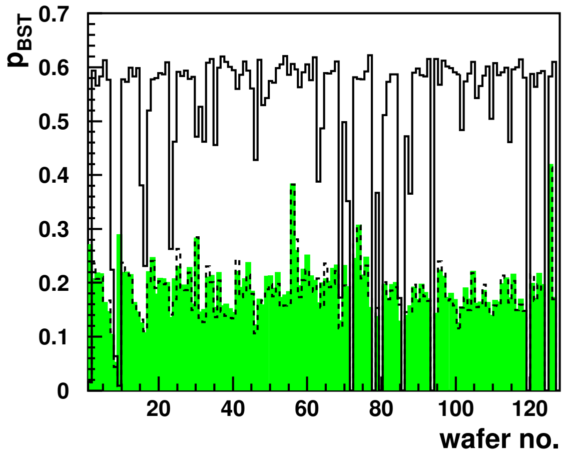

Figure 4.13: Probability p_{BST} to receive a random hit per wafer per event as a function of wafer number before (full line) and after (dashed line) correction of the noise contribution to Monte Carlo compared to the data noise level (filled histogram). Data from the mb99 data set were used.

is treated in exactly the same manner in order to ensure identical BST analysis procedure for both data and simulations.

After removal of the noisy strips the remaining random noise is estimated from BST ϕ-sectors without an electron signal. A sample of events is used with precisely one high energy electron candidate reconstructed in BST and SpaCal. The corresponding BST sector with the reconstructed track was removed from the BST and the remaining sectors were checked for the presence of hits. Since there should be no hits in these sector, if a hit was present it was treated as a white noise hit. It was found that the white noise in the real data is typically about 3 times smaller than that in the Monte Carlo simulation, see Figure 4.13 (a), where it is added to the reconstructed BST signal by hand. Due to a clear signature of random noise hits in the simulations, namely its signal to noise ratio is set to zero, majority of these noise hits was removed in the analysis code in order to reach the noise level of data. Figure 4.13 (b) shows the number of random hits per wafer per event, p_{BST}, as a function of the wafer number before and after correction of the noise contribution to Monte Carlo compared to the data noise level. On average the probability to receive a random hit on a wafer in one event is $\langle p_{BST} \rangle \approx 0.2$. It should be mentioned that the noise estimate is closely connected to BST wafer efficiencies, described in the next Sections 4.4.3 and 4.4.4. A couple of iterations of efficiency and noise estimates is necessary to reliably separate the influences of noise and efficiencies.

4.4.2 Hit treatment

The BST data acquisition and hit reconstruction was described in Section 3.4. In Monte Carlo simulations the BST is treated such that no detailed simulation of the BST electronics is done and hits are directly ‘created’ in the digitization of the particle’s passage through the wafers of the BST detector. Random noise hits, as described in the previous section, are added on top of the signal hits. This is a different situation as compared to the data, where a sliding window of 3-strip width is used to scan through the digitized amplitudes of the strips of a wafer in order to find a signal. For example, there can be two or more hits on one strip or neighbouring strips in the Monte Carlo simulations while only one hit is technically allowed in the data. Thus in both data and simulations the hits were checked for occurrence of hits on the same strips and also for

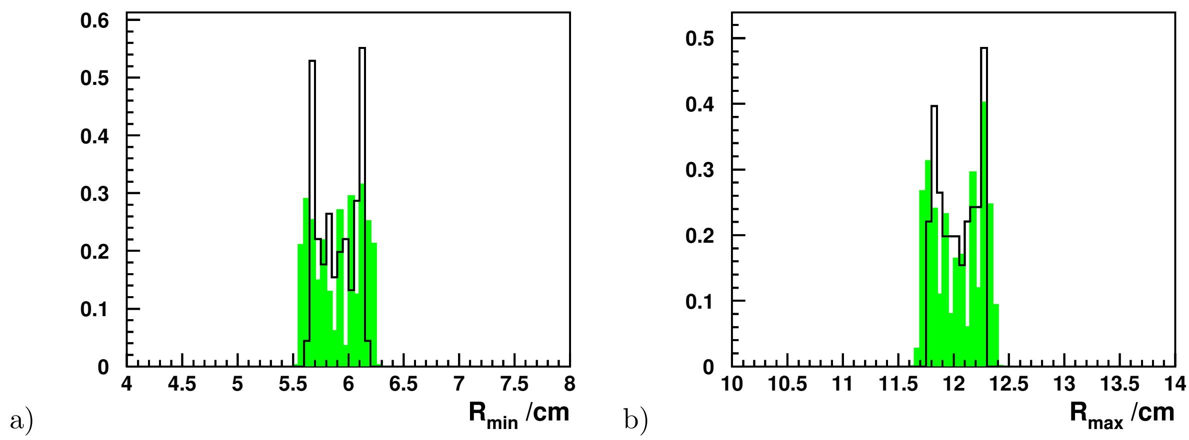

Figure 4.14: Distribution of the radial distance of the inner (a) and outer (b) BST wafer strips to the beam. Data from mb99 set (filled histogram) are compared to the Monte Carlo simulations (full line). Units on y-axis are arbitrary.

hits correlated with hits on neighbouring strips. Hits closer to each other than four strips were partially removed such that only one of them remained.

A further issue requiring particular care is the acceptance of the BST planes. Due to a difference in the beam positions in data and Monte Carlo a significant effect is coming from a different BST position in the beam coordinate system rather than from the alignment. Figure 4.14 depicts the radial distance from the beam of the inner, closest and the outer, furthest strips on BST wafers in the mb99 data set after alignment is performed. In order to minimize the edge effects the hits on edges of the BST wafers are removed if their radial distance to the beam R_{hit} is smaller than 6.5 cm or larger than 11.5 cm. In the svtx00 data set, in order to fully employ the BST acceptance at lowest values of Q^2, the radial acceptance of wafers was treated wafer-wise.

4.4.3 Internal efficiencies

A sample of events with a track in the BST acceptance linked to a SpaCal cluster with energy above 20 GeV is used to determine the internal efficiencies. This requirement corresponds to a clear electron signature. In order to suppress QED Compton events a good vertex reconstructed with the central tracker was required. The azimuthal angle ϕ_{Sp}, as measured by SpaCal, was used to externally determine which BST sector contains the track. In order to minimize effects of a wrongly assigned sector a strict cut on ϕ_{Sp} was done around the ϕ center of a given BST sector.

A single hit efficiency was defined with the requirement that a hit in the studied wafer has to be assigned to a track found in the BST. Due to the structure of the BST wafers, see Section 3.4, the internal efficiencies were studied for every single APC chip on a given wafer rather than for the wafer as a whole. This way particular inefficiencies related to damaged APC chips were identified and were not spoiling efficiencies of other APC chips of the wafer. Due to the treatment of noisy hits the efficiencies of BST wafers in Monte Carlo are not expected to be 100%. Hence, the same procedure was done for both data and Monte Carlo and the difference was used to correct efficiencies in simulations to the data level. The result is presented in Figure 4.15 which shows the internal efficiencies for a few wafers in the mb99 data.

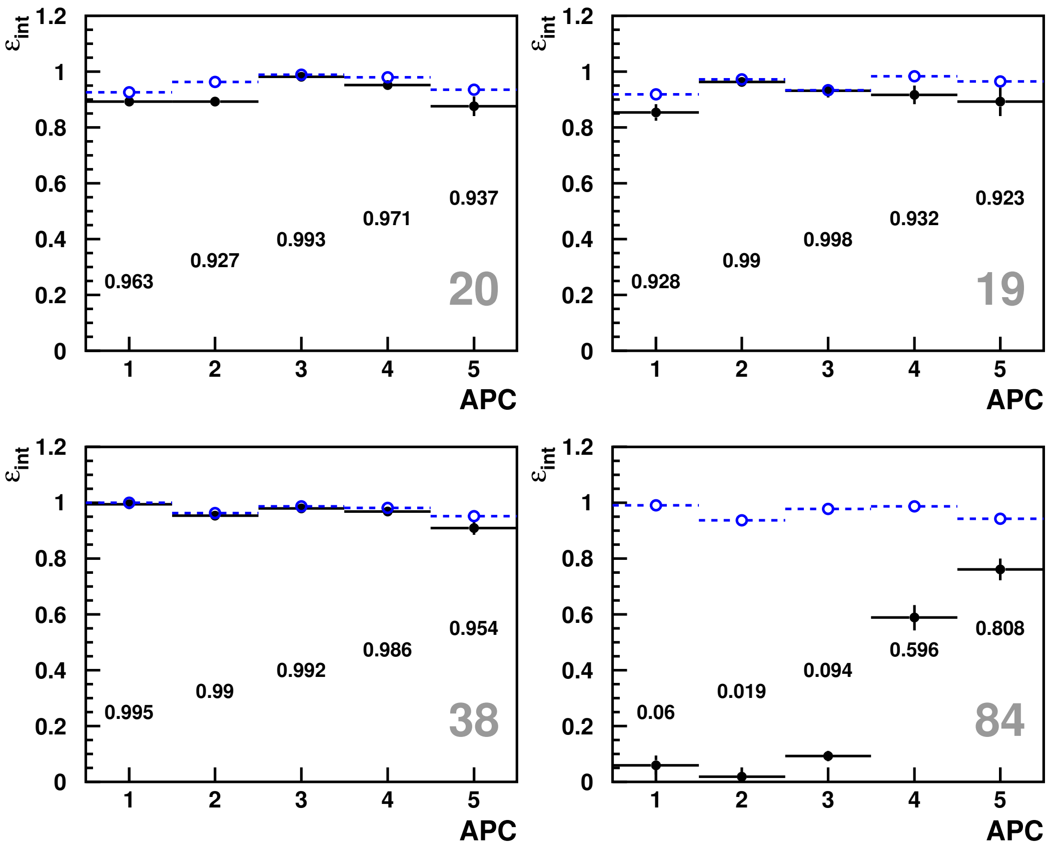

Figure 4.15: Internal efficiencies as a function of APC chip number on few example BST wafers. The number of the wafer is at the right-bottom corner of each plot. Data (closed points) and simulations (open points) are compared and their ratio (numbers) is used to downgrade the efficiencies of wafers in the Monte Carlo simulations.

4.4.4 Coherent losses

The external efficiency has possibly a component due to coherent losses. These may be due to readout failures affecting 'coherently' the whole detector or larger parts of it. Due to the high efficiency of the wafers, when a track is passing through 4 planes in BST the probability ϵ_{tr} to reconstruct such a track with at least two hits is almost 100% according to the binomial expression

$$\epsilon_{tr} = \epsilon^4 + 4\,\epsilon^2(1-\epsilon) + 6\,\epsilon^2(1-\epsilon)^2 \approx 100\,\%, \tag{4.11}$$

where ϵ is a single plane efficiency of a wafer and it is approximately 92% with large fluctuations on both sides. In order to check coherent losses in the readout chain, which lead to a loss of hits in the whole sector, events with an electron track passing through the first or second half of BST planes were selected. The splitting of the BST into two halves, each of four planes, is suggested by the BST construction. Events are selected based on a high energy SpaCal cluster and a very good central vertex. Furthermore, a track in the BDC chamber was required in combination with the vertex to determine accurately a track position in the BST.

Events were checked for the number of hits in the sector corresponding to the SpaCal cluster position. According to eq. (4.11) the expected external inefficiency in the case of no coherent

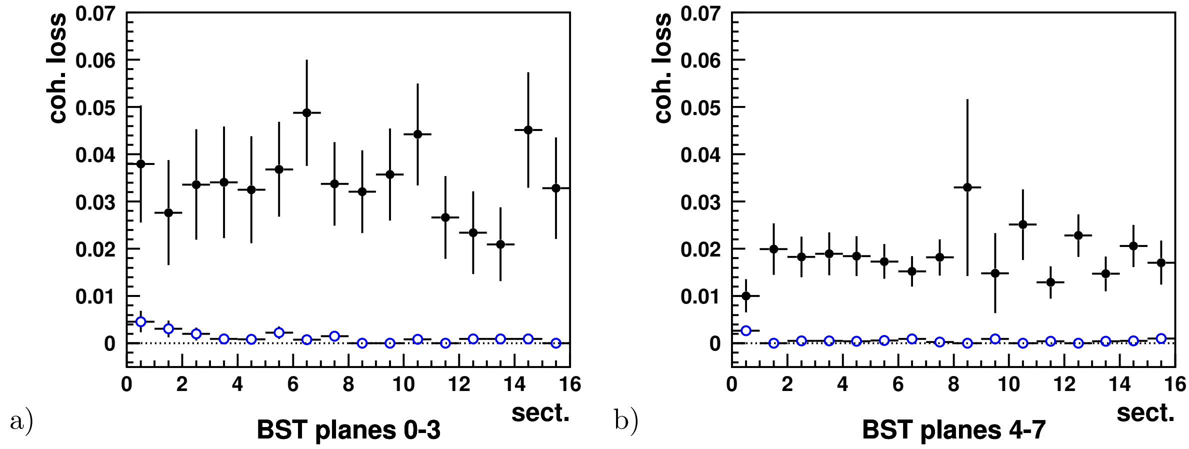

Figure 4.16: Coherent loss probability as a function of BST sector number for planes 0-3 (a) and 4-7 (b). Data (closed points) are compared to Monte Carlo simulations (open points), downgraded according to the internal efficiencies.

loss is almost zero. In the case that no hits were found the events were attributed to a coherent loss in the readout chain.

Figure 4.16 shows the result of the coherent loss analysis. The probability to have a coherent loss is plotted versus sector number for both halves of the BST separately. The Monte Carlo simulation (open points) demonstrates the validity of eq. (4.11) since simulations give an almost negligible effect of coherent losses except in sectors with lower wafer efficiencies. However, the effect of low efficient wafers does not exceed 0.5% and is taken into account by subtracting fake coherent losses in the simulations from the data estimates. In the presented analysis the simulated BST was sector-wise downgraded in order to reach the level of the coherent losses in the data. Overall, the coherent loss was reduced to 2-3% as compared to about 7% in the 1997 BST [49] due to improvements in the readout electronics and data acquisition.

4.5 Calibration

The reconstruction of the event kinematics is affected by the calibration accuracy of the energy of both the outgoing electron/positron and of the hadronic final state. As it can be seen from eq. (4.1) and eq. (4.5) the calibration enters directly the evaluation of kinematic variables via the E'_e and Σ quantities. Furthermore, the calibration affects the measurement indirectly due to the $E-p_z$ and P_t analysis cuts, see Section 4.7. Thus an accurate calibration of the electromagnetic as well as the hadronic energy measurement is vital for a precision cross section measurement. In this section, the calibration of the backward calorimeter SpaCal (Section 4.5.1) and of the Liquid Argon calorimeter (Section 4.5.2) is presented.

4.5.1 SpaCal energy calibration

The initial calibration of the SpaCal energy response is performed by employing a special LED system, which feeds light through fibers into light mixers and PMTs. Potential time-dependent instabilities of light output of each LED are monitored by photodiodes. Furthermore the calorimeter was re-calibrated using the so called *kinematic peak* [57] calibration method. For each cell a calibration constant is found in a number of iterations in order to separate the calibration effects arising from sharing a SpaCal cluster over few cells. This method is based on tuning the kinematic peak position in the way that it matches the position estimated from the Monte Carlo simulations. Since rather large statistics is needed in this method, it is usable mainly in the inner part of SpaCal, approximately for $R_{Sp} \lesssim 50cm$. The outer part is calibrated with cosmic muons.

In this analysis the calibration was re-done with the *double angle* method [58] which makes use of the fact that the event kinematics is overconstrained, see Section 4.1. This leads to the possibility to determine the scattered electron energy E'_e via the measurement of its polar angle θ_e and of the hadronic final state polar angle θ_h

$$E'_e = \frac{E_e(1 - y_{DA})}{\sin^2(\theta_e/2)}, \tag{4.12}$$

where the inelasticity y_{DA} in the double angle method is expressed as

$$y_{DA} = \frac{\tan(\theta_h/2)}{\tan(\theta_h/2) + \tan(\theta_e/2)}. \tag{4.13}$$

As can be seen from these relations, the double angle method does not depend directly on the SpaCal and LAr calibrations.

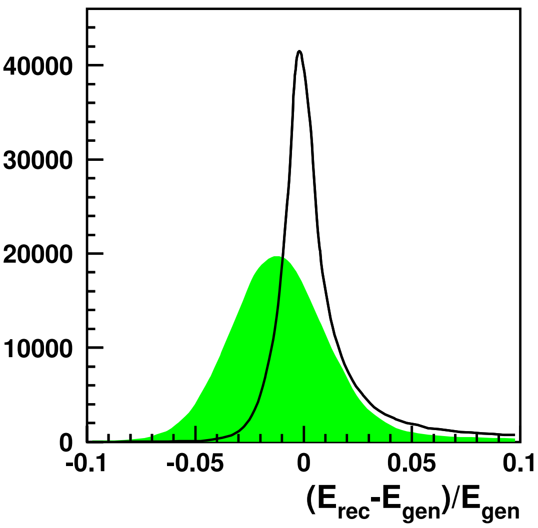

Figure 4.17: Relative reconstruction accuracy of the scattered electron energy as measured in SpaCal (filled area) and as obtained by the double angle method (full line) with respect to the energy on the generator level.

For the double angle calibration events with a high energy electron in the SpaCal and a well reconstructed central tracker vertex were selected. Furthermore a validation of the electron by the BST and the BDC was required. In order to select low y events a cut on $\theta_h < 80°$ was applied, corresponding to approximately $y < 0.15$. A possible influence of events at very low y, where the hadronic final state partially escapes detection in forward direction, was suppressed by a cut $\theta_h > 15°$. Events with wrongly reconstructed kinematics were removed by requiring $|y_h - y_{DA}|/(y_h + y_{DA}) < 0.2$.

Figure 4.17 shows a simulation of the scattered electron energy E_{rec} reconstructed with the double angle method and with the SpaCal calorimeter compared to the energy on the generator level E_{gen}. A bias on the level of 1% is observed in the case of the SpaCal reconstruction which is due to energy losses in the material on front of SpaCal. A visible tail towards higher values of the plotted ratio is due to showering [59] and the final state radiation. In these events a photon was radiated from the outgoing electron under a small angle, hence, both particles enter one cluster in the SpaCal while on the generator level the electron energy E_{gen} is calculated after the photon radiation.

The resolution of the double angle reconstruction method is about three times better than that of the SpaCal, and it thus was used to define the reference energy scale for the SpaCal calibration.

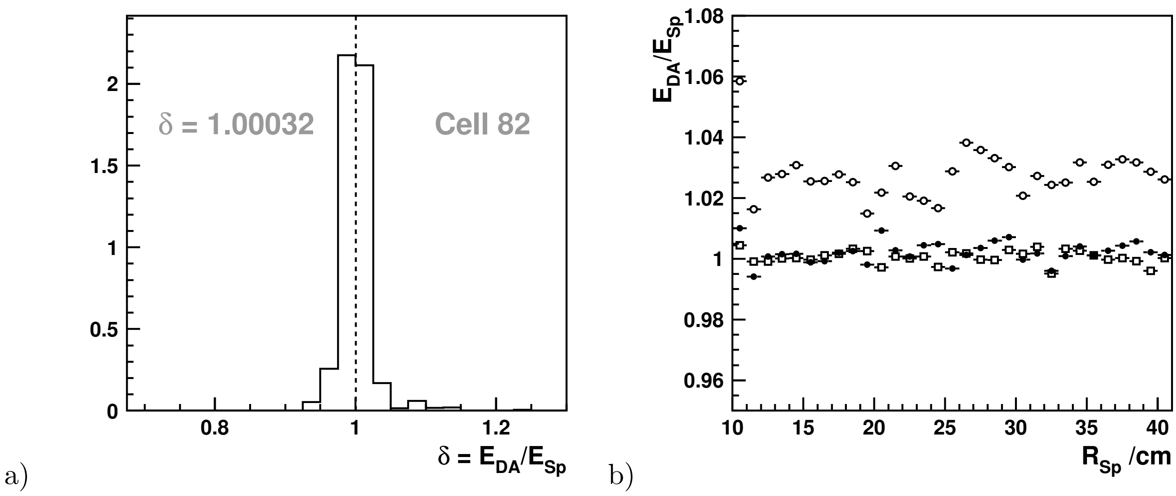

Figure 4.18: a) An example of the energy calibration pull δ distribution for a SpaCal cell. b) Distribution of the mean energy pull $\langle\delta\rangle$ as a function of the radius in the SpaCal plane R_{Sp}. Data from the svtx00 data set before (open points) and after (closed points) cell-by-cell calibration are compared to the cell-by-cell calibrated Monte Carlo simulations (open squares).

This was done by means of comparing the energy reconstructed in SpaCal, E_{Sp}, with that reconstructed by the double angle method E_{DA}. The energy calibration pull $\delta = E_{DA}/E_{Sp}$ is plotted as a function of various quantities in SpaCal, which are later used for correction of the cluster energy. In the following, the steps performed in this analysis are introduced and in more detail described.

Cell-by-cell correction

For each cell belonging to a particular cluster the pull δ of the whole cluster is plotted in a histogram, weighted by the energy fraction contribution of the cell to the cluster. An example distribution is shown in Figure 4.18 (a) for cell number 82. According to such distributions, for each cell i a mean pull δ^i is found by a robust mean estimator [60] and applied to reconstruct the re-calibrated cluster energy

$$E_{Sp} = \sum_i E_i \ . \ \delta^i, \tag{4.14}$$

where E_i is the energy of a cluster cell. In order to separate the influence of single cells in a cluster a number of iterations is needed. In every iteration step the result from the previous iteration is used and a further correction to cell energies is calculated. About five iterations are sufficient to obtain a stable result.

The result of this calibration step is shown in Figure 4.18 (b). The data before (open points) and after (closed points) cell-by-cell calibration are plotted as the pull δ dependence on the radius in the SpaCal plane R_{Sp} and compared to the result of the double angle calibration applied to the simulated events (open squares).

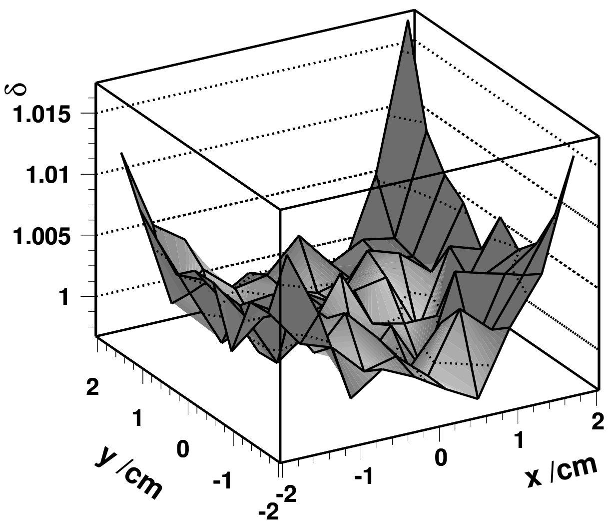

Figure 4.19: Distribution of the mean energy pull $\langle\delta\rangle$ as a function of the impact point position within the hottest cell in the cluster.

Inbox correction

Due to the SpaCal calorimeter construction there are small effects on the reconstructed energy expected from the position of the particle impact point within the calorimeter cells. If a particle hits a calorimeter cell in the middle, the energy is better contained than in the case of a hit in a cell corner, when part of the energy is lost in the dead material and not detected. In order to correct for this effect, the energy pull δ after cell-by-cell calibration is investigated as a function of the impact point position within the hottest cell in the cluster. Figure 4.19 shows a distribution of the mean pull δ as a function of the x and y coordinates in the hottest cell. In the middle of the cell the energy correction is small while in the case of a particle hitting the corner of the cell the energy correction can reach about 1%. The reconstructed cluster energy is corrected for this effect.

Crack correction

Except the dead material between single cells, the SpaCal is constructed from larger blocks of 16 cells, so called *supermodules*, see Section 3.3. Hence, there are further energy losses due to cracks between supermodules. These were corrected for as a function of $R_{box} = \max(|x_{Sp}|, |y_{Sp}|)$, where the coordinates correspond to the impact point position. Figure 4.20 (a) shows the mean energy pull δ as a function of R_{box}. Corrections are observed to reach level of 2% and are not fully described by Monte Carlo simulations. The crack corrections are used to correct the reconstructed cluster energy.

Radial correction

The radial correction is the last correction introduced in this analysis. It is motivated by the observed fluctuations of the energy pull δ as a function of the radius in the SpaCal plane $R_{Sp} = \sqrt{x_{Sp}^2 + y_{Sp}^2}$, see Figure 4.20 (b) open points. Hereafter the radial corrections are used to correct the reconstructed cluster energy.

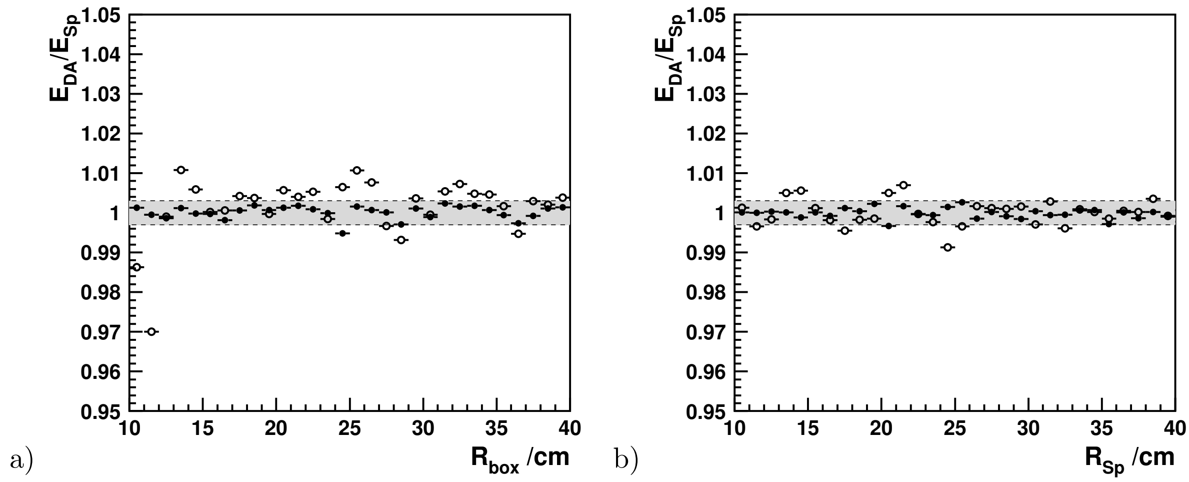

Figure 4.20: Distribution of the mean energy pull $\langle\delta\rangle$ as a function of $R_{box} = \max(|x_{Sp}|, |y_{Sp}|)$ (a) and $R_{Sp} = \sqrt{x_{Sp}^2 + y_{Sp}^2}$ (b) before (open points) and after (closed points) application of crack (a) and radial (b) corrections. Grey band around 1 corresponds to $\pm\,0.3\%$ error range. Data for svtx00 analysis are shown.

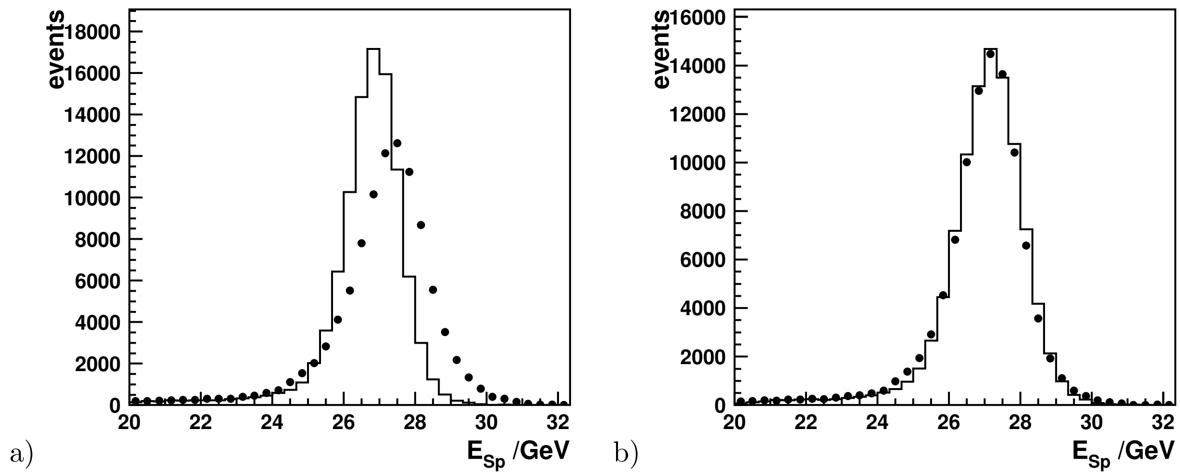

Figure 4.21: A comparison of cluster energy distributions before (a) and after (b) SpaCal calibration. In both cases data (closed points) are compared to Monte Carlo simulations (histogram), normalized by the histogram area.

Monte Carlo simulations were processed in the same way as the data. Energy spectra of data and simulations are compared before and after calibration in Figure 4.21. Variations of the energy scale do not exceed 0.3 %, this range is marked in Figure 4.20 by gray bands. Note that this high accuracy regards the relative scale difference between data and simulation which is the relevant quantity in this analysis. According to a study performed in [61], the error of the SpaCal energy measurement is larger at lower energies and reaches 2% at about $E = 7\,\mathrm{GeV}$ as is estimated from the energy-momentum comparison of SpaCal and BST, respectively. Hence, in the presented analysis the error value of 0.3% is used for the electron energy measurement error at 27 GeV and it is linearly extrapolated to 2% at 7 GeV.

4.5.2 Liquid Argon energy calibration

The kinematics reconstruction at large y, low x, is based on the hadronic final state measurement, as introduced in Section 4.1. The quantities of interest are

$$\Sigma = \sum_h E_h(1 - \cos\theta_h), \qquad P_t^{had} = \sum_h E_h \sin\theta_h, \tag{4.15}$$

where the summation is performed over all particles in the hadronic final state. In fact, both quantities Σ and P_t^{had} are simple energy sums weighted by a function of the corresponding polar angle.

The resolution of the LAr calorimeter is worse at low deposited energy, where fluctuations are increasing like $\sim 50\%/\sqrt{E}$ with decreasing energy. The central tracker system, on the contrary, has better energy resolution at low energies, due to a factor $\sim E$. Thus the kinematic reconstruction of the LAr may be improved by complementing the LAr hadronic final state measurement by the tracker response [52]. A special procedure (FSCOMB) was developed in order to separate the contributions to eq. (4.15) between the LAr calorimeter and the central tracking detectors. Reconstructed tracks with momenta $< 2\,\mathrm{GeV}$ are selected and extrapolated to LAr where they are linked to clusters. A track is used also in the case that its extrapolation does not reach LAr. Those calorimeter cells which were linked to tracks are masked in the evaluation of Σ and P_t^{had}, in order to avoid double-counting. As a result the hadronic energy scale is determined more accurately than in the case of the calorimetric measurement only, because of a special treatment of low momentum charged particles.

The LAr calorimeter has a certain level of noise, which must be subtracted in order not to bias the reconstruction. Finally the contribution to Σ and P_t^{had} of the SpaCal calorimeter is added to the LAr and central tracker contributions. Hence, Σ and P_t^{had} are factorized as follows

$$\Sigma = \Sigma^{LAr} + \Sigma^{Tr} + \Sigma^{Sp} - \Sigma^{noise}, \tag{4.16}$$
$$P_t^{had} = P_t^{LAr} + P_t^{Tr} + P_t^{Sp} - P_t^{noise}. \tag{4.17}$$

The final calibration was performed with both data and simulations using the so called *Lagrangian method* [49, 62]. Unlike in the case of SpaCal, the hadronic energy flow in LAr is collimated into jets and it is difficult to select single hadrons. Thus the calibration of LAr is done using global quantities, actually the transverse momenta P_t^{had} and P_t^e of the hadronic final state and electron, respectively, which in neutral current interactions are balanced. The calibration is based on the transverse momentum conservation assumption

$$P_t^{had} + P_t^e = \sum_h E_h \sin\theta_h + E_e \sin\theta_e = 0. \tag{4.18}$$

Due to the $\sin\theta$ suppression, the P_t balance method is rather insensitive to particle losses in the extreme forward and backward directions which are connected with the proton remnant jet and photon radiation.

The electron energy, entering the calibration, is supposed to be well calibrated and the electron polar angle is measured well in the backward trackers BST and BDC. Using the least square method, the following functional is subject to a minimization procedure

$$\mathcal{L} = \sum_{i=1}^{N} \frac{1}{\sigma_i^2} \left(P_t^e - (P_t^{Tr} + P_t^{Sp} - P_t^{noise}) - \sum_{j=1}^{M} \alpha_j \, E_j^i \, \sin\theta_j^i \right)^2 \tag{4.19}$$

and the calibration constants α_j are determined. In eq. (4.19) the first summation is over all events in the sample while the second one is performed over all contributing LAr cells. In this analysis the LAr was divided in eight wheels and each of them into eight octants as suggested by the calorimeter structure. Since the LAr has electromagnetic and hadronic part, the total number of calibrated cells was 128.

The noise term P_t^{noise} in eq. (4.19) is suppressed due to the fact that it is distributed isotropically over the azimuthal angle. The resolutions σ_i were for simplicity set constant.

The minimization requirement

$$\frac{\partial \mathcal{L}}{\partial \alpha_j} = 0 \tag{4.20}$$

defines a system of $k = 1..M$ linear equations

$$\sum_{i=1}^{N} P_{t,h}^{i\,k} \left(P_{t,e}^{i} - \alpha_k \sum_{j=1}^{M} P_{t,h}^{i\,j} \right) = 0, \tag{4.21}$$

where $P_{t,e}^i = P_t^e - (P_t^{Tr} + P_t^{Sp} - P_t^{noise})$ and $P_{t,h}^j = E_j \, \sin\theta_j$ of event i. The system of equations can be solved and the calibration constants α_k obtained using matrix techniques.

The P_t balance dependence on the transverse momenta measured from the electron side (P_t^e) for the data and Monte Carlo is presented in Figure 4.22. The same quantities but versus hadronic angle γ_h are shown in Figure 4.23. The data and simulations are found to be in agreement within 2% of accuracy. This value is used to determine systematic errors due to the hadronic scale uncertainty.

The decomposition of the y_h measurement by different detectors is shown in Figure 4.24. The data and simulations are found to be in a good agreement. Apart from the hadronic energy scale a large influence on y_h reconstruction is due to the LAr calorimeter noise. It is of a crucial importance for measurements at low values of $y_h \lesssim 0.05$. The fraction of noise contributing to y_h is depicted in Figure 4.24 (a,b) by open triangles. At values of $y \approx 0.003$ it contributes by about 50% while at high y the contribution is small. In this analysis the noise contribution is subtracted and the corresponding systematic error is determined via a comparison of the noise contribution in the data and simulations. This is shown in Figure 4.24 (c,d) where the ratio of the noise contribution in the data and simulations is plotted. Simulations are found to describe the noise level in the data to a precision better than 10%. This value is used to determine systematic errors of the cross section measurement due to the LAr noise contribution.

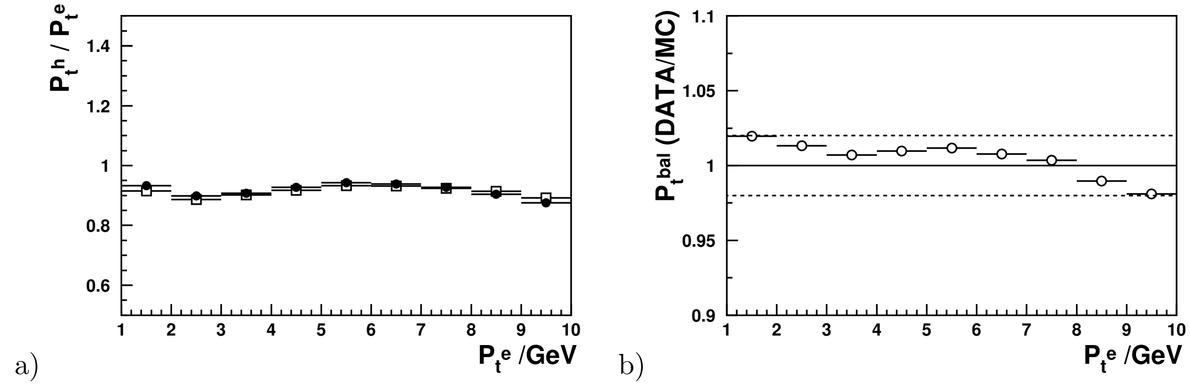

Figure 4.22: (a) Mean values of the P_t balance as a function of P_t^e for data (closed points) and Monte Carlo (open squares). (b) The corresponding ratio of the mean values between data and Monte Carlo. Dashed lines represent the systematical uncertainty of 2% for the LAr calorimeter calibration. The mb99 data are shown.

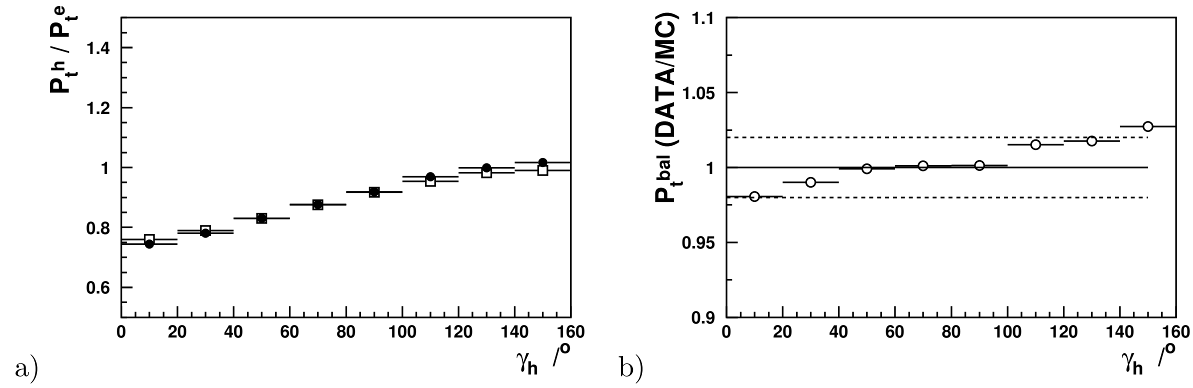

Figure 4.23: (a) Mean values of the P_t balance as a function of γ_h for data (closed points) and Monte Carlo (open squares). (b) The corresponding ratio of the mean values between data and Monte Carlo. Dashed lines represent the systematical uncertainty of 2% for the LAr calorimeter calibration. The mb99 data are shown.

4.6 Run selection

During data taking, the stream of events is split into so called luminosity runs. A run is a set of events collected by the experiment under similar conditions. The run size can vary and is not fixed. Each run has an integrated luminosity value. In general, various important database information is treated as being run dependent and it is stored separately for different runs.

The first step in the analysis is a preselection of the data sample on a run by run basis. This step ensures that the detector was in a stable condition and periods with hardware problems are not downgrading the quality of the measurement. The following criteria were applied:

- **Hardware status** - All relevant readout branches must be included in the detector readout and corresponding detector components must be operational. A run is rejected if at least one HV alarm bit is on for more than 20 % of the integrated luminosity recorded in this run. The luminosity is corrected accordingly. The following subdetectors were required to have nominal HV status: SpaCal, BST, LAr, BDC, central trackers and the luminosity system.

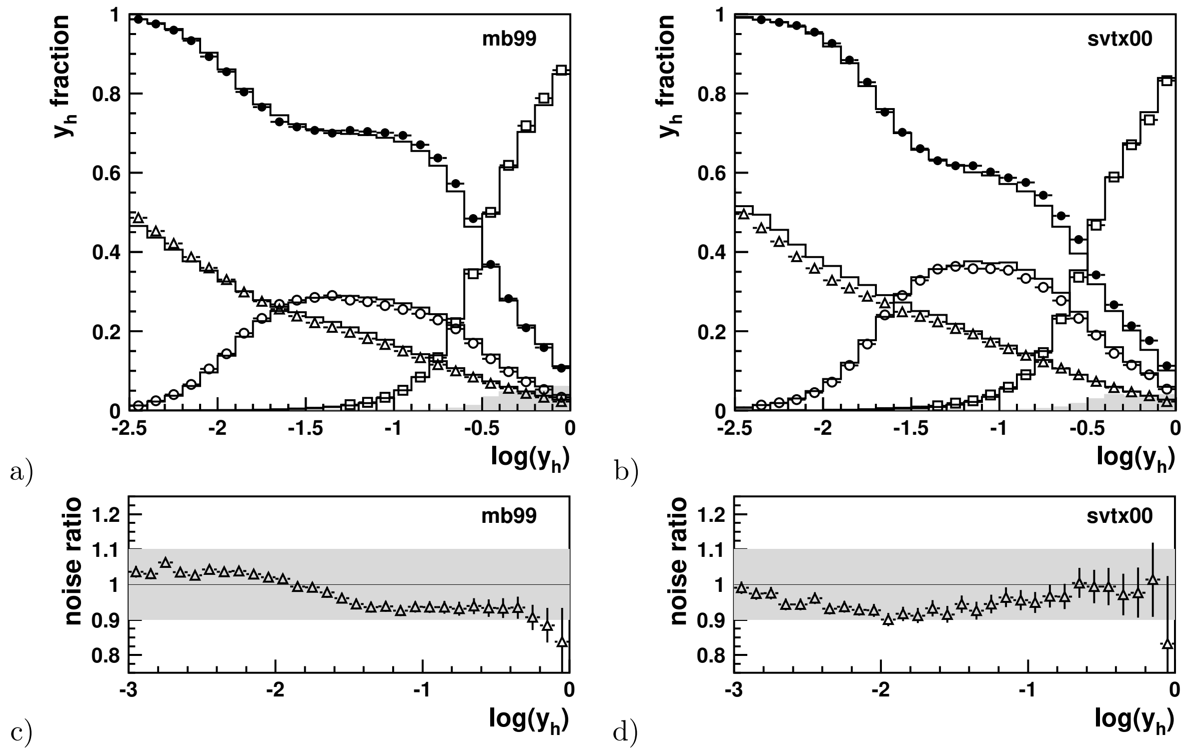

Figure 4.24: Experimental distributions of the fraction of y_h contributed by tracks (open circles), LAr calorimeter (closed circles) and SpaCal (open boxes) for the mb99 (a) and svtx00 (b) data sets. The histograms correspond to the Monte Carlo simulations. The fraction of subtracted noise is displayed by open triangles and corresponding ratio between data and Monte Carlo is shown for the mb99 (c) and svtx00 (d) data sets. Grey bands mark the systematical uncertainty of 10% for the noise description.

- **Large prescales of triggers** - In order to avoid runs with large trigger prescales, the prescale factors were limited to 8 for all subtriggers used. In fact, almost all runs fulfil this criterium.
- **BST performance** - Runs with downgraded performance of BST were removed from the sample and only runs with stable and understood response were considered. More details on the BST treatment were presented in Section 4.4.
- **Run quality** - Each run is classified according to the operation status of the main detector components as *good*, *medium* and *poor*. In runs with run quality poor an obvious hardware or software problem was found and, consequently, these are rejected from the analysis sample.

4.7 Event selection

In the presented analyzes the event selection is based mainly on the SpaCal calorimeter and the BST tracker. The number of selection cuts is kept as low as possible in order to keep low bias of data. Signal selection and background rejection of the imposed cuts is studied and aimed to act in the same manner on both data and simulations.

The focus on the electron reconstruction with BST makes the analysis truly inclusive since it does not rely on the hadronic final state properties. Events are detected and reconstructed even if the vertex is not found by the central tracker e.g. in some diffractive DIS processes.

Main selection cuts			
Cut	mb99	svtx00	mb99, high y
e energy cut	$6.9 < E_e < 32\,\mathrm{GeV}$		$4 < E_e < 15\,\mathrm{GeV}$
BST vertex	$\lvert z_v - 5\rvert < 30\,\mathrm{cm}$	$\lvert z_v - 70\rvert < 30\,\mathrm{cm}$	$\lvert z_v - 5\rvert < 30\,\mathrm{cm}$
Cluster radius	$< 4\,\mathrm{cm}$		
$E - p_z$ cut	$> 35\,\mathrm{GeV}$		$> 40\,\mathrm{GeV}$
P_t balance	> 0.3 for $E_e > 20\,\mathrm{GeV}$		-

Complementary cuts			
Fiducial cut	ineff. areas cut $\wedge\ R_{Sp} > 10\,\mathrm{cm}$		$\wedge\ R_{Sp} > 12\,\mathrm{cm}$
central tracker	-		$\exists$ vertex $\wedge\ N_{tracks} > 0$
Hadronic fraction	$< 15\,\%$		
Veto energy	$< 1\,\mathrm{GeV}$		

Table 4.4: Summary of the DIS selection cuts used in presented analyzes.

The prime task of the event selection is to identify the scattered electron. In the main part of the analysis, namely for inelasticity $y < 0.5$, the electron energy is higher than that of the hadronic jet. Thus a SpaCal cluster with maximum deposited energy, so called *leading cluster*, is considered to be the electron candidate. Also for higher inelasticity values the leading cluster still remains a reliable candidate. However, for largest values of inelasticity y in mb99 analysis based on the subtrigger s9 except the leading cluster as well the other SpaCal clusters were considered in the case that the leading one have not passed the electron selection criteria. This treatment of electron candidates is referred to as *energy ordering*. Another possibility is P_t ordering where the candidates are ordered according to their P_t whilst the candidate with largest P_t is considered to be the scattered electron. This ordering is consistent with energy ordering within 1% of the measured cross section [49].

At high cluster energies[4] the signal in SpaCal is almost background free and the event selection is focused on the kinematics reconstruction rather than on the background suppression. At low energies, corresponding to high y, the photoproduction contributes to the signal background. Hence, the background suppression and the electron identification are tasks of great importance.

For both data samples the event selection cuts are almost identical, see Table 4.4. A SpaCal electron candidate cluster is the basis of the event selection. For the bulk analysis, based on subtriggers s0 and s3, the electron candidate energy is required to be in the region where s0 has almost 100 % efficiency, i.e. above approximately 6.9 GeV. For the high y analysis, based on the subtrigger s9, this cut is lowered to 4 GeV and s9 inefficiency is corrected accordingly. In the next step, a track in BST corresponding to that cluster is required. This requirement significantly suppresses the photoproduction background, which is mostly due to photons from π decays misidentified as scattered electrons in SpaCal. Furthermore, the BST vertex is required to be reconstructed within a certain region around the mean vertex position. This requirement removes the contribution of the proton beam satellite bunches at larger values of z_v, which is not simulated in Monte Carlo simulations. The mean shift of the forward (backward) satellite bunch is roughly 70 cm (-70 cm) compared to the main bunch. Hence, a cut tolerance of ± 30 cm w.r.t. the mean position is chosen which is safe for satellite bunch rejection and corresponds to roughly 3σ of DIS signal events.

[4] At energies above approximately 15 GeV corresponding to $y \approx 0.5$ at low Q^2.

The photoproduction background is further suppressed by the cut on the SpaCal cluster radius and on total $E - p_z$. The latter cut is essentially requirement that all of kinematically relevant outgoing particles are detected in the H1 detector. Hence, when an electron in the photoproduction events escapes detection, the value of $E - p_z$ of such an event is significantly lower than the expected value $2 \times E_e^{beam}$. In the svtx00 data analysis this cut is relaxed if the sigma method is used in the event kinematics reconstruction. This is done to increase statistics of ISR events dominating at $Q^2 < 1\,\mathrm{GeV}^2$ and low y.

At values of very low y, high x, the hadronic final state particles can partially be scattered below the forward modules of the LAr calorimeter and escape detection. In the low Q^2 kinematic region of the presented analysis the losses are especially pronounced at low photon-proton system mass squared $W^2 = Q^2\,x/(1-x) + M_p^2$, where the resonance region is accessed. This contribution is missing in the DJANGO simulations, where events of $W < 5\,\mathrm{GeV}$ are not generated. Whilst it is possible to add HERWIG simulations to DJANGO in order to describe the region of low W^2, in this analysis it is preferred to control the hadronic final state and its losses via a cut on the balance of transverse momenta of the hadronic final state and the scattered electron, $\delta_{bal} = P_t^{had}/P_t^{el}$. It was shown in [49] that cut on $\delta_{bal} > 0.3$ for electron candidates with $E'_e > 20\,\mathrm{GeV}$ removes more than 99% of mentioned low W events.

An electron candidate track in the BST is extrapolated to the SpaCal. Fiducial cuts are applied for events with electron candidate clusters in SpaCal cells with low efficiency, bad response and also at the edge of acceptance. In both data and simulations the fiducial cuts are performed in the beam coordinate system in order to ensure identical kinematic phase-space coverage.

The list of cuts is enclosed by the cut on the hadronic fraction of the electron candidate energy, to suppress contributions of hadrons misidentified as electrons, and by the cut on energy in the veto layer of SpaCal. The latter cut is used to suppress losses of energy deposits at very high polar angles, close to the edge of SpaCal acceptance at low radii.

4.8 PHOJET normalisation

A large background contribution at highest values of inelasticity y, low scattered electron energies, is due to the photoproduction processes where a quasi-real photon is exchanged between the electron and the proton. Its four momentum transfer squared Q^2 is extremely low, hence, the scattered electron polar angle is close to the incident one and the electron is usually lost in the beam pipe. However, particles of the hadronic final state can be detected in SpaCal and may fake a low energetic electron signal due to the very high rate of those events. A major part of this background are photons from π^0 decays which can be well suppressed by a track requirement in BST, as it was mentioned in the event selection section. The remaining photoproduction background consists of converted photons which give a signal in BST and of charged hadrons. In this analysis this background is estimated using PHOJET simulations and statistically subtracted from the data. Thus an understanding of the photoproduction background and of the PHOJET luminosity is an important task for the high y analysis.

The scattered electron from a photoproduction event can be eventually detected in the electron tagger (ET) calorimeter, see Section 3.2. ET acceptance, however, is limited and only a small fraction of events with certain kinematics can be detected. The electron tagger acceptance as a function of the inelasticity y is depicted in Figure 4.25 (a) and it is calculated on a run-dependent basis. In the H1SIM simulation code the electron tagger is not included. Hence, the

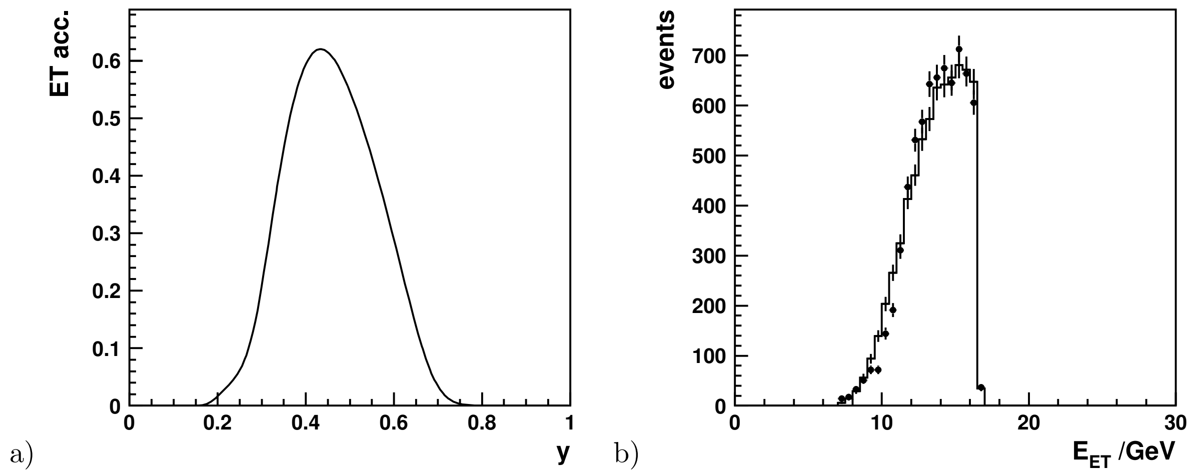

Figure 4.25: Electron tagger acceptance as a function of inelasticity y (a) and a distribution of the scattered electron energy as measured by the electron tagger (b) for the mb99 data set (closed points) and PHOJET simulation (full line).

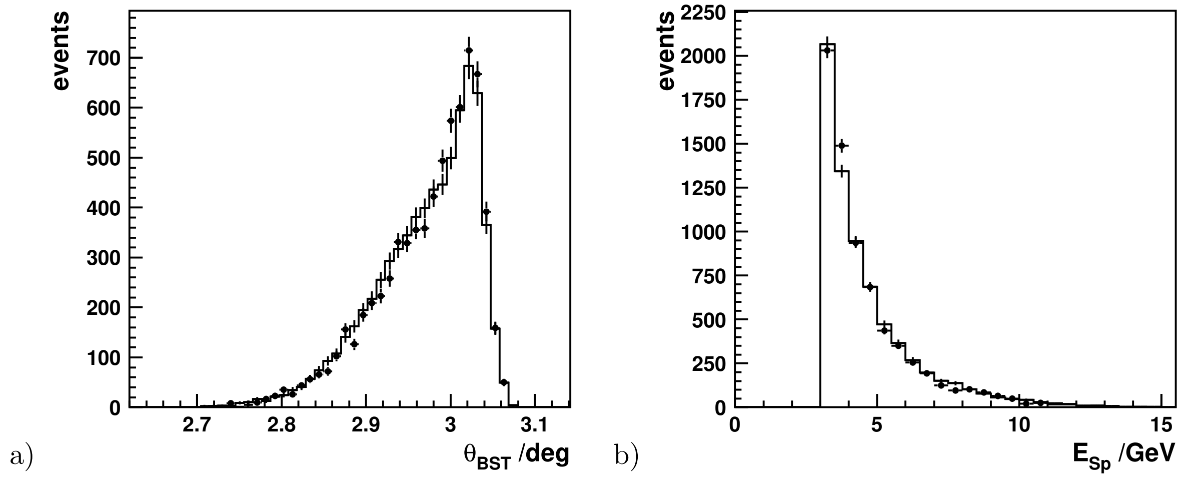

Figure 4.26: A distribution of the polar angle measurement (a) and SpaCal energy deposit (b) of misidentified electron candidate in the tagged events sample (mb99 data set).

acceptance function is used instead to re-weight PHOJET events according to the inelasticity on the generator level. The run-dependence is simulated by splitting the whole PHOJET sample into sets corresponding to single runs in the data, as defined by their luminosity.

A sample of so called *tagged events* was used to cross-check the PHOJET simulations. The event selection is identical to that of DIS high-y analysis, except the $E - p_z$ cut which is relaxed. This strategy is used in order to keep the photoproduction analysis close to the DIS analysis. The energy in the electron tagger is required to be greater than 7 GeV, in the region of good electromagnetic shower containment. The energy deposit in the photon tagger (PT) is required not to exceed 2 GeV.

Figure 4.25 (b) shows a comparison of the scattered electron energy measured in the electron tagger for data and PHOJET simulations. Figure 4.26 compares distributions of the misidentified electron candidate in SpaCal, i.e. of the background to DIS measurement. The distributions are in good agreement.

The PHOJET luminosity is normalized onto the data via integrals I_{Data} and I_{PHOJET} over the

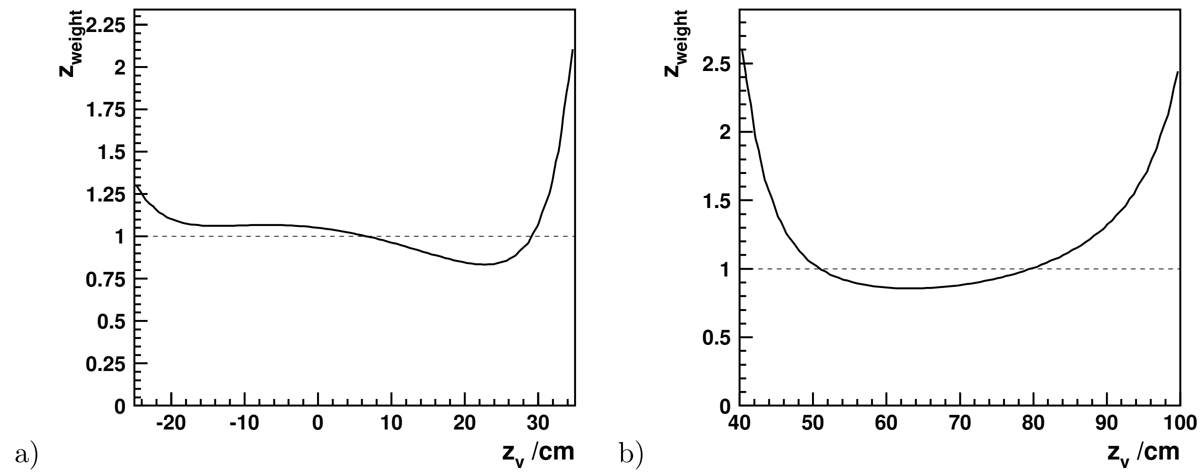

Figure 4.27: Re-weighting functions of interaction vertex z-position for DJANGO simulations of mb99 (a) and svtx00 (b) data sets.

tagger energy E_{ET} distributions of data and simulations, respectively. It is expressed as

$$\mathcal{L}_{PHOJET} = \frac{I_{PHOJET}}{I_{Data}} \cdot \mathcal{L}_{Data}, \tag{4.22}$$

where $\mathcal{L}_{Data}$ is the luminosity of the data.

4.9 DJANGO-final adjustments

The DJANGO simulations were performed with given structure functions which do not necessarily describe the data. Namely for the mb99 and svtx00 samples proton structure functions F_2 from GRV and MRST leading order fits[5] were used, respectively. In both cases the longitudinal structure function was set to zero during the event generation. These functions were selected due to their reasonable behaviour over the whole phase-space of the measured kinematic range. In the analysis code events were re-weighted according to the preferred structure functions by a weight

$$w_{\sigma_r} = \frac{\sigma_r^{an}(Q^2, x)}{\sigma_r^{gen}(Q^2, x)}, \tag{4.23}$$

where Q^2 and x are values used on the generator level and calculated at the hadronic vertex. Here σ_r^{gen} and σ_r^{an} are reduced cross sections for the structure function sets on the generator level and in the analysis, respectively.

Besides the cross section re-weighting the events were re-weighted according to their interaction z-vertex position. The z_v distribution in the Monte Carlo simulations is a gaussian distribution with certain mean position and width. Since in the data the vertex distribution slightly differs from simulations a procedure, called *vertex re-weighting*, is introduced in order to re-weight simulated events according to their vertex position and thus match the vertex distribution in

[5]The corresponding PDFLIB set numbers are 5004 and 3075.

$Q^2\,[\mathrm{GeV}^2] =$	0.3162, 0.4217, 0.5623, 0.7499, 1.00, 1.334, 1.778 2.371, 3.162, 4.217, 5.623, 7.499, 10.00, 13.34
$y_{mb99}\ =$	.0010, 0.0024, 0.0061, 0.015, 0.028, 0.050, 0.090 0.16, 0.29, 0.53, 0.67, 0.79, 0.89
$y_{svtx00}\ =$	0.00078, 0.0061, 0.015, 0.038, 0.090 0.16, 0.29, 0.53, 0.67, 0.79, 0.89
$y^{ISR}_{svtx00}\ =$	0.00078, 0.0061 0.038, 0.16, 0.53, 0.67, 0.79, 0.89

Table 4.5: Values of bin boundaries in presented analysis.

the data. Knowledge of the beam parameters is essential because it directly enters the polar angle measurement and thus the acceptance of the detector. Although the beam parameters vary for each luminosity fill of HERA, since both data sets were taken in short time periods with smooth running, the correction is applied for all runs of a particular data set in the same manner.

The event selection for the vertex position analysis is based on SpaCal inclusive triggers s0 and s3. Clusters are pre-selected with energies $E'_e > 15\,\mathrm{GeV}$, corresponding to low y. At least one track and a reconstructed vertex are required in the central tracker in a polar angle region $160^\circ < \theta_e < 175.6^\circ$ for the mb99 sample and $165^\circ < \theta_e < 177^\circ$ for svtx00. This requirement is due to minimization of SpaCal acceptance effects on the vertex distribution measurement. A Gaussian fit is performed to the vertex distribution for both data and simulations and a re-weighting function for simulated events is calculated according to

$$w_z = \frac{G(z_v^{data}, \sigma_z^{data})}{G(z_v^{MC}, \sigma_z^{MC})}, \tag{4.24}$$

where G stands for the normalized Gaussian distribution, z_v and σ_z are parameters from the fit to the data and simulations. Figure 4.27 shows the re-weighting function for the mb99 (a) and svtx00 (b) data samples.

4.10 Cross section measurement

The cross section determination in the presented analysis was performed in bins of Q^2 and y. The reason for selecting the inelasticity y instead of Bjorken x variable is that it is more appropriate for the high y region. Furthermore, many detector effects are y related, for example the vertex reconstruction efficiency, resolution etc.

Bin boundaries are enlisted in Table 4.5 and corresponding central values in Table 4.6. For svtx00 data set the y bins are wider than those of the mb99 data. This is due to the worsened hadronic reconstruction in the former data set and due to smaller statistics of the whole sample. Furthermore, bins at medium y and $Q^2 < 1\,\mathrm{GeV}^2$, which are dominated by initial state radiation (ISR) events, were enlarged due to a lower reconstruction resolution of these events and in order

$Q^2\,[\mathrm{GeV}^2] =$	0.35, 0.5, 0.65, 0.85, 1.5, 2.0, 2.5 3.5, 5.0, 6.5, 8.5, 12.0
$y_{mb99}\ =$	0.0017, 0.0043, 0.011, 0.022, 0.039, 0.070 0.13, 0.23, 0.41, 0.60, 0.73, 0.84
$y_{svtx00}\ =$	0.002, 0.01, 0.024, 0.060 0.13, 0.23, 0.41, 0.60, 0.73, 0.84
$y^{ISR}_{svtx00}\ =$	0.002 0.015, 0.09, 0.29, 0.60, 0.73, 0.84

Table 4.6: Values of bin centers in presented analysis.

to increase the statistics per y interval. Hereafter the bins corresponding to ISR bin boundaries are referred to as ISR bins.

The double differential reduced cross section in a particular bin is calculated as follows

$$\frac{d^2\sigma_r}{dx\,dQ^2} = \frac{N^{data} - N^{\gamma p}}{\mathcal{L}^{data}}\ \frac{1}{A}\ \frac{1}{1+\delta}\ \beta_{BC}, \tag{4.25}$$

where N^{data} and $N^{\gamma p}$ is the number of measured and background events, respectively, which passed the DIS selection criteria. Luminosity of the data corrected for the satellite bunch contribution is denoted as $\mathcal{L}^{data}$. The acceptance A is defined as $A = N^{rec}/N^{gen}$, i.e. as a ratio of the number of reconstructed and generated events in the bin. Radiative corrections are represented by the quantity $\delta = \sigma_{rad}/\sigma_{Born} - 1$, where σ_{rad} and σ_{Born} stands for bin integrated full and Born cross section, respectively. Bin center corrections are accounted for by a factor β_{BC}, which is defined as

$$\beta_{BC} = \frac{d^2\sigma_r^{MC}}{dx\,dQ^2}\ \frac{1}{\sigma_{Born}}. \tag{4.26}$$

Quantities A, δ and β_{BC} are calculated using Monte Carlo simulations. The above formula (4.25) becomes more simple in the case that radiative corrections are already included in the simulations, then $N^{gen} = \sigma_{rad}\,\mathcal{L}^{MC}$ and denoting $N^{MC} = N^{rec}$, for clarity, one obtains

$$\frac{1}{A}\ \frac{1}{1+\delta}\ \beta_{BC} = \frac{\sigma_{rad}\,\mathcal{L}^{MC}}{N^{MC}}\ \frac{\sigma_{Born}}{\sigma_{rad}}\ \frac{d^2\sigma_r^{MC}}{dx\,dQ^2}\ \frac{1}{\sigma_{Born}} = \frac{\mathcal{L}^{MC}}{N^{MC}}\ \frac{d^2\sigma_r^{MC}}{dx\,dQ^2}. \tag{4.27}$$

Hence, eq. (4.25) can be re-written into the so called *Monte Carlo* method form

$$\frac{d^2\sigma_r}{dx\,dQ^2} = \frac{N^{data} - N^{\gamma p}}{N^{MC}}\ \frac{\mathcal{L}^{MC}}{\mathcal{L}^{data}}\ \frac{d^2\sigma_r^{MC}}{dx\,dQ^2}, \tag{4.28}$$

which significantly simplifies the cross section calculation. In fact, the measured cross section is proportional to the one used in Monte Carlo simulations and re-weighted by the luminosity normalized ratio of the number of DIS events in a particular bin in data and simulations.

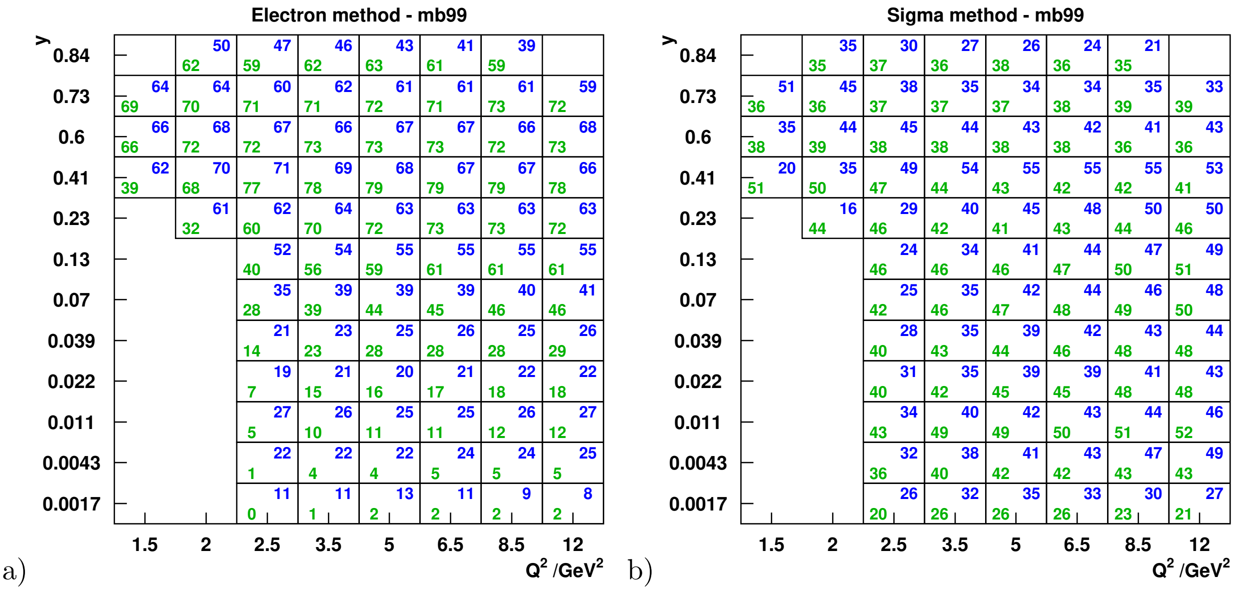

Figure 4.28: Purities (upper right corner) and stabilities (lower left corner) and in bins of Q^2 and y for kinematics reconstruction with electron (a) and sigma (b) method. Analysis of the mb99 data set. Values are in percent.

4.10.1 Bin selection

The cross section measurement is performed in intervals of Q^2 and y as introduced in the previous section. For each of these bins *purity* and *stability* quantities are defined as

$$purity = \frac{N^{rec.\&gen.}}{N^{rec.}} \qquad\qquad stability = \frac{N^{rec.\&gen.}}{N^{gen.}}, \tag{4.29}$$

where $N^{rec.}$ and $N^{gen.}$ are numbers of events reconstructed and generated, respectively, in a particular bin. The number of events which at the same time are reconstructed and generated is denoted as $N^{rec.\&gen.}$. The purity controls the contamination of migrating events from adjacent bins into a particular measurement bin. The stability corresponds to event migration out of bins where they actually belong to. The values of both quantities are by definition bounded to interval $\langle 0, 1 \rangle$.

The purities and stabilities for the electron method used in the event reconstruction are given in Figure 4.28 (a) and 4.29 (a) for mb99 and svtx00, respectively. The values of both quantities are high, about 60-70%, in the high y region. Due to the $1/y$ factor in the electron method the resolution of y_e rapidly degrades what causes a decrease of purities and stabilities at low y.

The sigma method has at high y worse resolution than the electron method. Hence purities and stabilities are worse (see Figure 4.28 (a) and 4.29 (b)). However, it covers the whole phase-space with approximately comparable values of purities and stabilities of about 30-50%. Thus this method is preferred at low y but as well it may be used at higher values of y. Only bins with purity exceeding 30% are considered further in this analysis.

In the ISR bins, which differ from the nominal bins shown in Figures 4.28 and 4.29, the purities are on the level of about 40% for all bins considered. These are bins at $Q^2 < 1\,\mathrm{GeV}^2$ and at $8.10^{-4} < y < 0.16$.

The following bin selection strategy was used in order to exploit fully the available data potential:

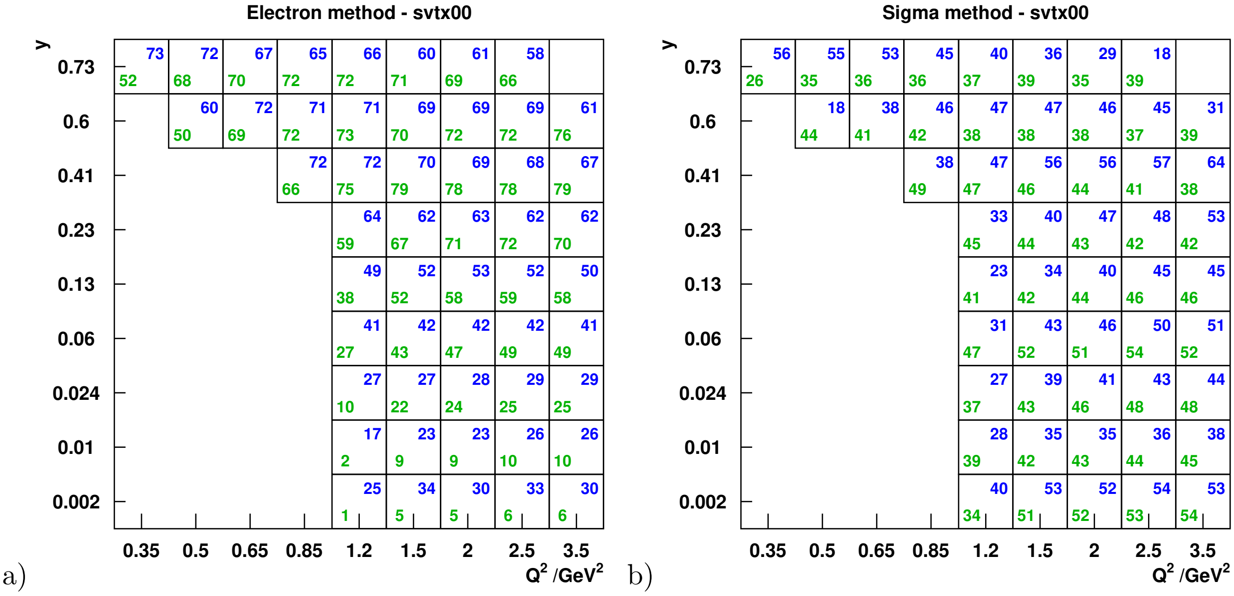

Figure 4.29: Purities (upper right corner) and stabilities (lower left corner) in bins of Q^2 and y for kinematics reconstruction with electron (a) and sigma (b) method. Analysis of the svtx00 data set. Values are in percent.

- In both mb99 and svtx00 data sets the main part of this analysis is based on s0 and s3 subtriggers and is limited to the range of safe BST and SpaCal acceptance. At high y events are preferably reconstructed with the electron method and at low y with the sigma method.
- The analysis based on the s9 trigger in the mb99 data set is used to measure only in the highest y bin. Lower y bins are better covered by s0 and s3 subtriggers. Only the electron method is employed in this case.
- In the svtx00 data set the bins on the edge of BST and SpaCal acceptance are measured with the sigma method if purities and stabilities of these bins are acceptable. The sigma method is preferred rather than the electron method to minimize edge effects and to avoid acceptance cuts in these bins.
- A low Q^2 ($< 1\,\mathrm{GeV}^2$) medium and low y is measured with the sigma method by making use of the ISR events.

The latter part of the analysis employs ISR events in a novel way. Usually radiative events are efficiently removed by the $E - p_z$ cut. Here, however, they are retained and thus an unexplored region of phase space becomes accessible. The analysis is technically identical to the non-radiative measurement and the same analysis code is used. The difference is in the evaluation of the Bjorken x from Q^2_Σ and y_Σ via a different center of mass energy s due to the photon emission. The mean incoming electron energy is obtained bin-wise as the arithmetical mean of

$$E_e = \frac{\Sigma + E'_e(1 - \cos\theta_e)}{2}. \tag{4.30}$$

This formula is valid for both non-radiative and ISR events with a collinear photon emission. An example of E_e distribution in two measurement bins is shown in Figure 4.30. In the example bin,

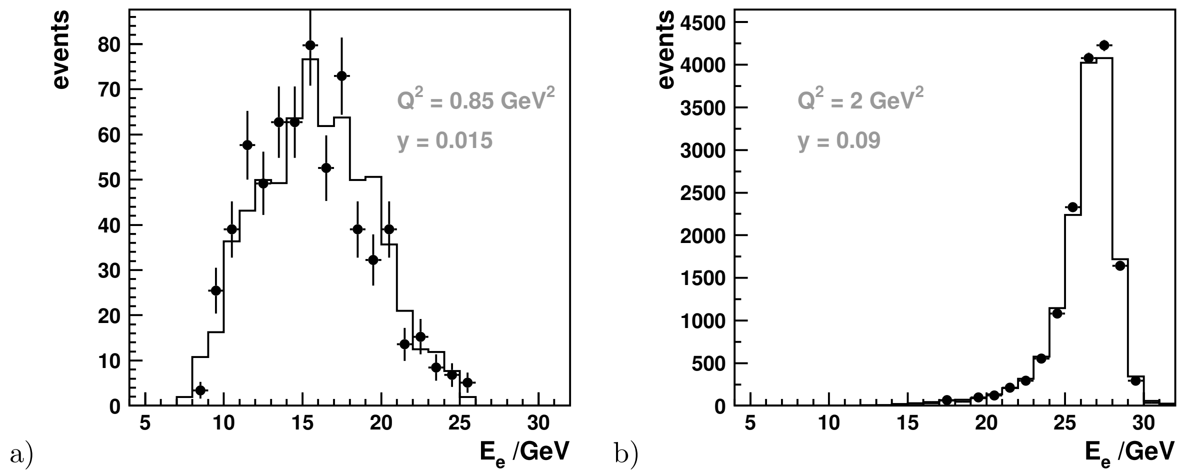

Figure 4.30: Distributions of the incoming electron energy E_e as defined in eq. (4.30) for a bin dominated by ISR (a) and a bin with little ISR contribution (b). Data are represented by closed points while the histograms correspond to the Monte Carlo simulation.

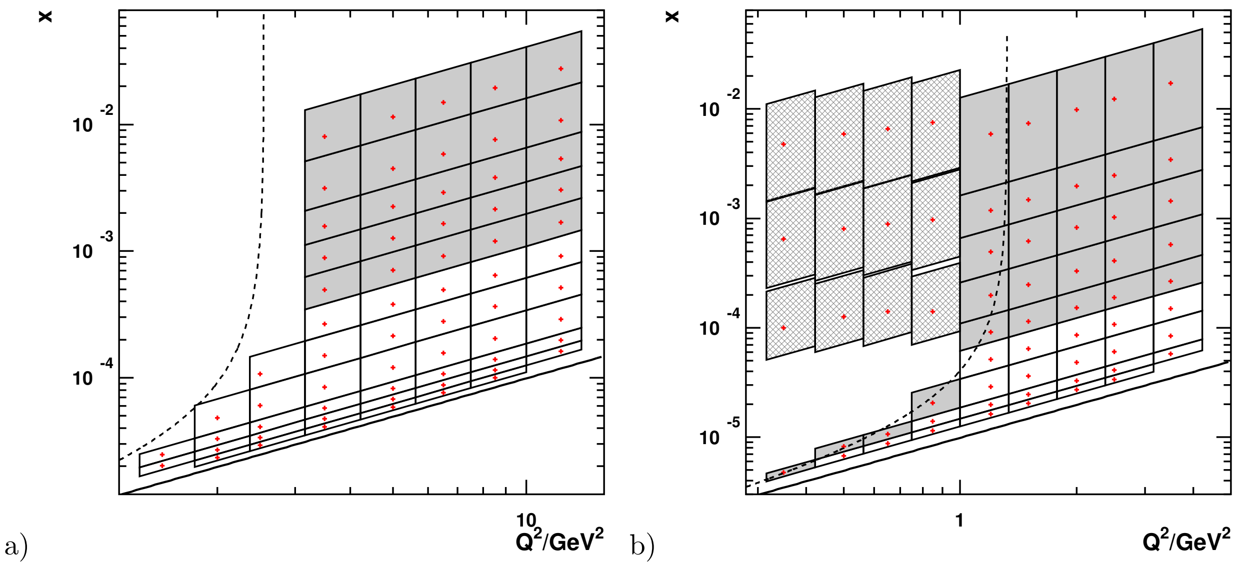

Figure 4.31: Kinematic plane coverage and bin selection of the mb99 (a) and svtx00 (b) data sets in Q^2-x kinematical plane. The electron reconstruction method is used in open boxes while the sigma method is used in shaded and hatched boxes. The hatched boxes correspond to bins measured with ISR events. The bins centers are marked by crosses. The dashed lines correspond to a limit of safe BST and SpaCal acceptance. It is evaluated as a constant polar angle θ_e corresponding to the nominal vertex position plus 1σ of its distribution and radius $R = 10\,\mathrm{cm}$ in the SpaCal plane.

where ISR is dominating, the incoming electron energy is much lower than the beam energy, approximately two times on average. In measurement bins where ISR contributes little the HERA electron beam energy is obtained.

The final selection of bins and event kinematics reconstruction methods is shown in Figure 4.31. Bins where the kinematics is reconstructed with the electron method and sigma method are marked by open and filled boxes, respectively. Hatched boxes correspond to bins measured with ISR events, their x-position is corrected for the mean incoming electron energy as calculated according to eq (4.30).

4.10.2 Measurement uncertainties

The uncertainties of the cross section measurement are divided into four different types

- **Luminosity measurement** - The data have a normalisation uncertainty of 1.3% (mb99 data) and of 1.8% (svtx00 data). This uncertainty is not included in any error bar subsequently shown.
- **Statistics** - The statistical uncertainty of the data is typically 1-2% for the mb99 data set and 1-5% for the svtx00 data set, depending on the kinematic region.
- **Uncorrelated systematics** - An about 2% uncorrelated cross section uncertainty is due to the simulated event statistics. The imperfect description of the BST track reconstruction efficiency contributes by 1% for the mb99 data set and 2% for the svtx00 data set. Further contributions are due to the uncertainty of the radiative corrections (1%) and from the determination of the SpaCal trigger efficiency (0.5%).
- **Correlated systematics** - There are five individual sources contributing to the correlated cross section uncertainties:

  1. Uncertainties of 0.3% at $E_e = 27\,\mathrm{GeV}$ and 2% at 7 GeV [61] were assigned to the electron energy scale for the SpaCal calorimeter. The uncertainty was treated as a linear function of E_e interpolating between the results at 27 GeV and 7 GeV.
  2. The uncertainty on the scattered electron polar angle measurement is 0.2 mrad. The corresponding error on the cross section measurement is typically well below 1% but larger at lowest values of Q^2.
  3. The uncertainty on the hadronic energy scale comprises a number of systematic error sources corresponding to the y_h decomposition: an uncertainty of the LAr hadronic energy scale calibration of 2%, an uncertainty of 3% for the y_h fraction carried by tracks and a 5% uncertainty of the SpaCal hadronic energy scale.
  4. The uncertainty on the hadronic energy scale is further affected by the subtracted noise in the LAr calorimeter. The noise is described to the level of 10% and the corresponding error is propagated to the cross section uncertainty. The largest influence is in the low y region, which is measured with the sigma method.
  5. The uncertainty due to the photoproduction background at large y is estimated from the normalisation error of the PHOJET simulations to about 20%. At low and medium values of $y \lesssim 0.5$ it is negligible.

The total systematic error is calculated from the quadratic summation over all sources of the uncorrelated and correlated systematic uncertainties. The total error of the DIS cross section measurement is obtained from the statistical and systematical errors added in quadrature. In the main region of the analyzed data sets it is about 2-3% for the mb99 data set and 3-4% for the svtx00 data set. At the acceptance edges the errors increase. At highest y bins of the mb99 data set, measured with the s9 subtrigger, the dominant error contribution is due to the PHOJET normalisation. Bins measured with ISR events are affected by limited statistics, the total error fluctuates around 10%. For full error tables of the presented measurement see Appendix C.

4.10.3 Results

The analysis procedure, as described in this thesis, was implemented in the analysis code. To cross check whether the detector response is correctly described in the Monte Carlo simulations it is useful to compare distributions of the main kinematic and technical variables of the analysis. Such a comparison is shown in Figure 4.32 for the case of the mb99 data set. The distributions of the scattered electron energy and polar angle (upper row) in the data are compared to the Monte Carlo simulations. A very good agreement is found demonstrating a well understood response of the sub-detectors involved and the reliable reconstruction of kinematics from the electron side. The fact that also the hadronic side is well understood is demonstrated in the lower row plots of Figure 4.32, where the total $E - p_z$ and the balance of transverse momenta P_t^h/P_t^e are shown. Again, good agreement is found between the data and the simulation. Reconstruction of the kinematic variables is presented in Figure 4.33 of the four momentum transfer squared Q^2 and Bjorken x reconstructed from the electron side and of the inelasticity y reconstructed with the sigma method.

Distributions of the main variables are shown in Figure 4.34 for the analysis at highest y with the s9 subtrigger. The data and simulations are found to be in good agreement. At lowest scattered electron energies, below 5 GeV, the data have a tendency to overshoot the simulations. This effect is not attributed to the normalisation of the PHOJET simulations and may hint to a slightly different behaviour of F_L than assumed in the simulation.

Event control distributions for the svtx00 data set are shown in Figure 4.35. The distribution of the scattered electron energy and polar angle (upper row) in the data are compared to the Monte Carlo simulations. Kinematic variables Q^2 and y as reconstructed with the electron method are shown in the second row. The corresponding quantities reconstructed with the sigma method are presented in Figure 4.36, complemented by the vertex position distribution. Overall, the control distributions show good agreement between the data and the Monte Carlo simulations. A discrepancy between data and Monte Carlo simulation for the polar angle θ_e measurement when reaching 3.1 rad is related to edge effects of BST and SpaCal acceptance.

The cross section determination has been performed using the two different reconstruction methods, the electron and the Σ method. This allows to cross check the central values of the cross section and also to estimate part of the systematic errors. In Figures 4.37 and 4.38 the comparison of the DIS cross sections determined by the electron and Σ methods are presented for both analyzed data samples, mb99 and svtx00. Results are found to be in good agreement. The fact that both cross sections agree so well despite degrading resolutions of the electron method reconstruction towards values of low y confirms the correct calibrations of the energy scales.

The comparison of the DIS cross section with and without the $E - p_z$ cut for svtx00 data is shown in Figure 4.39. It is seen that results are consistent, however, for low values of Q^2 only the relaxation of the $E - p_z$ cut leads to reliable results at large x.

The results on the cross section measurement presented in this thesis are summarized in Figure 4.40 and compared with the cross sections measured by ZEUS [38] and NMC [66] collaborations in the Q^2 acceptance region of the present analysis. The inner error bars represent the statistical errors. The full errors include the statistical and systematic errors added in quadrature. In the regions of overlaps in x the data presented here confirm the former measurements within the uncertainties quoted.

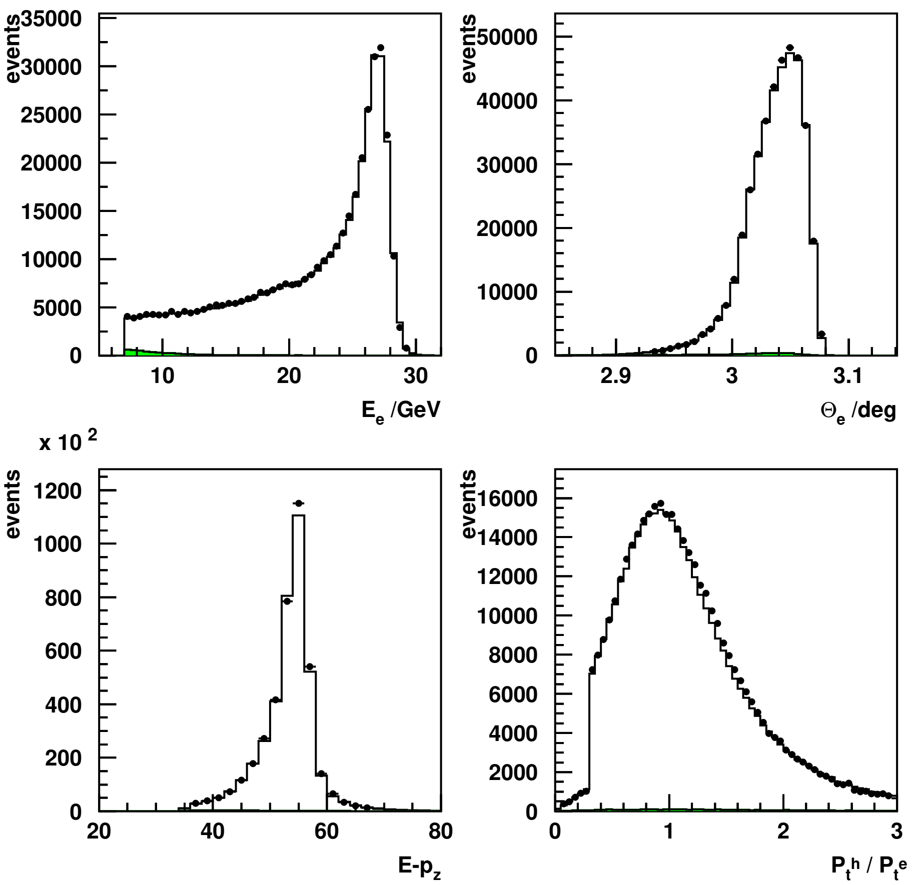

Figure 4.32: Event control distributions for the **mb99** data set: energy of the scattered electron and its polar angle, $E - p_z$ and balance of the transverse momenta P_t^h/P_t^e. Data are represented by closed points while the histograms correspond to the Monte Carlo simulation of DIS and the small photoproduction background (shaded).

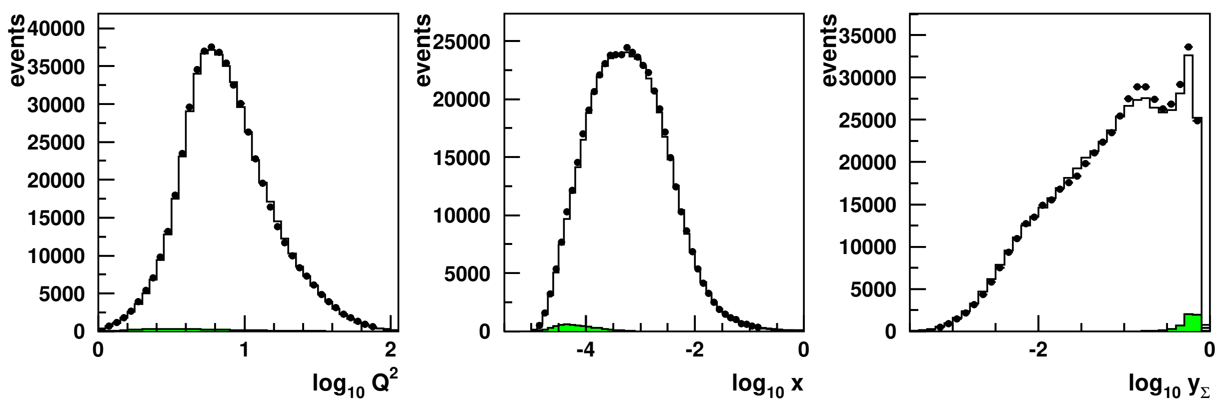

Figure 4.33: Event kinematics distributions for the **mb99** data set: four momentum transfer squared Q_e^2, Bjorken x_e and inelasticity y_Σ. Data are represented by closed points while the histograms correspond to the Monte Carlo simulation of DIS and the photoproduction background (shaded).

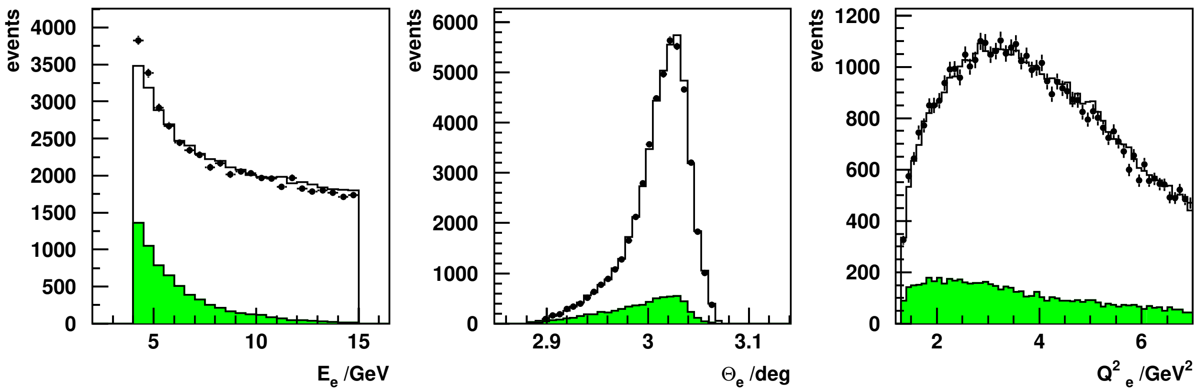

Figure 4.34: Event control distributions for the high y analysis of the **mb99** data set: energy of the scattered electron and its polar angle and electron method reconstruction of Q^2. Data are represented by closed points while the histograms correspond to the Monte Carlo simulation of DIS and the photoproduction background (shaded).

4.11 Rise of $\mathbf{F}_2(x, Q^2)$ at low $\mathbf{Q}^2$

The cross section measurement, presented in the previous section, is used for the phenomenological analysis of the F_2 rise, as explained in in Section 1.7. Data are selected in the $y < 0.35$ range to suppress the contribution of the structure function F_L at high y. To further improve the precision of the measured cross section even and odd adjacent Q^2 bins are combined into one Q^2 bin, starting from $Q^2 = 0.65\,\mathrm{GeV}^2$. The cross section after re-binning is shown in Figure 4.41. The total errors of the mb99 and svtx00 data sets in the main kinematic region reach level of 1.5-2% and 2-3%, respectively.

The x dependence of F_2 at low x is consistent with a power law:

$$F_2(x, Q^2) = c(Q^2) \cdot x^{-\lambda(Q^2)}. \tag{4.31}$$

The functions $\lambda(Q^2)$ and $c(Q^2)$ are determined from fits of the form (4.31) to the F_2 structure function data. The fits are restricted to the region $x < 0.01$. Uncorrelated and statistical uncertainties of the $\lambda(Q^2)$ and $c(Q^2)$ determination include errors of the fit to the F_2 points with their statistical and uncorrelated systematic errors. The correlated systematic uncertainties are treated separately and added in quadrature to the total error. In this treatment the F_2 points with statistical and uncorrelated systematic errors are shifted according to the correlated systematic errors and re-fitted. The corresponding systematic uncertainty is the difference of parameters λ and c as compared to the central fit parameters. The total correlated systematic uncertainty consists of uncertainties from five correlated error sources added in quadrature.

The results are presented in Figure 4.42 and in Table C.3. At $Q^2 > 2\,\mathrm{GeV}^2$ the extracted function $\lambda(Q^2)$ is consistent with the extrapolation of the linear fit to larger Q^2 data by the H1 collaboration [10]. At low $Q^2 < 2\,\mathrm{GeV}^2$ the extracted points are found to be above the linear fit extrapolation.

4.12 $\mathbf{F}_L(x, Q^2)$ determination

The new low Q^2 data are used to determine the F_L structure function for the first time in the transition region, for $Q^2 < 1\,\mathrm{GeV}^2$. Previously, the F_L data were obtained with the so called

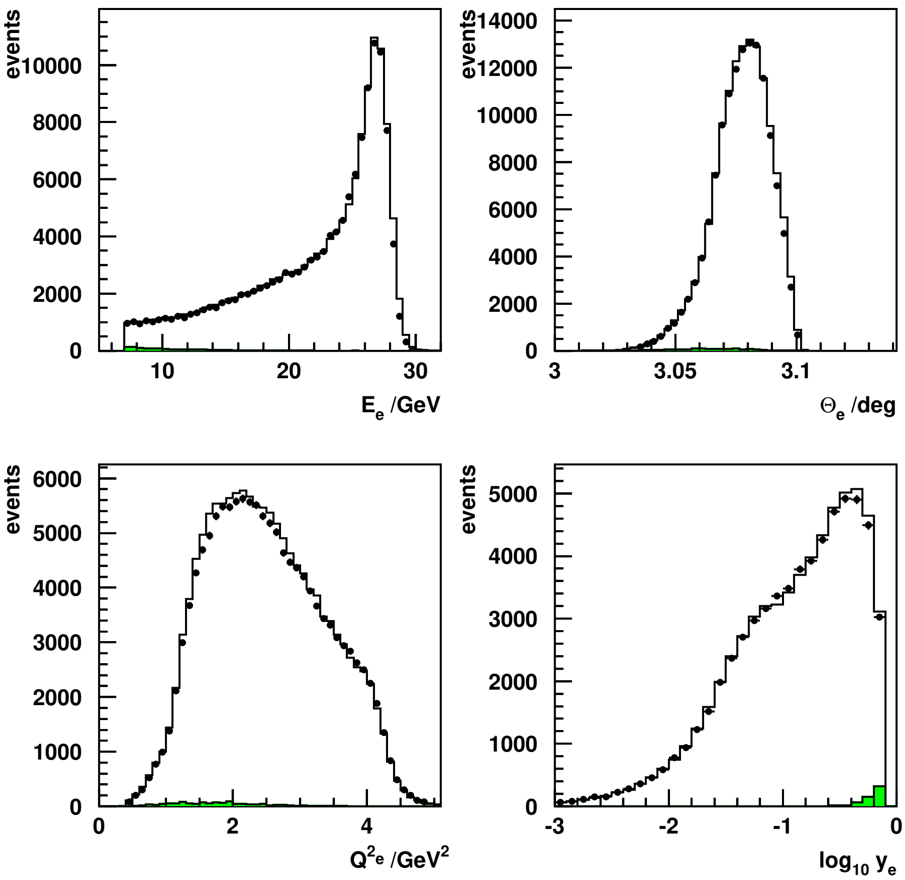

Figure 4.35: Event control distributions for the **svtx00** data set: energy of the scattered electron and its polar angle, $E - p_z$ and balance of the transverse momenta P_t^h/P_t^e. Data are represented by closed points while the histograms correspond to the Monte Carlo simulation of DIS and the small photoproduction background (shaded).

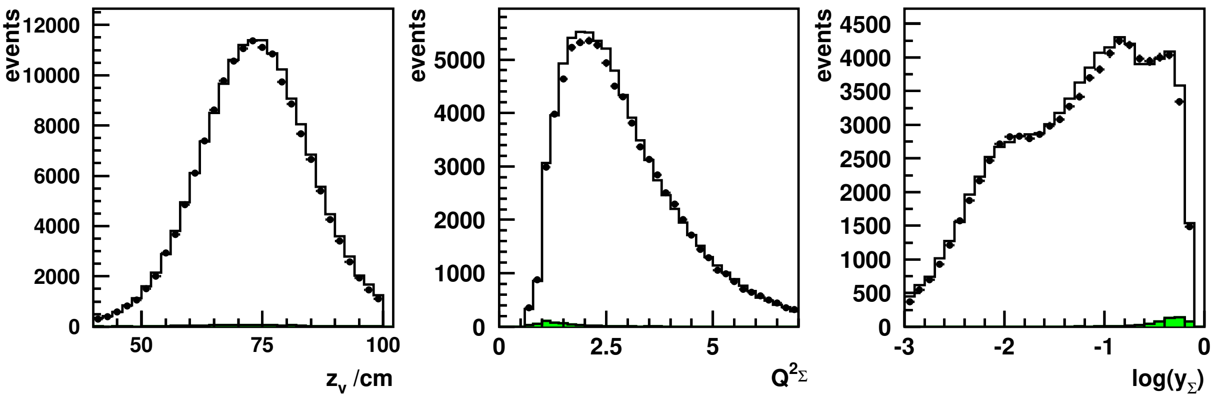

Figure 4.36: Event kinematics distributions for the **svtx00** data set: four momentum transfer squared Q_e^2, Bjorken x_e and inelasticity y_Σ. Data are represented by closed points while the histograms correspond to the Monte Carlo simulation of DIS and the photoproduction background (shaded).

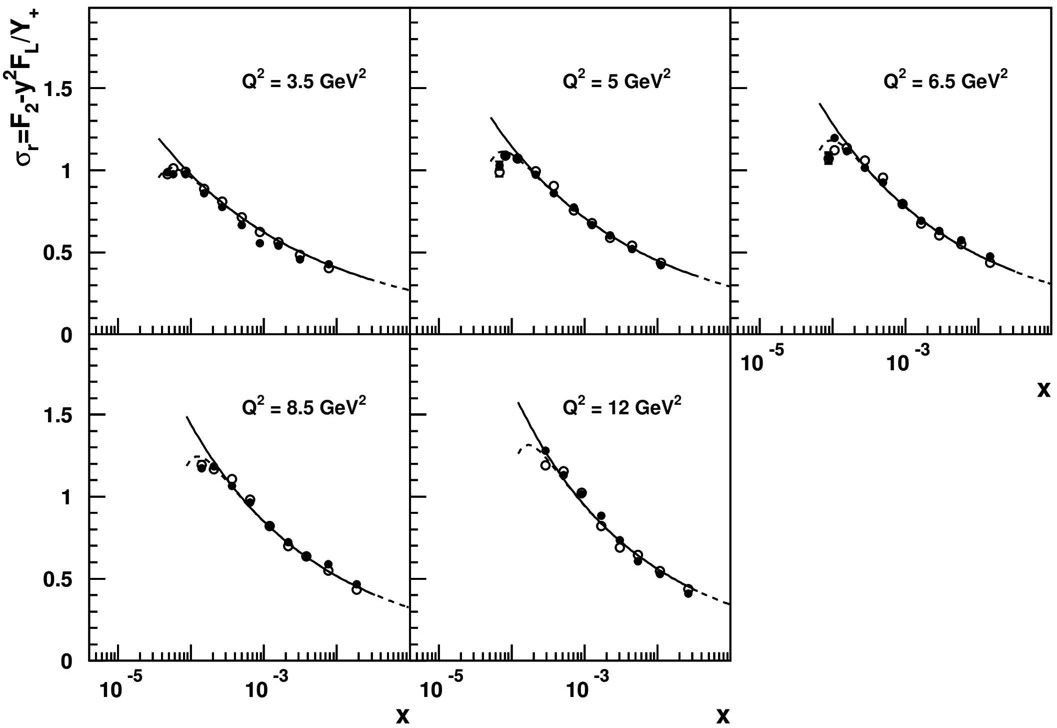

Figure 4.37: Reduced DIS cross section measurement based on the **mb99** data with the electron (closed points) and sigma (open points) methods. The error bars correspond to the statistical uncertainty only.

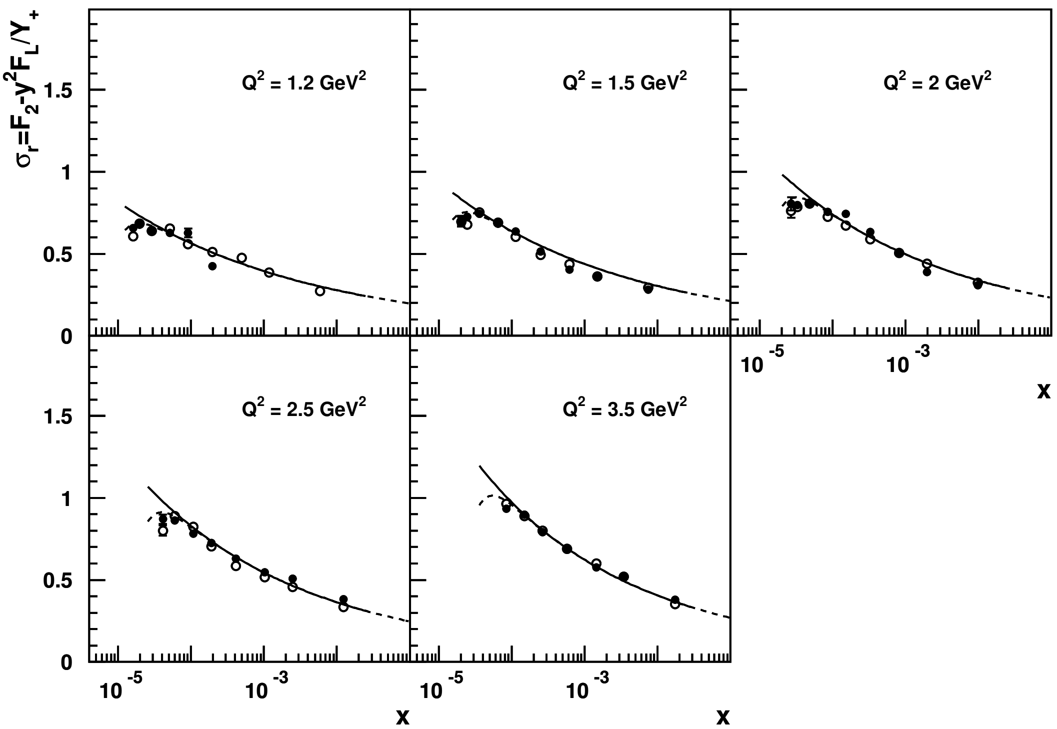

Figure 4.38: Reduced DIS cross section measurement based on the **svtx00** data with the electron (closed points) and sigma (open points) methods. The error bars correspond to the statistical uncertainty only.

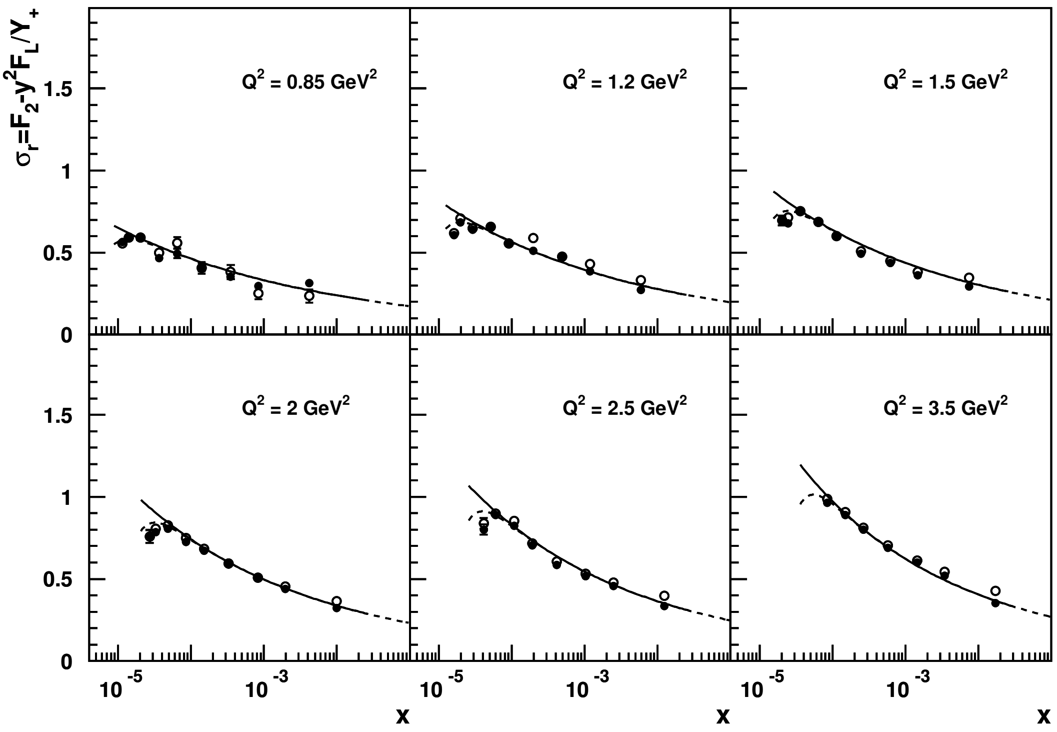

Figure 4.39: Reduced DIS cross section measurement based on the **svtx00** data reconstructed with the sigma method with (open points) and without (closed points) $E - p_z$ cut. For even lower Q^2 only the relaxation of the $E - p_z$ cut leads to reliable results at large x.

derivative method [12, 61]. Here a new method, the so called *shape method*, see also [63, 64], is used to obtain the F_L data with a better precision. The method is motivated by the following observations

1. The shape of the cross section bending at $y \gtrsim 0.5$, see Figure 4.41, is driven by the steep kinematic factor y^2/Y_+ rather than by the x dependence of F_L.
2. The result on F_L from the derivative method consists in a few points close in y with sizeable errors. The precision of the measurement does not allow to resolve the x dependence of $F_L(x, Q^2)$ on this basis.

It follows from the second point that a single, more precise F_L point per Q^2 bin is desirable rather than a number of less precise points in an anyhow very narrow range of x corresponding to the highest y region. The data do not constrain the x dependence of F_L. Consequently, the F_L structure function is considered to be constant ($F_L = F_L(Q^2)$), for each Q^2 bin in the narrow x range, high y range of sensitivity to F_L governed by the y^2/Y_+ term. The effect of a non-constant F_L is added to the measurement error.

In agreement with the results presented in the previous section, the method assumes that the structure function $F_2(x, Q^2)$ behaves like $c \cdot x^{-\lambda}$ at fixed Q^2. On this basis the reduced cross section distribution in each Q^2 bin can be parameterized and fitted as:

$$\sigma_{FIT} = c \cdot x^{-\lambda} - \frac{y^2}{1 + (1 - y)^2} F_L. \tag{4.32}$$

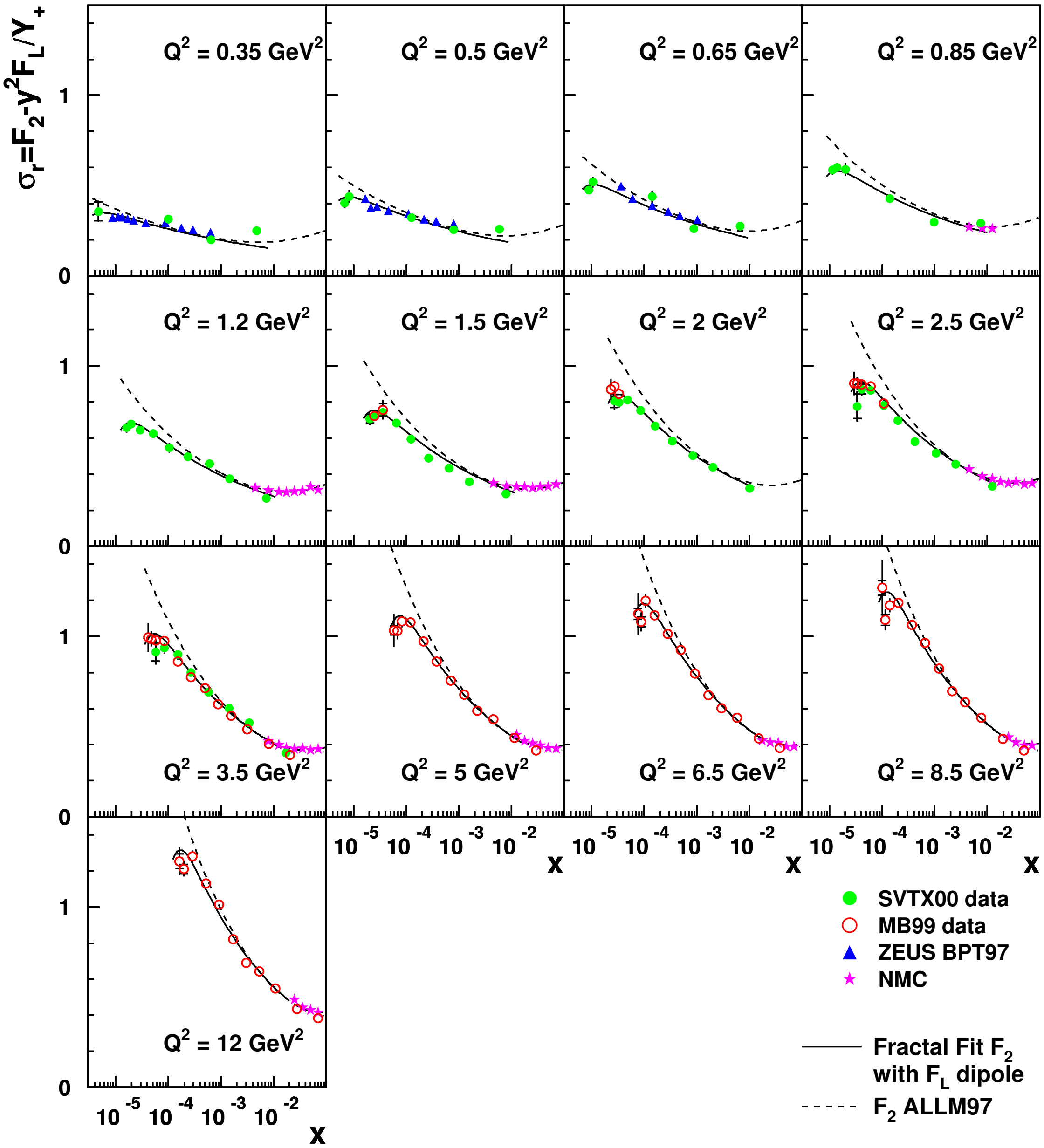

Figure 4.40: Measurement of the inclusive DIS cross section with the svtx00 and mb99 data sets. This analysis (circles) is compared to data from ZEUS (BPT97, triangles) [38] and from NMC (stars) [66]. The curves are from a phenomenological parametrisation of the cross section calculating F_2 within the fractal proton structure model and using a GBW dipole model prediction for F_L (solid) and phenomenological F_2 parametrisation ALLM97 (dashed) [67].

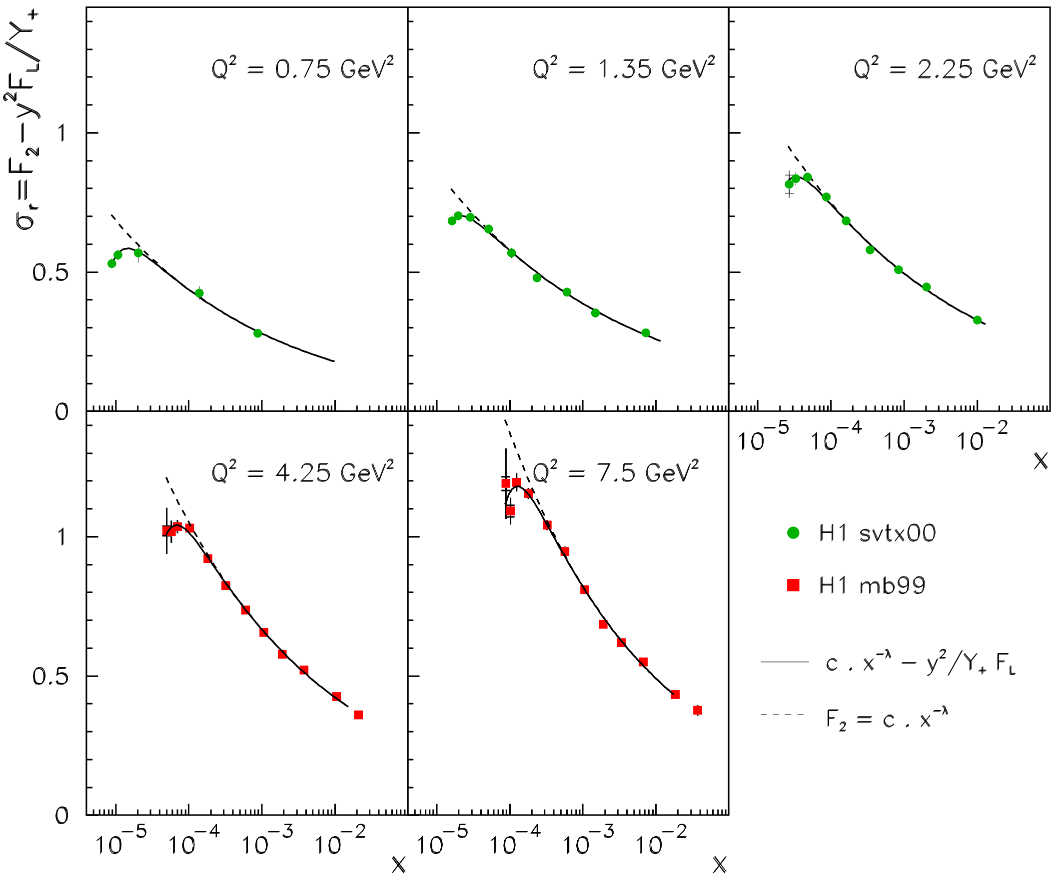

Figure 4.41: The reduced cross section as a function of x in bins of Q^2 as determined in this thesis. The inner error bars represent the statistical errors. The full errors include the statistical and systematic errors added in quadrature. The dashed lines show a function of the form $c \cdot x^{-\lambda}$ representing the F_2 contribution to the fitted cross section. The solid lines show fits of the form $\sigma_r = c \cdot x^{-\lambda} - y^2/Y_+ \, F_L$, from which F_L is extracted in the shape method, see text.

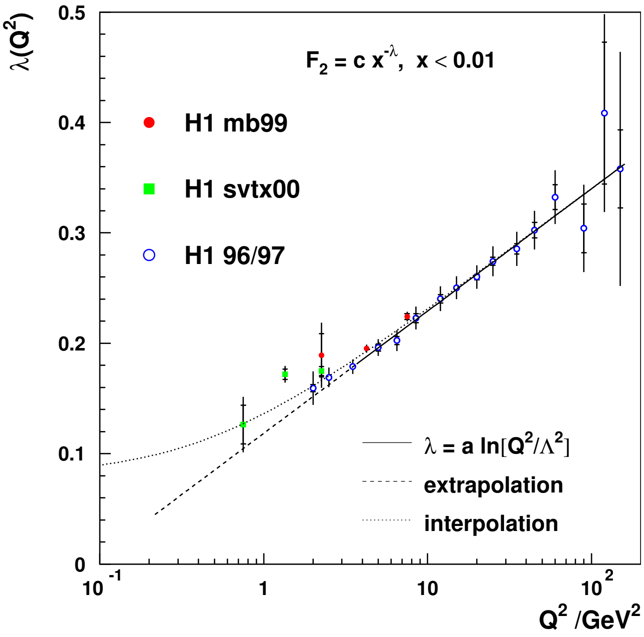

Figure 4.42: Determination of the function $\lambda(Q^2)$ from fits of the form $F_2(x, Q^2) = c(Q^2) \cdot x^{-\lambda(Q^2)}$ to F_2 structure function data presented in this thesis. The straight line corresponds to a fit of the form $a \ln[Q^2/\Lambda^2]$ using published H1 data (blue points [10]) for $Q^2 \geq 3.5$ GeV^2, the dashed line to its extrapolation to lower values of Q^2. The dotted line is an interpolation between the λ behaviour at large Q^2, as given by the fit, and in the photoproduction limit $Q^2 \to 0$ where $\lambda \approx 0.08$.

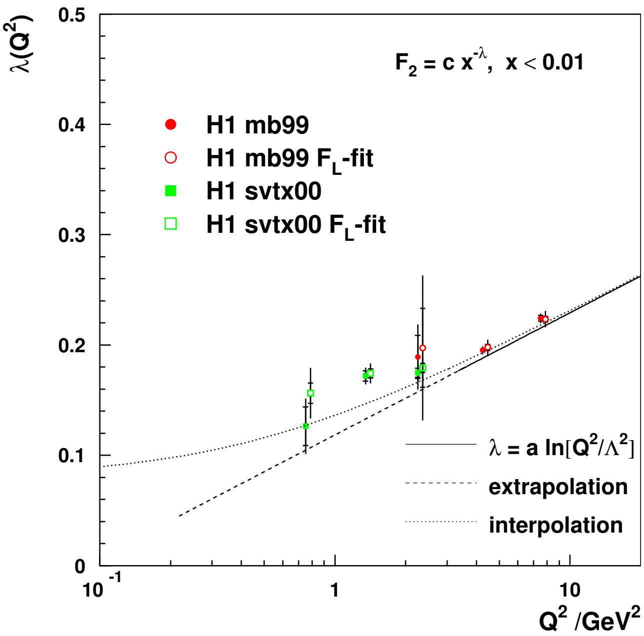

Figure 4.43: Determinations of the function $\lambda(Q^2)$ from fits of the form $F_2(x, Q^2) = c(Q^2) \cdot x^{-\lambda(Q^2)}$ to F_2 structure function data presented in this thesis. These are compared to the F_L fit result which includes all data and F_L according to eq. (4.32) while the standard λ determination excludes the F_L affected region demanding $y < 0.35$. The straight line corresponds to a fit of the form $a \ln[Q^2/\Lambda^2]$ using published H1 data [10]) for $Q^2 \geq 3.5$ GeV^2, the dashed line to its extrapolation to lower values of Q^2. The dotted line is an interpolation between the λ behaviour at large Q^2, as given by the fit, and in the photoproduction limit $Q^2 \to 0$ where $\lambda \approx 0.08$.

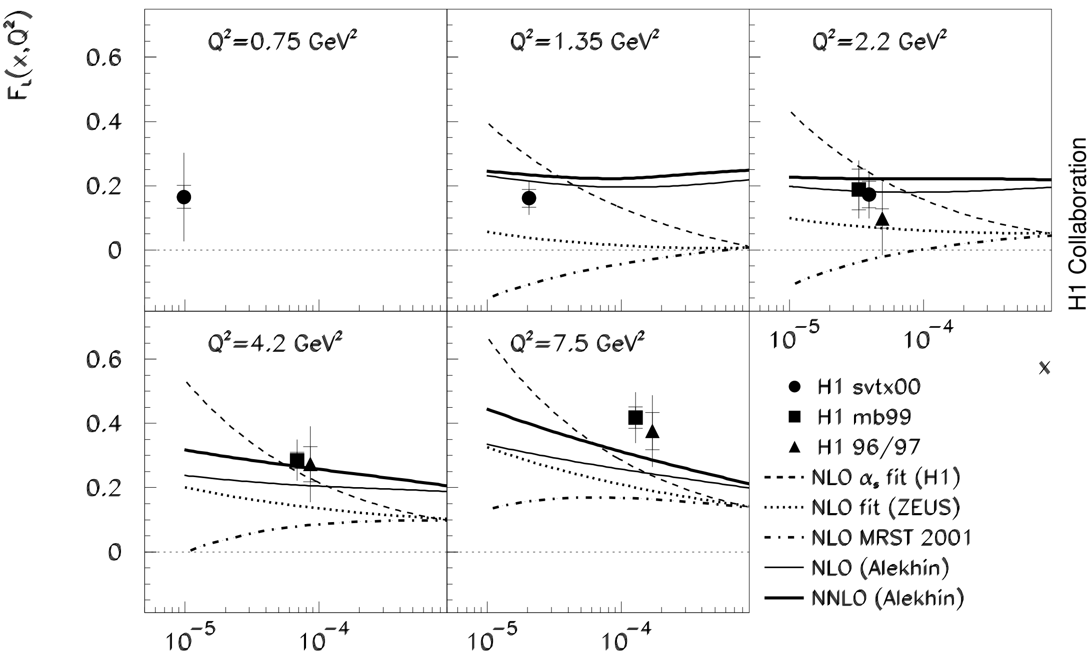

Figure 4.44: Determination of $F_L(x, Q^2)$ (closed squares and circles) from low Q^2 cross section measurements. The inner error bars correspond to the statistical errors. The full errors include the statistical, uncorrelated and correlated systematic errors added in quadrature. The result is compared to various NLO and NNLO QCD fits and to the previous H1 determination [12] (triangles).

The method is technically identical to the extraction of c and λ in the previous section with one more parameter added. Furthermore, the full kinematic range of the cross section measured is used, i.e. without the $y < 0.3$ cut. The fit parametrisation (4.32) provides an excellent description of the reduced cross section, see Figure 4.41. The c and λ values extracted from this fit turn out to be in a good agreement with those obtained in the previous section. See Figure 4.43 for the comparison of lambda.

The correlated, uncorrelated and statistical errors are treated in the same manner as in the case of the c and λ determination. Additionally, the error due to a non-constant F_L is estimated comparing the fit results using the constant F_L approximation with those using the steepest theoretical estimate (H1 QCD fit [12]).

The results are presented in Figure 4.44 together with predictions of various higher order QCD fits, partially extrapolated below their minimum Q^2 of applicability. The values of $F_L(x, Q^2)$ are consistent with the previous determination by the H1 Collaboration (closed triangles), but are more precise and extend the kinematical region, in which $F_L(x, Q^2)$ is determined, to lower Q^2. As can be seen from the different curves there is a significant uncertainty for the F_L prediction in the NLO QCD fits. This reflects the uncertainty of the initial gluon distribution. The H1 data clearly favor a positive, not small F_L at low Q^2 and small x, as is preferred by the H1 and Alekhin's fits while the MRST and ZEUS predictions are low. A negative F_L value at small x is experimentally ruled out by the measured turn-over of the reduced cross section, see Figure 4.41, which leads to $F_L > 0$. It becomes evident from Figure 4.44 that the x dependence of F_L needs to be measured which requires to operate HERA at reduced proton beam energy.

An overview of all current H1 data on $F_L(x, Q^2)$, from $Q^2 = 0.75\,\mathrm{GeV}^2$ to $700\,\mathrm{GeV}^2$ and for fixed $W = 276\,\mathrm{GeV}$, is given in Figure 4.45. It comprises the results of this analysis, the results based

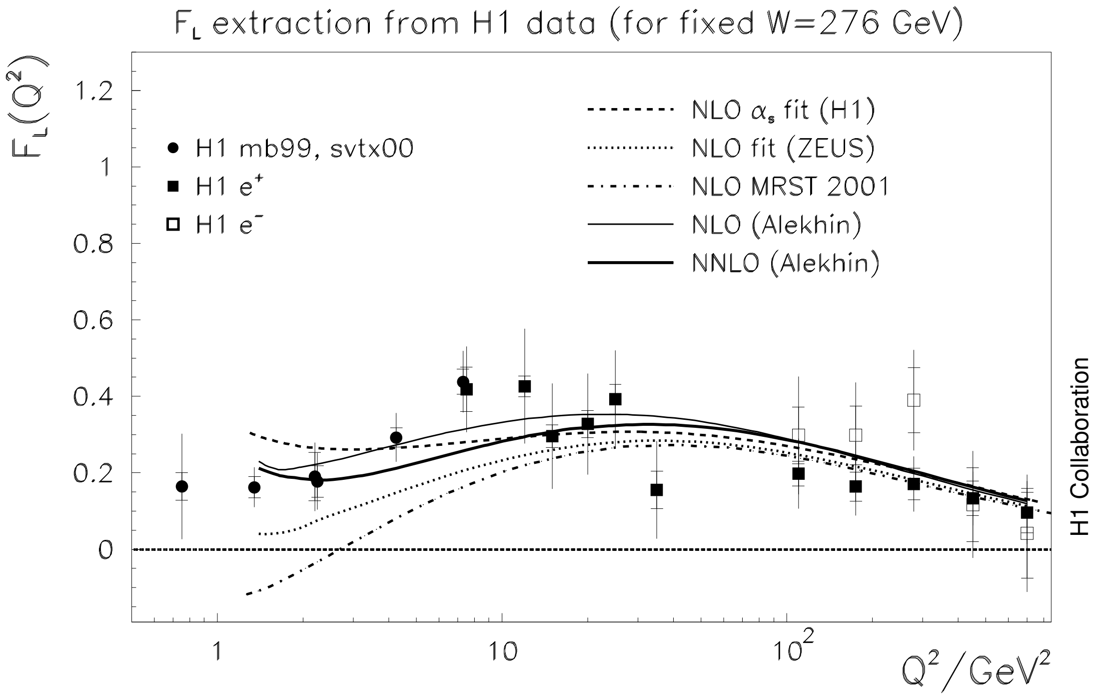

Figure 4.45: Q^2 dependence of $F_L(x, Q^2)$ (at fixed $W = 276\,\mathrm{GeV}$), summarizing the data from the H1 experiment. The inner error bars represent the statistical errors. The full errors include the statistical, uncorrelated and correlated systematic errors added in quadrature. The result is compared to various NLO and NNLO QCD fits.

on data collected in 96/97 [12] and also the recently published high Q^2 results from e^+p and e^-p data [65]. All QCD fits describe the data at larger Q^2 while at lower Q^2 similar conclusions can be drawn as for the x dependence discussed above.

Summary

This thesis presents a new cross section measurement in the kinematic domain $0.35 \leq Q^2 \leq 12\,\mathrm{GeV}^2$ using new data taken in special runs by the H1 collaboration. This measurement provides the first precise low x data on the inclusive DIS cross-section in the transition region from the non-perturbative to the deep-inelastic domain in a wide range of inelasticity y. Access to the extreme regions of y is possible by using the Backward Silicon Tracker which at high y suppresses neutral particle background and which at low y, where the hadronic final state escapes detection in proton beam direction, restores efficiently the vertex reconstruction efficiency.

The region of large x at low Q^2, below $1\,\mathrm{GeV}^2$, is accessed by using QED radiative events in a new way, without an explicit detection of the radiated photon. The obtained cross section is found to have a typical error on the level of 10% and is consistent with predictions based on phenomenological parametrisations.

Based on the cross section data a novel method is introduced here to extract F_L for the first time at low Q^2. The strong y dependence observed for the cross section at high y leads to positive results of the longitudinal structure function down to lowest Q^2. Indeed, the extracted F_L is found to be non-zero and positive for all values of Q^2 where it is determined. Collecting all H1 results, $F_L(x, Q^2)$ data are presented in a wide Q^2 range, from 0.75 to $700\,\mathrm{GeV}^2$. A measurement of the x dependence of $F_L(x, Q^2)$, independent of assumptions on $F_2(x, Q^2)$ and more accurately, can only be performed at HERA with a variation of the proton beam energy.

A completely new approach to study the proton structure at low x is introduced, by looking at fractal patterns in the parton densities. The proton is seen as a multi-fractal and the corresponding fractal dimensions are determined by constructing a phenomenological model which is fitted to the H1 data. This approach is found to describe the data excellently and can be used to obtain deeper and complementary understanding of low x, Q^2 physics. In this thesis a prediction of the pion structure function F_2^π is discussed which is found to be consistent with recent F_2^π data. Also a discussion on the 'negativity' of one of the determined dimensions is presented. The low x behaviour of this model is compared to the GBW saturation model and found to be consistent with the last version of the GBW model in the region of existing data at low Q^2. However, at even lower values of x the models have different behaviour due to the saturation effect explicitly built in the GBW model.

To conclude, this thesis presents the first accurate HERA data on the inclusive ep scattering cross section at low x for $Q^2 \sim 1\,\mathrm{GeV}^2$ accessed with new instrumentation and novel analysis methods to extract F_2 and F_L besides a new view on low x proton structure based on fractal patters.

Appendix A

Structure functions

The NC DIS cross section in the one-photon exchange approximation can be calculated from

$$\sigma \sim L_{\mu\nu} W^{\mu\nu}, \tag{A.1}$$

where $L_{\mu\nu}$ is the leptonic tensor known from QED. The hadronic tensor $W^{\mu\nu}$ is not completely known and can be expressed using P and q, the four-momenta of the interacting proton and the virtual photon, respectively, combined with basic tensors of rank two[1] in order to form a general Lorentz tensor:

$$W_{\mu\nu}(P,q) = -W_1 g_{\mu\nu} + W_2 \frac{P_\mu P_\nu}{M_p^2} + iW_3 \epsilon_{\mu\nu\alpha\beta} P_\alpha P_\beta + W_4 q_\mu q_\nu + W_5 (P_\mu q_\nu + P_\nu q_\mu) + iW_6 (P_\mu q_\nu - P_\nu q_\mu). \tag{A.2}$$

The $W_i(P,q)$ functions are real functions of P and q, which depend on the internal structure of the proton. Parity conservation leads to $W_3 = 0$ and a gauge invariance requirement expressed as $q^\mu W_{\mu\nu} = 0$ yields $W_6 = 0$ and the following relations

$$\begin{aligned} W_5(P,q) &= -W_2(P,q) \frac{Pq}{q^2 M_p^2} \\ W_4(P,q) &= W_1(P,q) \frac{1}{q^2} + W_2(P,q) \frac{(Pq)^2}{q^4 M_p^2}. \end{aligned} \tag{A.3}$$

Thus out of originally six functions only two are independent. The terms proportional to q^μ and q^ν can be dropped since they would vanish anyway after contraction with the leptonic tensor $L_{\mu\nu}$. Finally, the hadronic tensor can be written as

$$W_{\mu\nu}(P,q) = -W_1(P,q) g_{\mu\nu} + W_2(P,q) \frac{P_\mu P_\nu}{M_p^2}. \tag{A.4}$$

[1] The basic tensors of rank two are the symmetric metric tensor $g_{\mu\nu}$ and the totally antisymmetric Levi-Civita pseudotensor $\epsilon_{\mu\nu\alpha\beta}$.

After contraction with the leptonic tensor $L_{\mu\nu}$ one has

$$L^{\mu\nu}W_{\mu\nu} = \frac{4(kP)}{y}\left[\frac{\nu}{M_p}W_2\left(1 - y - \frac{M_p^2x^2y^2}{Q^2}\right) + 2xW_1\frac{y^2}{2}\right]. \tag{A.5}$$

It is common to introduce new functions instead of W_1 and W_2

$$F_1 \equiv W_1 \qquad F_2 \equiv \frac{\nu}{M_p}W_2 \tag{A.6}$$

in terms of which the equation (A.5) reads

$$L^{\mu\nu}W_{\mu\nu} = \frac{4(kP)}{y}\left[F_2(x,Q^2)\left(1 - y - \frac{M_p^2x^2y^2}{Q^2}\right) + 2xF_1(x,Q^2)\frac{y^2}{2}\right]. \tag{A.7}$$

Furthermore, it is useful to introduce the *longitudinal structure function* F_L

$$F_L(x,Q^2) \equiv F_2(x,Q^2)\left(1 + \frac{4M_p^2x^2}{Q^2}\right) - 2xF_1(x,Q^2), \tag{A.8}$$

which corresponds to the cross section of longitudinally polarized photons while F_1 corresponds to transversally polarized photons and F_2 has contributions from both polarizations.

Thus evaluating the double differential cross section with the new set of structure functions the following relation is obtained

$$\frac{d\sigma^2}{dxdQ^2} = \frac{2\pi\alpha^2}{Q^4x}Y_+\left[F_2(x,Q^2) - \frac{y^2}{Y_+}F_L(x,Q^2)\right], \qquad Y_+ = 1 + (1-y)^2, \tag{A.9}$$

neglecting $M_p^2x^2y^2/Q^2$ in eq. A.7 as is possible in the HERA kinematic region. By convention, the term in brackets is denoted as the *reduced cross section*

$$\sigma_r = F_2(x,Q^2) - \frac{y^2}{Y_+}F_L(x,Q^2). \tag{A.10}$$

Appendix B

Quantum path dimension in the presence of a local potential

Feynman and Hibbs' [21] consider the following Hamiltonian

$$H = -\frac{\hbar^2}{2m}\Delta + V(x), \tag{B.1}$$

where $V(x)$ is an arbitrary local potential. The transition element from an initial state $|x_{in}, t = 0\rangle$ to a final state $|x_{fi}, t = T\rangle$ is written as

$$\langle x_{fi}, t = T | x_{in}, t = 0\rangle \;=\; \left\langle x_{fi} \middle| exp[-\frac{i}{\hbar}HT] \middle| x_{in} \right\rangle \;=\; \int [dx(t)] exp\Big[\frac{i}{\hbar}S[x(t)]\Big], \tag{B.2}$$

where the integration is done over all paths starting in x_{in} and ending at x_{fi}, weighted by a phase factor $exp[\frac{i}{\hbar}S[x(t)]]$. The $S[x(t)]$ is the classical action corresponding to the Hamiltonian (B.1) for a particular path,

$$S = \int_0^T dt \frac{m}{2}\dot{x}^2 - V(x(t)). \tag{B.3}$$

In analogy, the transition element for an operator $F[\hat{x}]$ is given as

$$\langle F[\hat{x}]\rangle \;=\; \langle x_{in}, t = T | F[\hat{x}] | x_{fi}, t = 0\rangle \;=\; \int [dx(t)] F[\hat{x}] exp\Big[\frac{i}{\hbar}S[x(t)]\Big]. \tag{B.4}$$

Assume that time is divided into little slices δ (later the limit $\delta \to 0$ will be considered), then the action can be expressed as

$$S = \sum_{N-1}^{i=1} \delta \; \Big[\frac{m}{2}\Big(\frac{x_{i+1} - x_i}{\delta}\Big)^2 - V(x_i)\Big]. \tag{B.5}$$

According to Feynman and Hibbs the following general relation holds

$$\left\langle \frac{\partial F}{\partial x_k} \right\rangle = -\frac{i\delta}{\hbar}\left\langle F\frac{\partial S}{\partial x_k} \right\rangle. \tag{B.6}$$

For the special case of $F = x_k$ a combination of equations (B.5) and (B.6) gives

$$\langle 1 \rangle = \frac{i}{\hbar}\left\langle m x_k \left(\frac{x_{k+1} - x_k}{\delta} - \frac{x_k - x_{k-1}}{\delta} \right) + \delta x_k V'(x_k) \right\rangle. \tag{B.7}$$

The potential term $\delta x_k V'(x_k)$ becomes negligible in the limit $\delta \to 0$ leading to usual *commutation relations* of particle momentum and position operators

$$\left\langle m \frac{x_{k+1} - x_k}{\delta} x_k \right\rangle - \left\langle x_k m \frac{x_k - x_{k-1}}{\delta} \right\rangle = \frac{\hbar}{i}\langle 1 \rangle. \tag{B.8}$$

The second term on the l.h.s. can be advanced in time by one time slice δ

$$\left\langle x_k m \frac{x_k - x_{k-1}}{\delta} \right\rangle = \left\langle x_{k+1} m \frac{x_{k+1} - x_k}{\delta} \right\rangle + O(\delta). \tag{B.9}$$

Substituting (B.9) into (B.8) and considering the limit $\delta = \Delta t \to 0$ one obtains

$$\begin{aligned} \langle (x_{k+1} - x_k)^2 \rangle &= -\frac{\hbar\delta}{im}\langle 1 \rangle, \\ \langle (\Delta x)^2 \rangle &\propto \frac{\hbar}{m}\Delta t. \end{aligned} \tag{B.10}$$

Furthermore, it is possible to prove the relation

$$\langle (\Delta x)^2 \rangle = \frac{2}{\pi}\langle |\Delta x| \rangle^2 \tag{B.11}$$

and thus finally substituting (B.11) into (B.10) the following relation between the time and space increments is obtained

$$\langle |\Delta x| \rangle^2 \propto \Delta t. \tag{B.12}$$

This relation is identical with relation (2.5) from Section 2.2 and implies $d_f = 2$ for the fractal dimension of typical unmonitored quantum paths in the case of classical quantum mechanics.

Appendix C

Tables of the experimental results

This Appendix contains tables of the experimental results presented in this analysis. The DIS cross section measurement and determination of the structure function F_2 is presented in Tables C.1 and C.2 for mb99 and svtx00 data sets, respectively. Values in columns correspond to (from left)

- the kinematic variables Q^2, x and y of the bin centers. The value of Bjorken x variable is calculated from the inelasticity y via eq. (1.4) where the center of mass energy s is evaluated with the electron and proton beam energies of 27.55 GeV and 920 GeV, respectively.
- the result of the measurement of the reduced DIS cross section σ_r and of the structure function F_2.
- the total error of the measurement δ_{tot}, in percent, and its components, i.e. statistical error δ_{sta}, uncorrelated systematical error δ_{unc} and correlated systematical error δ_{corr}. All errors are presented in percent.
- the last five columns represent the contributions to the correlated systematical error from the scattered electron energy and polar angle measurements (δ_{E_e}, δ_{θ_e}), from the uncertainty of the hadronic scale and noise in the LAr calorimeter ($\delta_{E_{had}}$, δ_{noise}) and from the photoproduction background ($\delta_{\gamma p}$).

The data on $\lambda(Q^2)$ and $c(Q^2)$ from fits to the F_2 structure function at $y < 0.35$ are presented in Table C.3. The statistical and systematic errors are on the absolute scale.

The data on the longitudinal structure function F_L are presented in Table C.4. The values in first three columns corresponds to the kinematic variables Q^2, x, y where F_L (column 4) is determined. The statistical and systematic errors, enlisted in the last two columns, are on the absolute scale.

Q^2 /GeV^2	x	y	σ_r	F_2	δ_{tot}	δ_{sta}	δ_{unc}	δ_{corr}	δ_{E_e}	δ_{θ_e}	$\delta_{E_{had}}$	δ_{noise}	$\delta_{\gamma p}$
1.50	0.0000247	0.600	0.723	0.780	4.97	2.22	2.44	3.72	-3.20	1.40	0.70	-0.10	1.06
1.50	0.0000361	0.410	0.756	0.776	8.64	4.64	4.28	5.91	-2.00	5.50	0.60	-0.50	0.21
2.00	0.0000235	0.840	0.870	1.018	7.55	1.98	2.50	6.84	-1.50	-0.30	4.00	-0.50	5.31
2.00	0.0000270	0.730	0.886	0.988	3.93	1.72	2.03	2.89	-1.30	-0.20	1.00	-0.20	2.37
2.00	0.0000329	0.600	0.845	0.905	3.09	1.40	1.75	2.13	-1.80	0.30	0.60	-0.20	0.90
2.50	0.0000294	0.840	0.902	1.056	7.84	2.10	2.65	7.07	-0.20	-0.30	3.70	-0.40	6.00
2.50	0.0000338	0.730	0.903	1.010	3.92	1.73	1.88	2.97	-1.50	-0.40	0.80	-0.10	2.40
2.50	0.0000411	0.600	0.898	0.961	2.64	1.23	1.56	1.74	-1.30	-0.30	0.60	-0.10	0.94
2.50	0.0000601	0.410	0.886	0.908	2.18	0.98	1.46	1.28	-1.10	0.60	0.20	-0.10	0.16
2.50	0.0001072	0.230	0.793	0.798	3.37	1.81	1.81	2.20	-0.90	2.00	0.00	-0.10	0.02
3.50	0.0000411	0.840	0.994	1.161	8.21	2.25	2.59	7.46	0.30	-0.40	3.80	-0.50	6.38
3.50	0.0000473	0.730	0.987	1.103	4.35	1.87	1.90	3.44	-2.10	-0.30	0.90	-0.10	2.55
3.50	0.0000575	0.600	0.977	1.045	2.49	1.25	1.54	1.50	-0.90	-0.40	0.60	-0.10	0.96
3.50	0.0000842	0.410	0.975	0.999	1.86	0.79	1.40	0.94	-0.90	-0.20	0.10	-0.10	0.13
3.50	0.0001501	0.230	0.860	0.866	2.02	1.02	1.45	0.95	-0.90	0.30	0.00	-0.10	0.02
3.50	0.0002656	0.130	0.775	0.776	3.00	1.32	1.56	2.20	-2.00	0.90	0.00	-0.20	0.00
3.50	0.0004932	0.070	0.714	0.715	3.67	1.33	1.57	3.04	-1.90	0.80	-2.20	0.40	0.01
3.50	0.0008852	0.039	0.625	0.625	3.68	1.60	1.69	2.85	-2.30	0.90	-1.30	0.60	0.00
3.50	0.0015692	0.022	0.561	0.561	3.55	1.74	1.75	2.56	-2.20	1.10	-0.70	-0.10	0.00
3.50	0.0031384	0.011	0.485	0.485	3.19	1.61	1.68	2.18	-1.50	1.10	-0.80	-0.80	0.00
3.50	0.0080284	0.004	0.405	0.405	4.09	1.98	1.82	3.08	-2.40	1.30	-1.10	0.90	0.00
3.50	0.0203072	0.002	0.344	0.344	9.96	3.11	2.34	9.17	-2.10	1.10	-2.80	8.40	0.00
5.00	0.0000587	0.840	1.034	1.216	8.70	2.42	2.93	7.83	-0.80	-0.10	3.80	-0.60	6.77
5.00	0.0000676	0.730	1.030	1.156	4.55	2.18	2.00	3.46	-2.10	-0.30	1.00	-0.10	2.54
5.00	0.0000822	0.600	1.084	1.158	2.88	1.35	1.55	2.02	-1.60	-0.50	0.50	-0.20	0.99
5.00	0.0001203	0.410	1.077	1.104	2.09	0.76	1.38	1.37	-1.30	-0.40	0.10	-0.10	0.10
5.00	0.0002144	0.230	0.972	0.978	1.92	0.84	1.40	1.01	-1.00	-0.10	0.00	-0.10	0.01
5.00	0.0003794	0.130	0.860	0.862	2.49	0.95	1.43	1.81	-1.80	0.10	0.00	-0.10	0.00
5.00	0.0007045	0.070	0.755	0.755	2.08	1.01	1.45	1.10	-0.20	0.00	-0.90	-0.60	0.00
5.00	0.0012646	0.039	0.678	0.678	2.11	1.10	1.49	1.01	-0.70	0.20	-0.70	0.00	0.00
5.00	0.0022417	0.022	0.587	0.587	2.18	1.15	1.50	1.09	-0.70	0.20	-0.70	-0.40	0.00
5.00	0.0044834	0.011	0.541	0.541	2.37	1.03	1.47	1.55	-1.00	0.30	-0.70	-0.90	0.00
5.00	0.0114692	0.004	0.437	0.437	2.59	1.24	1.53	1.68	-0.70	0.40	-1.30	0.70	0.00
5.00	0.0290103	0.002	0.369	0.369	10.17	2.06	1.84	9.79	-0.60	0.00	-2.30	9.50	0.00
6.50	0.0000763	0.840	1.125	1.319	9.33	2.66	3.35	8.29	-1.10	-0.10	3.30	-0.50	7.51
6.50	0.0000878	0.730	1.081	1.215	4.66	2.49	2.09	3.33	-1.40	-0.50	1.00	-0.10	2.81
6.50	0.0001069	0.600	1.198	1.277	2.91	1.52	1.61	1.89	-1.60	-0.40	0.40	-0.20	0.82
6.50	0.0001564	0.410	1.118	1.146	1.90	0.83	1.39	1.00	-0.90	-0.40	0.10	-0.10	0.09
6.50	0.0002788	0.230	1.014	1.021	2.03	0.84	1.39	1.21	-1.10	-0.50	0.00	-0.10	0.01
6.50	0.0004932	0.130	0.926	0.928	2.16	0.90	1.42	1.36	-1.30	-0.40	0.00	-0.10	0.01
6.50	0.0009159	0.070	0.793	0.793	1.98	0.95	1.43	0.99	0.20	-0.30	-0.60	-0.70	0.00
6.50	0.0016439	0.039	0.674	0.674	2.11	1.04	1.45	1.12	0.30	-0.40	-0.10	-1.00	0.00
6.50	0.0029142	0.022	0.603	0.603	2.03	1.05	1.46	0.94	-0.10	-0.40	-0.60	-0.60	0.00
6.50	0.0058284	0.011	0.548	0.548	2.42	0.93	1.44	1.71	0.40	-0.40	-0.60	-1.50	0.00
6.50	0.0149099	0.004	0.435	0.435	3.02	1.15	1.49	2.35	0.50	-0.30	-1.40	1.80	0.00
6.50	0.0377133	0.002	0.381	0.381	12.01	1.99	1.80	11.71	1.40	-0.20	-3.10	11.20	0.00
8.50	0.0000998	0.840	1.269	1.474	9.77	3.18	3.59	8.52	0.00	-0.60	4.70	-0.40	7.07
8.50	0.0001148	0.730	1.093	1.235	5.06	2.78	2.43	3.46	-0.60	-0.20	0.70	-0.10	3.33
8.50	0.0001397	0.600	1.174	1.257	2.99	1.81	1.68	1.69	-1.20	-0.30	0.50	-0.20	1.02
8.50	0.0002045	0.410	1.186	1.216	1.89	0.95	1.41	0.82	-0.70	-0.40	0.10	-0.10	0.08
8.50	0.0003645	0.230	1.064	1.071	2.02	0.91	1.41	1.12	-1.00	-0.50	0.00	-0.10	0.00
8.50	0.0006449	0.130	0.964	0.966	2.39	0.95	1.43	1.66	-1.60	-0.40	0.00	-0.20	0.01
8.50	0.0011977	0.070	0.821	0.821	2.36	1.01	1.45	1.57	0.80	-0.60	-0.10	-1.20	0.00
8.50	0.0021497	0.039	0.697	0.697	2.10	1.07	1.46	1.07	0.80	-0.40	-0.30	-0.50	0.00
8.50	0.0038109	0.022	0.635	0.635	2.20	1.07	1.47	1.23	0.60	-0.50	-0.30	-0.90	0.00
8.50	0.0076218	0.011	0.550	0.550	2.37	0.97	1.44	1.60	0.30	-0.40	-0.60	-1.40	0.00
8.50	0.0194976	0.004	0.433	0.433	3.27	1.24	1.52	2.62	0.40	-0.40	-1.60	2.00	0.00
8.50	0.0493174	0.002	0.368	0.368	14.74	2.31	1.93	14.43	0.70	-0.50	-3.40	14.00	0.00
12.00	0.0001621	0.730	1.254	1.403	5.19	3.23	2.36	3.31	-0.80	-0.30	0.80	-0.20	3.09
12.00	0.0001973	0.600	1.212	1.300	3.22	2.10	1.77	1.69	-1.10	-0.30	0.40	-0.20	1.16
12.00	0.0002887	0.410	1.280	1.312	2.14	1.09	1.46	1.13	-1.00	-0.50	0.10	-0.10	0.09
12.00	0.0005146	0.230	1.131	1.138	1.97	1.06	1.45	0.81	-0.70	-0.40	0.00	-0.10	0.01
12.00	0.0009105	0.130	1.014	1.016	2.48	1.09	1.47	1.68	-1.60	-0.50	0.00	-0.10	0.00
12.00	0.0016909	0.070	0.821	0.821	2.52	1.19	1.50	1.64	1.20	-0.50	0.00	-1.00	0.00
12.00	0.0030349	0.039	0.689	0.689	2.36	1.25	1.52	1.30	0.90	-0.60	-0.20	-0.70	0.00
12.00	0.0053801	0.022	0.643	0.643	2.45	1.24	1.53	1.46	0.80	-0.50	-0.20	-1.10	0.00
12.00	0.0107602	0.011	0.547	0.547	2.84	1.13	1.49	2.13	1.20	-0.60	-0.70	-1.50	0.00
12.00	0.0275260	0.004	0.435	0.435	4.56	1.46	1.60	4.02	1.00	-0.80	-1.90	3.30	0.00
12.00	0.0696246	0.002	0.383	0.383	16.09	2.86	2.23	15.67	1.10	-0.60	-3.60	15.20	0.00

Table C.1: Table of the H1 results of the DIS cross section measurement and determination of the structure function F_2 based on the mb99 data set.

Q^2 /GeV^2	x	y	σ_r	F_2	δ_{tot}	δ_{sta}	δ_{unc}	δ_{corr}	δE_e	$\delta\theta_e$	δE_{had}	$\delta noise$	$\delta_{\gamma p}$
0.35	0.0000047	0.730	0.356	0.384	27.06	14.59	16.17	0.00	0.30	0.30	1.30	-4.20	2.16
0.35	0.0000999	0.090	0.313	0.314	14.17	6.64	6.25	10.85	-6.30	0.80	-8.60	-0.10	1.85
0.35	0.0006474	0.015	0.198	0.198	11.63	7.69	6.26	6.07	0.50	1.40	-5.30	2.40	0.87
0.35	0.0047626	0.002	0.250	0.250	12.32	8.54	8.46	2.67	-1.80	1.70	-0.80	-0.40	0.42
0.50	0.0000068	0.730	0.403	0.443	9.63	5.53	6.19	4.88	-3.80	2.00	0.00	0.00	2.31
0.50	0.0000082	0.600	0.440	0.464	15.73	4.76	5.81	13.82	-4.40	0.00	0.20	1.60	3.92
0.50	0.0001256	0.090	0.323	0.323	13.10	6.02	5.65	10.18	-4.40	1.50	-8.30	1.40	3.33
0.50	0.0008023	0.015	0.255	0.255	9.55	6.38	5.65	4.31	-3.10	0.10	2.00	-2.20	0.33
0.50	0.0058910	0.002	0.257	0.257	12.23	8.54	8.07	3.39	-0.70	-1.20	-0.70	-3.00	0.22
0.65	0.0000088	0.730	0.474	0.523	6.35	3.58	4.50	2.68	-1.20	0.10	0.00	0.00	2.39
0.65	0.0000107	0.600	0.519	0.549	9.38	3.15	4.26	7.74	-3.10	0.40	-6.60	0.50	2.51
0.65	0.0001401	0.090	0.438	0.438	14.13	5.11	5.28	12.07	-6.40	1.50	-9.90	1.70	1.28
0.65	0.0008860	0.015	0.261	0.261	8.60	6.05	5.34	2.98	-1.30	0.20	-2.10	-1.60	0.41
0.65	0.0065784	0.002	0.274	0.274	10.56	7.50	7.02	2.46	0.20	1.40	-1.30	-1.50	0.37
0.85	0.0000115	0.730	0.587	0.647	5.97	2.86	3.94	3.46	-2.50	-0.30	0.00	0.00	2.37
0.85	0.0000140	0.600	0.600	0.637	4.71	2.42	3.67	1.70	-1.40	-0.60	0.00	0.00	0.75
0.85	0.0000204	0.410	0.590	0.604	10.11	2.17	3.54	9.22	-4.60	0.30	-7.80	1.00	1.37
0.85	0.0001402	0.090	0.427	0.427	10.65	4.08	4.48	8.76	-4.30	0.40	-7.50	1.00	0.95
0.85	0.0009677	0.015	0.298	0.298	9.76	5.05	4.84	6.80	-4.50	1.40	-4.50	1.90	0.44
0.85	0.0075003	0.002	0.290	0.290	9.60	6.82	6.32	2.38	0.70	-0.90	-2.00	0.60	0.00
1.20	0.0000162	0.730	0.658	0.733	5.14	3.00	3.35	2.49	-0.40	-0.60	0.00	0.00	2.38
1.20	0.0000197	0.600	0.677	0.723	4.28	2.04	2.78	2.54	-2.40	0.00	0.00	0.00	0.84
1.20	0.0000289	0.410	0.645	0.662	3.48	1.68	2.57	1.63	-1.60	-0.10	0.00	0.00	0.27
1.20	0.0000515	0.230	0.626	0.631	4.94	2.67	3.28	2.56	-2.20	1.30	0.00	-0.10	0.07
1.20	0.0001050	0.130	0.546	0.546	7.77	2.90	3.33	6.39	-4.60	1.90	-3.90	0.90	0.24
1.20	0.0002330	0.060	0.497	0.497	7.57	3.19	3.57	5.85	-4.00	1.30	-3.60	1.90	0.12
1.20	0.0006028	0.024	0.459	0.459	6.35	4.01	4.39	2.25	-1.70	0.70	-1.20	0.50	0.00
1.20	0.0014707	0.010	0.374	0.374	8.26	4.62	4.75	4.93	-3.30	1.80	-1.10	-3.00	0.00
1.20	0.0072481	0.002	0.265	0.265	8.47	4.88	4.78	5.00	-3.70	0.20	-1.50	3.00	0.00
1.50	0.0000203	0.730	0.706	0.791	5.56	3.41	3.47	2.67	-1.00	-0.50	0.00	0.00	2.43
1.50	0.0000247	0.600	0.726	0.778	3.94	2.09	2.70	1.96	-1.50	-0.90	0.00	0.00	0.89
1.50	0.0000361	0.410	0.743	0.763	3.02	1.28	2.38	1.35	-1.30	-0.30	0.00	0.00	0.20
1.50	0.0000643	0.230	0.684	0.688	3.19	1.67	2.57	0.91	-0.90	0.10	0.00	0.00	0.02
1.50	0.0001234	0.130	0.594	0.595	4.33	1.90	2.66	2.83	-2.00	0.10	-2.00	0.00	0.05
1.50	0.0002625	0.060	0.489	0.489	4.28	1.88	2.62	2.82	-1.90	0.50	-2.00	-0.30	0.01
1.50	0.0006530	0.024	0.433	0.433	4.20	2.21	2.80	2.22	-1.60	1.00	-1.10	-0.40	0.03
1.50	0.0015566	0.010	0.358	0.358	4.92	2.47	2.93	3.08	-2.40	1.00	-0.70	-1.50	0.00
1.50	0.0077752	0.002	0.291	0.291	4.94	2.28	2.84	3.34	-1.80	1.50	-1.30	2.00	0.00
2.00	0.0000270	0.730	0.805	0.904	7.00	4.47	4.05	3.55	-1.50	-2.00	0.00	0.00	2.52
2.00	0.0000329	0.600	0.798	0.857	4.05	2.35	2.76	1.80	-1.30	-0.70	0.00	0.00	1.03
2.00	0.0000481	0.410	0.812	0.834	2.89	1.23	2.33	1.18	-1.00	-0.60	0.00	0.00	0.18
2.00	0.0000858	0.230	0.754	0.760	2.82	1.31	2.36	0.81	-0.80	-0.10	0.00	-0.10	0.02
2.00	0.0001601	0.130	0.666	0.667	3.21	1.51	2.44	1.45	0.00	-0.10	-1.20	-0.80	0.03
2.00	0.0003423	0.060	0.584	0.585	3.15	1.39	2.39	1.51	-0.40	-0.40	-1.40	0.00	0.00
2.00	0.0008460	0.024	0.503	0.503	3.16	1.53	2.46	1.27	-0.60	-0.10	-0.50	-1.00	0.00
2.00	0.0020228	0.010	0.437	0.437	3.85	1.66	2.51	2.39	-0.80	-0.40	-0.30	-2.20	0.00
2.00	0.0100639	0.002	0.321	0.321	4.77	1.66	2.49	3.72	-0.60	-0.60	-1.70	3.20	0.00
2.50	0.0000338	0.730	0.776	0.884	12.19	8.84	6.80	4.93	-3.60	-2.50	0.00	0.00	2.26
2.50	0.0000411	0.600	0.871	0.937	4.80	3.04	3.12	2.02	-0.80	-1.60	0.00	0.00	0.94
2.50	0.0000601	0.410	0.863	0.888	3.10	1.34	2.36	1.50	-1.40	-0.50	0.00	0.00	0.16
2.50	0.0001072	0.230	0.781	0.787	2.94	1.32	2.36	1.17	-1.00	-0.60	0.00	0.00	0.03
2.50	0.0001977	0.130	0.698	0.700	3.36	1.46	2.41	1.83	0.30	-0.60	0.00	-1.70	0.01
2.50	0.0004224	0.060	0.581	0.581	2.89	1.29	2.34	1.10	0.40	-0.40	-0.50	-0.80	0.01
2.50	0.0010458	0.024	0.516	0.516	2.99	1.33	2.36	1.26	-0.20	-0.10	-0.30	-1.20	0.00
2.50	0.0024980	0.010	0.456	0.456	3.54	1.40	2.39	2.20	-0.40	0.00	-0.50	-2.10	0.00
2.50	0.0124678	0.002	0.333	0.333	4.97	1.44	2.39	4.12	0.10	-0.60	-1.70	3.70	0.00
3.50	0.0000575	0.600	0.914	0.988	7.86	5.55	4.62	3.11	-1.80	-2.40	0.00	0.00	0.81
3.50	0.0000842	0.410	0.935	0.963	3.26	1.64	2.46	1.37	-0.40	-1.30	0.00	0.00	0.14
3.50	0.0001501	0.230	0.899	0.905	3.29	1.44	2.42	1.71	-1.60	-0.60	0.00	0.00	0.02
3.50	0.0002656	0.130	0.800	0.802	3.41	1.59	2.47	1.72	1.20	-0.70	-0.20	-1.00	0.00
3.50	0.0005754	0.060	0.691	0.691	3.11	1.34	2.37	1.50	0.80	-0.60	-0.20	-1.10	0.00
3.50	0.0014384	0.024	0.601	0.601	3.62	1.35	2.38	2.36	0.60	-1.10	-0.10	-2.00	0.00
3.50	0.0034522	0.010	0.521	0.521	3.76	1.40	2.40	2.52	0.60	-0.90	-0.60	-2.20	0.00
3.50	0.0172611	0.002	0.353	0.353	5.73	1.53	2.42	4.96	0.70	-0.80	-1.80	4.50	0.00

Table C.2: Table of the H1 results of the DIS cross section measurement and determination of the structure function F_2 based on the svtx00 data set.

Q^2/GeV^2	λ	δ_{sta}	δ_{sys}	c	δ_{sta}	δ_{sys}
0.750	0.126	0.018	0.025	0.130	0.017	0.024
1.350	0.172	0.005	0.008	0.118	0.004	0.008
2.250	0.175	0.004	0.008	0.148	0.005	0.009
2.250	0.189	0.020	0.030	0.137	0.028	0.040
4.250	0.195	0.002	0.004	0.173	0.003	0.005
7.500	0.224	0.003	0.004	0.172	0.003	0.006

Table C.3: Table of the measurement of $\lambda(Q^2)$ and $c(Q^2)$ from fits of the form $\sigma_r = c \cdot x^{-\lambda}$ to the presented low Q^2 data on F_2.

Q^2/GeV^2	x	F_L	δ_{sta}	δ_{sys}
0.750	0.0000098	0.165	0.036	0.138
1.350	0.0000204	0.161	0.028	0.052
2.250	0.0000392	0.172	0.041	0.074
2.250	0.0000329	0.188	0.063	0.090
4.250	0.0000683	0.285	0.025	0.064
7.500	0.0001278	0.418	0.033	0.080

Table C.4: Table of the H1 results of the longitudinal proton structure function $F_L(x, Q^2)$ determination at low Q^2.

Bibliography

[1] R.E. Taylor, Rev. Mod. Phys. **63**, (1991) 573.
H.W. Kendall, Rev. Mod. Phys. **63**, (1991) 597.
J.I. Friedman, Rev. Mod. Phys. **63**, (1991) 615.

[2] S. Glashow, Nucl. Phys. B **8**, (1961) 579.
S. Weinberg, Phys. Rev. Lett. **19**, (1967) 1264.

[3] T. Laštovička, Eur. Phys. J. C **24**, (2002) 529-533.

[4] V. Gribov et al., Sov. J. Nucl. Phys. **15**, (1972) 438.

[5] G. Altarelli, G. Parisi, Nucl. Phys. B **126**, (1977) 298.

[6] E. Kuraev, L. Lipatov, V. Fadin, Sov. Phys. JETP. **44**, (1976) 443.
Y. Balitsky, L. Lipatov, Sov. J. Nucl. Phys. **28** (1978) 822.

[7] M. Ciafaloni, Nucl. Phys. B **296**, (1998) 49.
S. Catani, F. Fiorani, G. Marchesini, Phys. Lett. B **234**, (1990) 339.
S. Catani, F. Fiorani, G. Marchesini, Nucl. Phys. B **336**, (1990) 18.

[8] L. Gribov, E. Levin, M. Ryskin Phys. Rep. **100**, (1983) 1.

[9] V. Fadin. L. Lipatov, Phys. Lett. B **249**, (1998) 127.
G. Camici. M. Ciafaloni, Phys. Lett. B **430**, (1998) 349.
S. Brodsky. G. Lepage, P. Mackenzie, Phys. Rev. D **28**, (1983) 228.

[10] H1: C. Adloff *et al.*, Phys. Lett. B **520**, (2001) 183.

[11] E. Iancu, A. Leonidov and L. McLerran, *The colour glass condensate: An introduction*, hep-ph/0202270.

[12] H1: C. Adloff *et al.*, Eur. Phys. J. C **21**, (2001) 33-61.

[13] A. Donnachie and P. V. Landshoff, Phys. Lett. B **518**, (2001) 63.;
A. Capella, E. G. Ferreiro, A. B. Kaidalov and C. A. Salgado, hep-ph/0106118;
A. Capella, A. Kaidalov, C. Merino and J. Tran Thanh Van, In Meribel les Allues 1994, QCD and high energy hadronic interactions 271-282.

[14] K. Golec-Biernat, M. Wüsthoff, Phys. Rev. D **60**, (1999) 114023.

[15] K. Golec-Biernat and M. Wüsthoff, Phys. Rev. D **59**, (1999) 014017.

[16] J. Bartels, K. Golec-Biernat and H. Kowalski, Acta Phys. Polon. B **33**, (2002) 2853-2858.

[17] A.D. Martin, R.G. Roberts, W.J. Stirling and R.S. Thorne, Eur. Phys. J. C **23**, (2002) 73.

[18] K. Golec-Biernat, private communication.

[19] B.B. Mandelbrot, *The Fractal Geometry of Nature.*, W.H. Freeman, New York 1977.

[20] B.B. Mandelbrot, *How Long is the Coast of Great Britain, Statistical Self Similarity and Fractional Dimension*, Science **155**, (1967) 636-638.

[21] R.P. Feynman and A.R. Hibbs, *Quantum mechanics and path integrals*, McGraw-Hill, New York 1965.

[22] H. Kröger, Phys. Reports **323**, (2000) 81-181.

[23] C. Itzykson, J.M. Drouffe, *Statistical Field Theory*, Cambridge University Press, Cambridge 1989.

[24] G. Roepstorff, *Path Integral Approach to Quantum Physics*, Springer, Berlin 1994.

[25] E. Nelson, Phys. Rev. **150**, (1966) 1079.

[26] H. Kröger, S. Lantagne, K.J.M. Moriarty and B. Plache, Phys. Lett. A **199**, (1995) 299.

[27] H.A. Gersch, Int. J. Theor. Phys. **20**, (1981) 491.

[28] M. Kac, Rocky Mountain, J. Math. **4**, (1974) 497.

[29] G.N. Ord, Int. J. Theor. Phys. **31**, (1992) 1177.
D.G.C. McKeon, G.N. Ord, Phys. Rev. Lett. **69**, (1992) 3.
G.N. Ord, Phys. Lett. A **173**, (1993) 343.

[30] H. Kröger, Phys. Lett. A **213**, (1996) 211.

[31] M.I. Polikarpov, *Fractals in Lattice Gauge Theories*, Moscow ITEP 71-90.

[32] H. Kröger, Phys. Lett. B **284**, (1992) 357.
H. Kröger, S. Lantagne and K.J.M. Moriarty, Mod. Phys. Lett. A **8**, (1993) 445.

[33] T.L. Ivanenko, A.V. Pochinsky, M.I. Polikarpov, Phys. Lett. B **252**, (1990) 631.
M.I. Polikarpov and U.J. Wiese, Moscow ITEP 30-90, Pis'ma Zh. Eksp. Teor. Fiz. **51**, (1990) 296.

[34] L.F. Abbot, M.B. Wise, Am. J. Phys. **49**, (1981) 37.

[35] H. Kröger, Phys. Rev. A **55**, (1997) 951.
H. Kröger, Phys. Lett. A **226**, (1997) 127.

[36] T. Laštovička, in "DIS 2002 - 10th Int. Workshop on Deep Inelastic Scattering", Acta Phys. Polon. B **33**, (2002) 2867-2871.

[37] PDFLIB: The Parton Density Functions Library, Version 8.04, GRV sets 4 and 14(98), CERN.

[38] ZEUS: J. Breitweg et al., Phys. Lett. B **487**, (2000) 53.

[39] ZEUS: S. Chekanov et al., Nucl. Phys. B **637**, (2002) 3.

[40] Nakano et al., Phys. Rev. Lett. **91**, (2003) 012002.

[41] H1: I. Abt *et al.*, Nucl. Instr. and Meth. A **386**, (1997) 310 and 348.

[42] H1: L. Goerlich, et al., *Strategy Studies for the H1 Topological L2 Trigger*, H1 Internal Note H1-09/97-508.

[43] H1: A. Grueber, et al., *A Neural Network Architecture for the Second Level Trigger in H1 Experiment at HERA*, Proceedings of the IEEE Conference TAI94, New Orleans, 1994.

[44] H. Bethe, W. Heitler, Proc. Roy. Soc. A **146**, (1934) 83.

[45] H1: *Technical Proposal to upgrade the Backward Scattering Region of the H1 Detector*, DESY PRC 93/02.

[46] R. Appuhn *et al.*, Nucl. Instr. and Meth. A **386**, (1996) 397.

[47] H1: *Series of Tests of Fine Mesh Photomultiplier Tubes in Magnetic Fields of up to 1.2 Tesla*, DESY-97-070 (1997).

[48] H1: *The LED based Calibration System of the H1 Lead/Scintillating-Fiber Calorimeter*, Nucl. Instr. Meth.

[49] V.V. Arkadov, PhD Thesis, Berlin, Humboldt-University, 2000, DESY-Thesis-2000-046.

[50] H1: C. Adloff *et al.*, Nucl. Phys. B **497**, (1997) 3.

[51] Ed. U. Amaldi, *Proc. of the study of an ep facility for Europe*, DESY 79/48, (1979) 391-394.

[52] U. Bassler, Habilitation thesis, Université Pierre et Marie Curie, Paris, 2003.

[53] A.A. Glazov, PhD Thesis, Berlin, Humboldt-University, 1998.

[54] J. Riedlberger, *The H1 Trigger with Emphasis on Tracking Triggers*, H1 Internal Note H1-01/95-419.

[55] V. Lenderman, PhD Thesis, Dortmund, University of Dortmund, 2002, DESY-Thesis-2002-004.

[56] V. Blobel, Universität Hamburg, *Millepede: Linear Least Squares Fits with a Large Number of Parameters*, unpublished, (2000).

[57] A. Meyer, PhD thesis, Hamburg, 1997.

[58] K.C. Hoeger, Proceedings of the Workshop Physics at HERA, vol.1, DESY, (1992) 43.
S. Bentvelsen, J. Engelen, P. Kooijman, Proceedings of the Workshop Physics at HERA, vol.1, DESY, (1992) 23.

[59] R. Wallny, PhD thesis, Zurich, 2001.

[60] A. Yuille et al., Harvard Robotics Laboratory Technical Report no. 90-7 (1990).

[61] D. Eckstein, PhD Thesis, Berlin, Humboldt-University, 2002, DESY-Thesis-2002-008.

[62] S. Glazov, private communication.

[63] T. Laštovička, in “HEP 2003”, Aachen, to appear in Eur. Phys. J. C.

[64] E. Lobodzinska, in “DIS 2003 - 11th Int. Workshop on Deep Inelastic Scattering”, St.Petersburg, to appear.

[65] H1: C. Adloff *et al.*, Eur. Phys. J. C **30**, (2003) 1-32.

[66] NMC: M. Arneodo *et al.*, Nucl. Phys. **B483** (1997) 3.

[67] H. Abramowicz and A. Levy, The ALLM parameterization of sigma(tot)(gamma* p): An update, DESY-97-251, [hep-ph/9712415] (1997).

Acknowledgements

I would like to address special thanks to Max Klein, supervisor of this thesis, for his support and high level requirements during my PhD study. Fruitful discussions with him gave me a feeling that physics is meaningful and it can be even fun.

I would like to thank to all people i had pleasure to meet during my stay at DESY Zeuthen, DESY Hamburg and Charles University Prague. You made my life more rich and interesting. I decided not to list all the names in this acknowledgements since someone could be accidentally forgotten. If you are reading this and you know that you are one of those people: thank you again!

Special gratitude i would like to express to my closest colleagues with whom i was sharing all difficulties and success during the data analyzes, to Doris Eckstein and Alexey Petrukhin in particular. I would also like to thank to other colleagues perhaps not so directly involved in analyzes but being a part of my life in Germany: Ilja Tsurine, ewelinA Lobodzinska, Jan Kretzschmar, Vova Arkadov, Sasha Glazov, Peter Kostka, Thomas Naumann, Serguey Gorbounov, Wolfgang Lange, Hans Henschel, Katja Lipka and many others.

Separately I would like to thank to my friend Mirek Nožička for: making jokes, caring about H1 silicon trackers, making some more jokes, bringing home-made wine, complaining, preparing strange teas and destroying my Bohemian accent by his Moravian accent.

I am indebted to my brother Radek, my mother and to my father, whom i will always keep in my thoughts, for their support and for the freedom they gave me to decide what i want to do with my life.

Last but not the least i would like to thank to my wife Gordana and daughter Michaela for their patience, especially during the last hectic weeks of this thesis preparation.